Temporal quantum correlations and their applications in quantum metrology

Kawthar Mohamed Al Rasbi

University of Leeds

School of Physics and Astronomy

Submitted in accordance with the requirements for the degree of

Doctor of Philosophy

November, 2023

I dedicate this thesis to my husband, Haitham. Your support and encouragement have been invaluable. I would not have been able to go on this journey without you.

To my children, Malik, Mariah and Ahmed, who fill my heart with joy each and every day, you are the light of my life.

To my parents, Mohamed and Maryam, your love, prayers, and encouragement have been a source of strength and inspiration.

To my brothers, Hassan and Omar, thank you for your constant encouragement, your words of wisdom are greatly appreciated.

To my one and only sister, Huda, thank you for your everlasting love and emotional support throughout my studies.

Last but not least, I dedicate this thesis to the memory of my beloved brother Khalid.

Intellectual Property Statement

The candidate confirms that the work submitted is her own and that appropriate credit has been given where reference has been made to the work of others. This copy has been supplied on the understanding that it is copyright material and that no quotation from the thesis may be published without proper acknowledgement.

The right of Kawthar Mohamed Al Rasbi to be identified as Author of this work has been asserted by her in accordance with the Copyright, Designs and Patents Act 1988.

Some of the content of Chapter 2 and 5 in the thesis has been published in

- K. Al Rasbi, A. Beige and L. A. Clark, " Quantum jump metrology in a two-cavity network ," *Physical Review A* 106, 062619 (2022).

I was the primary investigator of the research and the results were discussed with the other authors.

Chapter 6 of the thesis is in preparation for publication

- K. Al Rasbi, L. A. Clark and A. Beige." Quantum physics cannot be captured by classical linear hidden variable theories even in the absence of entanglement." (in preparation) (2023).

I was the primary investigator of the research and the results were discussed with the other authors.

Acknowledgements

I would like to express my gratitude and appreciation to my supervisor, Dr.Almut Beige, for her guidance and patience throughout my academic pursuit. Her compassion and willingness to help are purely outstanding. I greatly appreciate her generosity and kindness.

I would like to extend my gratitude towards Prof.Jiannis Pachos and Dr.David Jennings for their insightful feedback in reviewing my progress during my PhD journey.

I would like to express my sincere appreciation to Dr.Lewis Clark for providing his guidance and invaluable feedback. The discussions that we had have served as a source of inspiration for me to engage in critical thinking from many different perspectives.

Abstract

The quest to develop and implement techniques that enable the achievement of highly accurate measurements in the estimation of parameters constitutes a crucial component of the field of quantum metrology. Using quantum properties to enhance parameter estimation, the interferometry process requires the development of entangled quantum states and single-shot measurements to extract information about an unknown parameter. Despite its perceived effectiveness, implementing this scheme in a larger number of states is quite challenging. According to recent research, quantum jump metrology offers an alternative method for acquiring information. Using quantum feedback and continuous observation of an open quantum system, this method generates phase-dependent temporal correlations without the need for entanglement as a resource. This study investigates relative phase measurements in an optical network with two cavities and laser-pulse quantum feedback. The methodology proposed in the study is capable of surpassing the standard quantum limit without requiring complex quantum states. Furthermore, the discovery that quantum systems can generate not only local but also temporal non-classical correlations has been the subject of extensive research, along with the search for the most effective quantum devices that exploit these correlations. By analysing the parametrization of the two-cavity metrology scheme, it is possible to observe the analogy between the quantum jump metrology scheme and the formalism of the hidden quantum Markov models. As first steps towards investigating the quantum jump metrology scheme in the hidden quantum Markov formalism, we begin by characterising the main properties of a one-qubit hidden quantum Markov model. Comparing this machine to its classical counterpart with a single bit, a so-called hidden Markov model, we find that hidden quantum Markov model is capable of generating complex stochastic sequences and time correlations more than a single bit hidden Markov model.

Publications

1. K. Al Rasbi, A. Beige and L. A. Clark, " Quantum jump metrology in a two-cavity network ," *Physical Review A* 106, 062619 (2022).

2. Rasbi, Kawthar Al, Photon 2022 IOP conference. *Quantum Jump Metrology with Quantum Feedback in Cavity Networks.*.

3. K. Al Rasbi, L. A. Clark and A. Beige." Quantum physics cannot be captured by classical linear hidden variable theories even in the absence of entanglement." (in preparation) (2023).

Contents

List of Figures

Abbreviations

SQL	Standard Quantum Limit
HL	Heisenberg Limit
MM	Markov Model
HMM	Hidden Markov Model
HQMM	Hidden Quantum Markov Model
POMV	Positive Operator Value Measures
LOCC	Local Operation and Classical Communication

Chapter 1

Introduction

The hypothesis of light quantization as a consequence of the photoelectric effect in accordance with Planck's postulate has revolutionised our understanding of the nature of light, which was previously believed to have only one form, electromagnetic waves. Although, the realisation of the concept of light quantization was postulated a long time before the establishment of quantum theory by Schrödinger and Heisenberg, the experimental verification of controversial quantum theories, such as entanglement, has remained purely theoretical and has been the subject of debate only through 'thought experiments' for a long time. As a result of the difficulty of experimentally validating quantum hypotheses, there has been a great interest in thought experiments. Thought experiments, also known as 'Gedankenexperiment', are hypothetical experiments designed to think deeply about a fundamental phenomenon in physics in order to investigate the properties of the phenomenon and the consequences of the thought experiment. The significance of thought experiments lies in their potential to establish numerous theoretical principles and hypotheses, despite the challenges of testing them in laboratories. These difficult-to-perform investigations aid in the comprehension of the most counter-intuitive quantum laws, such as entanglement and non-locality. In particular, they assist in the investigation of the relationship between the macroscopic classical physics world and the microscopic quantum physics world. Understanding the quantum laws and the thin boundary between

the quantum and classical worlds is crucial for the efficient application of these laws in quantum information, computation, and quantum technologies. Nevertheless, the development of laser devices and photon detectors has made it possible to test quantum hypotheses experimentally, thus overcoming the difficulties in validating the outcomes of thought experiments [1, 2]. In parallel to the development of quantum technologies, a new discipline utilising the quantum properties of systems in quantum computation and quantum metrology has emerged. As a result, an extensive amount of research has been conducted to enhance our comprehension of quantum theories and their practical implementations.

1.1 Quantum parameter estimation

Quantum metrology is one of the promising fields that exploits the quantum properties of systems in quantum technology. The objective of quantum metrology is to enhance the accuracy of measurement processes of parameter estimation. The methods of parameter estimation and phase measurement enhancement have been thoroughly studied recently [2]. Quantum estimation theory is necessary for testing physics principles that may be difficult to infer directly through measurements of observables or the practical difficulty of performing the experiment physically. It also looks for optimisation of parameter estimation methods, maximisation of Fisher information, and minimization of uncertainty in parameter estimation [3]. The pursuit of developing and implementing methods that facilitate the achievement of accurate measurements in parameter estimation is an essential aspect of the field of quantum metrology. Furthermore, the improved computational capacity of optical interferometry networks in quantum metrology has been exhibited by researchers using boson sampling, as suggested by Aaronson and Arkhipov [4]. In addition, it is essential to note that precise and reliable measurements are of the utmost significance in a variety of fields and disciplines. These measurements provide a fundamental basis for a wide range of applications, ranging from the comprehensive investigation of biological samples [5, 6] to the identification and examination of gravitational waves [7]. Moreover, in the field

of science, there is a widespread recognition of the established techniques for proficiently carrying out such measurements. This recognition is substantiated by a range of scholarly publications, such as the works of Demokowitcz-Dobrzanski et al [8], Yang and Zhang [9], Loughridge [10], Ataman [11], and Blanco [12], among others, that have aided in the evolution and enhancement of these methodologies throughout the years. The utilisation of high-intensity sources is commonly considered the most convenient method for improving measurement accuracy. The main resource employed in quantum metrology experiments is usually the number of photons transmitted through the experimental apparatus or the number of detected time measurement outcomes. The standard quantum limit (SQL) represents the highest level of accuracy that can be attained with conventional metrology methods. Any attempt to exceed this boundary using conventional metrology is considered unachievable. Nevertheless, although it was widely believed that quantum enhancement can be only achieved though utilising entangled photons, recent research suggest that breaking the SQL is achievable by following quantum jump approach in quantum metrolgoy [13, 14].

1.2 Open quantum system

In quantum parameter estimation, the use of open quantum systems instead of closed systems has been shown to be a promising approach for measurement enhancement [13, 15–17]. In a closed quantum system that is isolated from its surroundings, the system's energy is always conserved. The wavefunction formalism is frequently utilised in characterising the dynamics of a closed quantum system, while the density matrix formalism is often applicable to mixed states. For a closed quantum system, the system's description and evolution are achieved through unitary evolution. The wavefunction formalism has been developed in a manner that ensures the preservation of the norm of the wavefunction. The Schrödinger equation predicts that [18]

$$\frac{d}{dt}\left|\psi(t)\right\rangle = -\frac{i}{\hbar}H(t)\left|\psi(t)\right\rangle , \tag{1.1}$$

where $H(t)$ is the time-dependent Hamiltonian. The solution of the Schrödinger equation in the case of a closed quantum system where the Hamiltonian is time independent reads

$$|\psi(t + \Delta t)\rangle = U(t + \Delta t, t) |\psi(t)\rangle , \tag{1.2}$$

where $U(t + \Delta t, t) = \exp[-iH(\Delta t)]$ is a unitary time evolution operator. For a time dependent Hamiltonian $H(t)$ such that $[H(t), H(t')] = 0$, the unitary operator is the integration of the Hamiltonian as a function of time; thus, the unitary operator $U(t + \Delta t, t)$ reads as

$$U(t + \Delta t, t) = \exp \int_{t}^{t+\Delta t} (-iH(n)) \, dn . \tag{1.3}$$

As mentioned earlier, the closed quantum system does not have to be in a pure state. For a mixed state quantum system, we resort to the density matrix formalism, that is given by

$$\rho(t + \Delta t) = \sum_{k} w_k U(t + \Delta t, t) |\psi_k(t)\rangle \langle \psi_k(t)| U^{\dagger}(t + \Delta t, t) , \tag{1.4}$$

where w_k is the probability of being in state $|\psi_k(t)\rangle$. Thus, the density matrix is also defined as $\rho(t + \Delta t) = U(t + \Delta t, t)\rho(t)U^{\dagger}(t + \Delta t, t)$. If the quantum system is evolved in small time steps Δt, the unitary operator can be approximated to the first order as

$$U(t + \Delta t, t) \approx 1 - \frac{i}{\hbar} H(t)\Delta t . \tag{1.5}$$

Utilising the approximate definition of the unitary operator, the time evolution of the density matrix reads

$$\rho(t + \Delta t) = \rho(t) - \frac{i}{\hbar}[H(t), \rho(t)]\Delta t . \tag{1.6}$$

Rearranging Eq. (1.6) gives the differential equation

$$\frac{d}{dt}\rho(t) = -\frac{i}{\hbar}[H(t), \rho(t)] . \tag{1.7}$$

The differential equation in terms of the density matrix is known as the Von Neumann equation. Using the notion of statistical mechanics, the differential equation of the density matrix in Eq. (1.7), the Liouville equation, is given by

$$\frac{d}{dt}\rho(t) = \mathcal{L}\rho(t). \tag{1.8}$$

where $\mathcal{L}$ is the Liouville superoperator. The action of the Liouville operator on the density matrix is defined as $\mathcal{L}\rho = -\frac{i}{\hbar}[H(t), \rho]$. If the Hamiltonian H is time independent, then the density matrix using the Liouville equation is $\rho(t + \Delta t) = \exp(-i\mathcal{L}(\Delta t))\rho(t)$.

The closed quantum system approach is not applicable in cases where the quantum system is affected by the surrounding environment. The exchange of energy between the system and the environment is inevitable. In this case, an open quantum system formalism is necessary to establish a mathematical model that includes the dynamics of the quantum system and the surrounding environment, which can have infinite degrees of freedom. The open quantum system can be analysed as a system that interacts with its environment and in which energy is dissipated from the system to the environment. System-environment coupling generates correlations between the system and the environment. In addition, this analysis incorporates noise and corresponds to a more realistic physical system. Thus, the total density matrix of the quantum system S in a Hilbert space $\mathcal{H}_S$ and the environment E in a Hilbert space $\mathcal{H}_E$ can be defined as ρ_{SE} [18].

If we are interested in the evolution of the principal system ρ_S, then it can be defined by evaluating the reduced density matrix of the total system as

$$\rho_S = \text{Tr}_E(\rho_{SE}). \tag{1.9}$$

If $\hat{O}$ is an operator acting on the Hilbert space of the quantum system $\mathcal{H}_S$, then the expectation value of any observable $\hat{O}$ acting on the Hilbert space $\mathcal{H}_S$ where the density matrix of the quantum system ρ_S is only known,

$$\left\langle \hat{O} \right\rangle = \text{Tr}_S[\hat{O}\,\text{Tr}_E(\rho_{SE})] = \text{Tr}_S(\hat{O}\rho_S). \tag{1.10}$$

The evolution of the density matrix of the Schrödinger equation is defined in a similar way as in the case of a closed quantum system, with some differences

in the definition of the Liouville superoperator defined in Eq. (1.6) and it reads

$$\frac{d}{dt}\rho_S(t) = \mathcal{L}\rho_S(t).$$ (1.11)

The Liouville superoperator is defined in terms of a set of operators known as the Lindblad operators L_k. The action of the Liouville superoperator on the reduced density matrix ρ_S

$$\mathcal{L}\rho_S = -\frac{i}{\hbar}[H(t), \rho_S(t)] + \sum_k \Gamma_k(L_k\rho_s L_k^\dagger - \frac{1}{2}[L_k^\dagger L_k, \rho_S]_+).$$ (1.12)

where Γ_k represents the correlation function between the system and the environment, $\frac{1}{2}[L_k^\dagger L_k, \rho_S]_+$ is the anti-commutator of the two terms $L_k^\dagger L_k$ and ρ_S. It is readily apparent that the key difference between a closed system and an open quantum system lies in the addition of the Lindblad operators. In the context of open quantum systems, the additional terms are incorporated to account for the energy dissipation that occurs between the quantum system and its surrounding environment.

1.3 Open quantum system as hidden quantum Markov model

Modelling stochastic processes has recently seen the development of a number of quantum algorithms that demonstrate the potential advantages of quantum-based measurements over classical measurements. The standard approach for modelling stochastic processes with hidden states, in which an observable variable depends on the state of the system, is commonly referred to as hidden Markov models (HMM). In such a model, the future state of the system depends solely on its current state; consequently, information regarding the system's prior states is lost. On the other hand, the quantum version of the hidden Markov model, also known as hidden quantum Markov model (HQMM), that was first introduced by Monras et al.[19] represents a more general quantum counterpart to a previous proposal of evolosing qunatum systems using Von Nuemann projective

measurement [20]. The advantage of the quantum based Markov models was further demonstrated by research publications such as those authored by Cholewa et al. [21], Srinivasan et al.[22] and Markov et al.[23]. The utilisation of HQMM requires a reduced number of states for the purpose of modelling a stochastic process, in contrast to classical models for the same stochastic process. The HQMM has been utilised to model the open quantum system, as demonstrated by the findings presented in recent research Ref. [13, 24]. The operators that trigger transitions in HQMMs are formulated based on trace preserving Kraus operators. Consequently, an open quantum system that is subjected to quantum feedback will undergo an evolution through Kraus operators that follow parametrisation conditions of HQMMs. As a result, the suggested open quantum system model might find use in quantum stochastic process simulations or quantum computations.

1.4 Motivation and aim

An alternative method to classical parameter estimation method, quantum jump metrology approach, has been proposed for parameter estimation enhancement. Research has demonstrated that the utilisation of quantum feedback has the capability to measure phase shifts between two light pathways with a level of precision that surpasses the SQL. Unlike other quantum metrology approaches, quantum jump metrology does not require the use of entanglement as a resource. Rather than relying on entanglement, this approach employs non-classical temporal correlations, which are frequently more readily accessible. In this context the quantum jump metrology approach refers to the utilisation of quantum feedback loops in quantum metrology. This involves the continuous monitoring of an open quantum system over a duration of time, while conducting a sequence of consecutive measurements on the system. The previously mentioned methodology exhibits the potential for achieving an accuracy level that surpasses the standard quantum limit (SQL). By employing this methodology, it is feasible to achieve an enhancement in accuracy for phase shift measurements between

light pathways that surpass the SQL, without necessitating entanglement [13, 14]. The employed optical network comprises of an optical cavity situated within a quantum feedback loop. This network is used to perform measurements on the phase differences between the two light pathways. The measurements are based on the non-linear dynamics of the individual quantum trajectories of the cavity's state. The primary resource utilised in quantum jump metrology is time, which is comparatively more accessible than entanglement. The utilisation of quantum jump metrology is, therefore, well suited for expanding to complex networks, in comparison to alternative quantum metrology approaches. Furthermore, the implementation of quantum jump metrology schemes solely requires linear optics, which are easily accessible and can be expanded to more complex networks.

In this thesis, we lay the foundation for enhancing a previous single-parameter quantum jump metrology scheme and generalising it to the simultaneous measurement of phase shift difference between light pathways with a precision exceeding the SQL [13]. The proposed network is more complex as it comprises of two optical cavities within an instantaneous feedback loop. A sequential measurement approach is employed on the system using generalised measurement operators. This introduces complex non-linear dynamics in the system, as previously explored in studies by Monras et al.[19] and Clark et al. [24] on hidden variables. Upon closer examination of the open quantum system formalism of optical networks from a stochastic processes modelling perspective, it becomes evident that the open quantum system model, which undergoes a time evolution governed by Kraus operators, can be classified as a HQMM, as previously discussed in the literature[19, 24]. The investigation of formalism for open quantum systems as HQMM is conducted in light of the temporal correlations present in the quantum jump metrology approach for phase shift measurements. Furthermore, we conduct a comparative analysis of the performance of a basic HQMM in demonstrating correlations among measurements to the performance of the classical counterparts, specifically, the Markov model (MM) and the HMM.

1.5 Outline

This thesis consists of seven chapters. In Chapter 2 we review the methods of parameter estimation using optical experimental setups. We focus on the measurement of phase shift difference between two light pathways in a classical Mach–Zehnder interferometer. We present a comprehensive discussion of classical parameter estimation methods, with a specific emphasis on the Mach–Zehnder interferometer as an example of a tool that is capable of attaining the utmost scaling accuracy achievable within classical frameworks that is known to operate at the SQL. Subsequently, we examine the utilisation of quantum properties of systems to achieve an improvement in parameter estimation beyond the SQL. We present a comprehensive analysis of quantum-based methodologies that have the potential to exceed the SQL. Our focus is on the practical implementation of these techniques. More concretely, we present the notion of a quantum metrology approach that employs the quantum jump method within an open quantum system to produce temporal correlations among successive measurements on an optical network. In addition, we discuss the evaluation of the maximum accuracy attainable in parameter estimation methodologies through the estimation of the Cramér-Rao bound. We conclude this chapter by discussing the temporal correlations that exist in quantum and classical systems.

In Chapter 3 we shall introduce the modelling of open quantum systems consisting of a principal quantum system and the environment. We study the quantum mapping in open quantum systems using density matrix representation and the generalised measurements for retrieving information from the evolving open quantum system. We focus on the operator-sum representation and quantum mapping using Kraus operators. Then we study the dynamical evolution of an open quantum system using master equations of Lindbladian form. The master equation formalism established earlier can be challenging to solve analytically, therefore we resort to the numerical analysis using a quantum trajectory theory. The primary benefit of using this approach lies in its ability to model the dynamics of individual trajectories of the quantum systems. As a result, it is possible to investigate both the system's individual trajectory and the ensemble behaviour

of a vast number of trajectories.

In Chapter 4, we present a theoretical framework for studying the dynamics of a single cavity network as an open quantum system inside a feedback loop. Using a coherent state for the state of the cavity, the description of the system's master equation yields extremely non-linear equations that cannot be solved analytically. For an ensemble of individual trajectories, we investigate the dynamical behaviour of the optical cavity and the photon statistics of the system. Consequently, we discuss the parameter estimation accuracy of the single cavity network in phase shift difference measurement.

In Chapter 5, we introduce our proposed optical network which consists of two cavities network inside an instantaneous feedback loop. The optical network here is treated as an open quantum system and we follow the quantum jump approach to analyse the dynamics of the system. By studying a simulation of the evolution of the optical network that results in a large ensemble of individual trajectories of the system we are able to assess the performance of the network in estimating the phase shift difference for sets of different parameters.

In Chapter 6, we introduce the mathematical modelling of stochastic processes in the context of hidden models. We provide an in-depth examination of the Markov model, hidden Markov model, and a quantum version model based on Markov chains known as the hidden quantum Markov model. We assess the models in terms of the existence of correlations between observing successive measurements by revisiting the basic definitions and parametrisation of the three models to evaluate the probability of observing certain sequences. Finally, in Chapter 7, we provide a conclusion to this thesis by examining the outcomes of prior simulations.

Part I

Background

Chapter 2

Parameter Estimation

Classically, there are two primary methods for enhancing parameter estimation: either by increasing the number of probing systems or repeatedly conducting the experiment. This approach fails in many cases in which repeating the experiment for a large number of times is not possible or due limited resources. Moreover, the highest accuracy attainable by classical methods is limited by the SQL. The employment of quantum properties of physical systems revealed that there is an advantage achieved in enhancing parameter estimation beyond the SQL and reaching the Heisenberg limit (HL) using fewer resources and quantum entanglement [16, 25–27]. However, since the implementation of quantum entanglement at a large scale is not experimentally and readily feasible, other methods to surpass the SQL are investigated. In particular, we focus on the quantum jump metrology as an alternative approach in which the temporal correlations formed as a result of sequential measurements on an optical network system using coherent states subjected to instantaneous quantum feedback as an input. Moreover, this scheme exhibits measurement enhancements beyond the SQL with relativity accessible linear optics elements.

In this chapter, we discuss the classical parameter estimation methods with a particular focus on the Mach–Zehnder interferometer as an example of an apparatus capable of achieving the highest scaling accuracy possible within classical frameworks. Then, we introduce the concept of quantum parameter estim-

ation, in which we discuss methods used to achieve measurement enhancement in parameter estimation through utilising the quantum properties of systems. We primarily focus on employing quantum jump metrology approach for parameter enhancement. Furthermore, we discuss the quantification of the accuracy of the parameter estimation scheme utilising the concept of Fisher information and Cramér–Rao bound. Finally we conclude this chapter by introducing the concept of quantum correlation through entanglement and addressing the classical correlations that exist in stochastic processes.

2.1 Classical parameter estimation

The classical approach to estimating an unknown parameter φ can be achieved through the utilisation of N independent probes in a measurement process, as illustrated in Fig. 2.1. In the present case, the scaling of the uncertainty of the estimator, denoted by $\Delta\hat{\varphi}$, with the number of probes, denoted by N, is constrained by the SQL, which tells us that [11, 28]

$$(\Delta\hat{\varphi})^2 \ \propto \ \frac{1}{N} \tag{2.1}$$

where N here is the resource. The development of alternative metrology techniques has been essential to surpassing the SQL. As previously noted, the improvement of measurements can be achieved through two classical methods: increasing the number of resources N employed in the experiment or conducting the experiment multiple times to reduce the measurement's uncertainty. The classical scheme of standard metrology is shown in Fig. 2.1. The accuracy of the measurements can be inferred from the number of systems that have been put into operation. Nonetheless, the feasibility of such an approach may be limited in certain cases, for example when the object under investigation is fragile or exhibits a limited lifespan [5]. In instances such as these, accurate assessments are made only through multiple repartitions of the measurements. This is due to the fact that the measurements rely on optical interferometry and do not employ the properties of quantum physics.
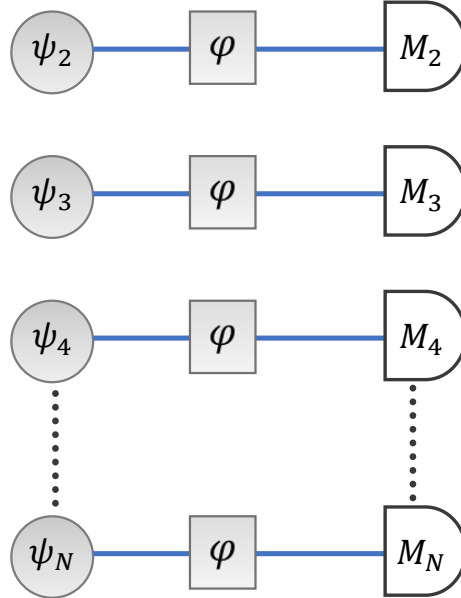
Figure 2.1: Classical/uncorrelated scheme consisting of independent and uncorrelated systems in which each probe is first encoded with the parameter to be determined and then measured. In such a case, the accuracy of measurement is limited by the standard quantum limit.

To investigate the phase estimation performance of a classical interferometer, we conduct a thorough analysis of the classical scheme for parameter estimation enhancement. The ultimate goal of analysing a classical interferometer is to use it as a benchmark for evaluating complex measurement schemes later. The measurement of the phase difference between two light pathways can be approached through a classical method that involves the implementation of an interferometer equipped with two phase shifters one on each arm. This approach is widely used in the field and has proven to be effective in parameter estimation. Here, we examine the Mach–Zehnder interferometer scheme shown in Fig. 2.2. The inputs are carefully arranged such that a coherent state is directed towards only one input, denoted as $|\alpha\rangle$, while the other input is the vacuum state $|0\rangle$. The objective is to examine various components and their functions to gain a better understanding of the experimental procedure and obtain an in-depth examination

of the experimental configuration illustrated in Fig. 2.2. Conducting a thorough examination of the experimental setup, we aim to enhance our understanding of the underlying principles and mechanisms at play in the observed phenomenon.

Employing a quantum mechanical framework to investigate the Mach–Zehnder interferometer, we utilise the creation and annihilation operators to provide a quantum mechanical representation of a lossless beam splitter. It is noteworthy that when a coherent state is present in one input and a vacuum is present in the other, the input port containing the vacuum is characterised by a quantized field in the vacuum mode. Moreover, in case of coherent state, the classical analysis of the scheme would yield identical outcomes as the quantum mechanical treatment.

Using the quantum mechanical framework, the annihilation field operators between the input ports (a_0, a_1) and the output ports (a_2, a_3, a_4, a_5) of the above interferometer are given by [28],

$$a_2 = \frac{1}{\sqrt{2}}(a_0 + ia_1),$$
$$a_3 = \frac{1}{\sqrt{2}}(a_1 + ia_0),$$
$$a_4 = \frac{1}{\sqrt{2}}(e^{i\varphi_1}a_2 + ie^{i\varphi_2}a_3),$$
$$a_5 = \frac{1}{\sqrt{2}}(e^{i\varphi_2}a_3 + ie^{i\varphi_1}a_2). \tag{2.2}$$

Here, for a 50:50 beam splitters, the reflected beam gains a factor of i upon reflection and the mirrors add a factor of $e^{i\pi/2}$ that can be ignored.

Re-writing the output annihilation operators a_4 and a_5 in terms of the input annihilation operators a_0 and a_1 we obtain the following equations,

$$a_4 = ie^{i(\varphi_1+\varphi_2)/2}\left[-\sin\left(\frac{\varphi_2-\varphi_1}{2}\right)a_0 + \cos\left(\frac{\varphi_2-\varphi_1}{2}\right)a_1\right],$$
$$a_5 = ie^{i(\varphi_1+\varphi_2)/2}\left[\cos\left(\frac{\varphi_2-\varphi_1}{2}\right)a_0 + \sin\left(\frac{\varphi_2-\varphi_1}{2}\right)a_1\right]. \tag{2.3}$$

For comparing the Mach–Zehnder interferometer to a more complex model that will be discussed later, we chose a coherent state and the vacuum state as the interferometer's inputs. Assuming a coherent state is incident on one input and vacuum on the other, $|\psi_{\text{in}}\rangle = |\alpha, 0\rangle$ describes the initial quantum state. After

15
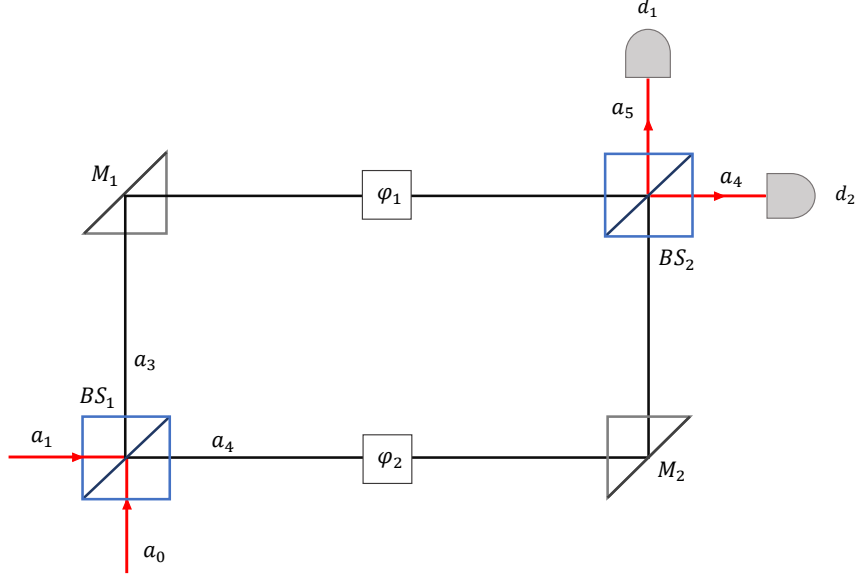
Figure 2.2: Mach–Zehnder interferometer experiment with a coherent state in one input port and a vacuum state in the other input port sent through a 50:50 beam splitter, BS_1, and then passing through phase shifters, φ_1 and φ_1, at each light pathway. The two modes travel through another 50:50 beam splitter, BS_2, before being measured at one of the two detectors, d_1 and d_2.

passing through the beam splitters and phase shifters, the final state at the output port reads

$$|\psi_{\text{out}}\rangle = S\,|\psi_{\text{in}}\rangle \tag{2.4}$$

where $S = S_{\text{BS1}}S_{\text{Phase}}S_{\text{BS2}}$, $S_{\text{BS1}} = S_{\text{BS1}} = \frac{1}{\sqrt{2}}\begin{pmatrix} 1 & i \\ i & 1 \end{pmatrix}$ is the beam splitter transformation matrix and $S_{\text{Phase}} = \begin{pmatrix} e^{i\varphi_1} & 0 \\ 0 & e^{i\varphi_2} \end{pmatrix}$.

In particular, after passing the beam splitter and the phase shifters, the initial state $|\psi_{\text{in}}\rangle$ transforms to a tensor product of coherent states as follows

$$|\psi_{\text{out}}\rangle \rightarrow i e^{i(\varphi_1+\varphi_2)/2}\left|-\alpha\sin\!\left(\frac{\varphi_2-\varphi_1}{2}\right), \alpha\cos\!\left(\frac{\varphi_2-\varphi_1}{2}\right)\right\rangle. \tag{2.5}$$

We present next a thorough analysis of the accuracy of the phase shift measurement of this interferometer scheme. Here, we can easily see that the probability of detecting a photon at the first detector d_1 and second detectors d_2, respectively,

$$P_1 = \mid \alpha \mid^2 \sin^2(\frac{\varphi_2 - \varphi_1}{2}),$$
$$P_2 = \mid \alpha \mid^2 \cos^2(\frac{\varphi_2 - \varphi_1}{2}). \tag{2.6}$$

These probabilities represent the oscillatory nature of photon detection at the detectors, which is dependent on the phase shift difference $\varphi_2 - \varphi_1$. To gain a better understanding of the accuracy of the measurement of the phase difference between the two light paths of this interferometer scheme, we must also estimate the measurement uncertainty. To accomplish this, we can employ the error propagation formula [29]

$$\Delta\hat{\varphi} = \frac{\Delta O}{\mid \frac{\partial \langle O \rangle}{\partial \varphi} \mid}. \tag{2.7}$$

where $\Delta O = \sqrt{\langle O^2 \rangle - \langle O \rangle^2}$. To estimate the uncertainty of the phase measurement in such a scheme, we can consider the number operator N as an observable O. Using the second d_2 output port (i.e. a_4), the number operator in which we are interested here is $N_4 = a_4^\dagger a_4$. Hence the uncertainty in phase measurement, assuming a coherent state input, is given by Eq.(2.1) as,

$$\Delta\hat{\varphi} = \frac{\Delta N_4}{\mid \frac{\partial \langle N_4 \rangle}{\partial \varphi} \mid} \tag{2.8}$$

where, $\Delta N_4 = \sqrt{\langle N_4^2 \rangle - \langle N_4 \rangle^2}$. Refer to the appendix A for detailed derivation of $\langle N_4^2 \rangle$ and $\langle N_4 \rangle$.

Therefore, one can see that the expectation values of $\langle N_4^2 \rangle$ and $\langle N_4 \rangle$ are given by [11],

$$\langle N_4 \rangle = \mid \alpha \mid^2 \cos^2(\frac{\varphi_2 - \varphi_1}{2}). \tag{2.9}$$

$$\langle N_4^2 \rangle = \mid \alpha \mid^4 \cos^4(\frac{\varphi_2 - \varphi_1}{2}) + \mid \alpha \mid^2 \cos^2(\frac{\varphi_2 - \varphi_1}{2}). \tag{2.10}$$
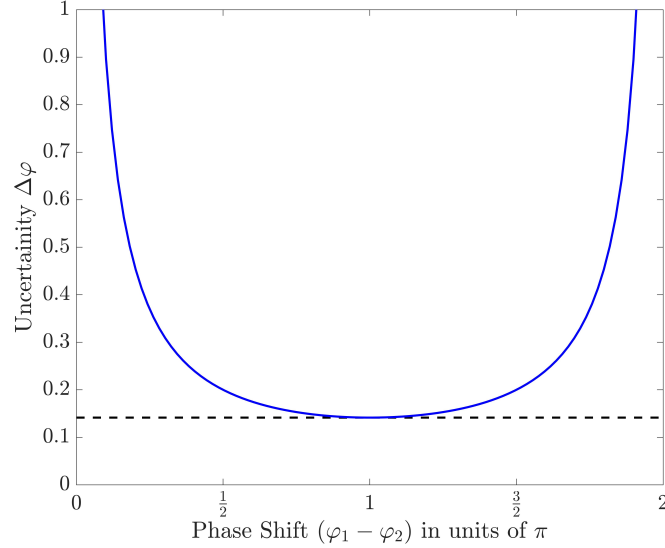
Figure 2.3: Uncertainty in phase measurement $\Delta\hat{\varphi}$ as function of phase difference $(\varphi_2 - \varphi_1)$ for a coherent state input in one port and vacuum in the other port. For a single input coherent state $|\alpha|^2 = 50$, the uncertainty clearly reaches a minimum limit that is proportional to $1/\sqrt{\overline{N}} = 1/\sqrt{50}$.

Using Eq. (2.8) and the expressions of the expectation values shown in Eq. (2.9) and Eq. (2.10), the phase measurement uncertainty $\Delta\varphi$ reads,

$$\Delta\hat{\varphi} = \frac{1}{\mid \alpha \sin\left(\frac{\varphi_2 - \varphi_1}{2}\right) \mid} \, . \tag{2.11}$$

The average number of photons $\overline{N}$ is defined in terms of the input coherent state as $\overline{N} = |\alpha|^2$; therefore, Eq. (2.11) becomes,

$$\Delta\hat{\varphi} = \frac{1}{\sqrt{\overline{N}} \mid \sin\left(\frac{\varphi_2 - \varphi_1}{2}\right) \mid} \, . \tag{2.12}$$

As seen from Eq. (2.12), the accuracy in the measurement scales as $\Delta\hat{\varphi} \sim 1/\sqrt{\overline{N}}$ which is essentially the SQL. A graph of the uncertainty $\Delta\hat{\varphi}$ as a function of the phase shift $(\varphi_2 - \varphi_1)$ is shown in Fig. 2.3. The uncertainty $\Delta\hat{\varphi}$ in the phase measurement diverges rapidly when $(\varphi_2 - \varphi_1) = k2\pi$, where $k \in \mathbb{Z}$, while it reaches a minimum value at $(\varphi_2 - \varphi_1) = \pi$. One can see that the uncertainty in

the phase shift measurement becomes smaller when the number of photons sent through the setup increases. However, as we had predicted, the uncertainty will always be bound to a certain limit that scales as the SQL.

2.2 Quantum parameter estimation

It has recently been recognised that quantum metrology, in particular, can be used to investigate the properties of quantum physics [25, 30, 31]. The utilisation of quantum properties of systems can potentially enhance the precision of measurements without increasing the size of probes [32–34]. Further research has been carried out on the topic of metrology, with a particular emphasis on the quantum behaviour of systems as a method of achieving measurement enhancement. Interferometric devices are frequently employed in the measurement of physical quantities, with light serving as the source of measurement. The current research explores the field of quantum metrology and its potential for surpassing the SQL through the utilisation of entanglement. Through extensive research, it has been discovered that the implementation of entanglement in quantum metrology can lead to enhanced measurements beyond the SQL. The quantum metrology scheme is displayed in Fig. 2.4. In the case of correlated probes, this scaling can be enhanced. In the case of probes exhibiting maximal correlation, it is possible to achieve the HL, which is proportional to the number of probes. The experimental protocol requires the preservation of entanglement among different systems throughout the duration of the experiment. The new limit is known as HL and it scales as [30]

$$(\Delta\hat{\varphi})^2 \quad \propto \quad \frac{1}{N^2} \,. \tag{2.13}$$

This means that for large N, some unknown parameter φ can be estimated with much higher precision. Determining how to obtain and utilise such correlated probes has thus been an active area of research. However, although entanglement is possible to realise experimentally, it is quite challenging to extend entanglement schemes to include a large number of systems [35].
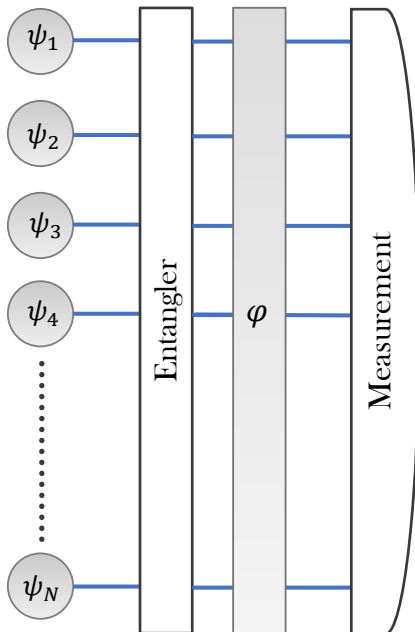
Figure 2.4: A quantum mechanical scheme to achieve an enhancement in estimating an unknown parameter φ utilising entangled states give rise to higher measurement accuracy reaching the Heisenberg limit.

As illustrated in Fig. 2.4, one solution is to evolve entangled quantum states in a φ-dependent fashion followed by a collective measurement of their state [36–44]. However, a typical problem with this approach is that it is difficult to implement. For example, it has been shown that so-called N00N states, which are highly-entangled N-particle states, are optimal for quantum interferometry experiments [39, 43–48]. However, reliably obtaining a reasonably large N in the laboratory to realise the previously-described enhancement remains extremely challenging [49, 50]. Using entanglement is not the only way of enhancing measurement precision [35, 51–55]. For example, in Ref. [35], it has been shown that another way of overcoming the SQL in Eq. (2.1) is by using non-linear or interacting systems. Using this approach, the uncertainty $\Delta\hat{\varphi}$ can scale such that

$$(\Delta\hat{\varphi})^2 \quad \propto \quad \frac{1}{N^k}. \tag{2.14}$$

where k is the order of the non-linearity of the interaction. Once again though,

non-linearities are often hard to implement experimentally, particularly when processing information with light.

At this point, it is useful to note the generality of the form of the N 'probes' in Eqs. (2.1), (2.13) and (2.14). Typically, these can be imagined as individual particles, or some dimensionality of the system. However, the value N can also be interpreted as the query complexity of the system, i.e. the number of incompressible steps [13, 56]. Hence, while in a single-shot setup, the number of particles is clearly the relevant resource N, for a continuously monitored system, N may instead be counted as the number of times the system is 'probed', i.e. it is related to the temporal resolution of detection.

2.3 Quantum jump metrology parameter estimation

In this thesis, we adopt an alternative approach and use *quantum jump metrology* [13, 14] to improve the precision of estimation. Quantum jump metrology does not require the preparation of highly entangled quantum states or the presence of non-linear optical elements; therefore, it is relatively easy to implement. Its basic idea is to deduce information about an unknown parameter φ by monitoring the (quantum jump based) output statistics of an open quantum system. To ensure that the dynamics of the individual quantum trajectories of the system depend on φ, we use quantum feedback [57], that is triggered by certain measurement outcomes, as illustrated in Fig. 2.5. Using the dynamics of open quantum systems, particular in continuously monitored systems, to infer information about an unknown parameter has recently received a lot of attention in the literature [15, 58–60]. The use of quantum feedback has found a variety of applications not only in quantum metrology [13, 14], but also in quantum error correction and noise reduction [61], quantum state stabilisation [62], entanglement control [63] and in implementing the HQMM [24]. Moreover, it has recently been shown that quantum feedback can lead to ergodicity breaking in quantum optical systems [64]. This can again be achieved even when using only coherent states and

Figure 2.5: Quantum jump metrology scheme to achieve an enhancement in estimating an unknown parameter φ, where the quantum system is evolved in time inside an instantaneous feedback loop. Sequential measurements on the system allows for an enhancement of the estimation performance beyond the SQL due to the existence of temporal correlations.

feedback in the form of displacements of the field, thus only requiring relatively simple technology for implementation. The quantum jump metrology approach is considered a quantum approach since it involves the detection of single photons.

Intuitively, we can see how quantum feedback can lead to time correlations in the bath statistics of an open quantum system. Consider a quantum optical system that emits a photon at a time t_1. Then, as the system is perturbed by the feedback, the emission probability for another photon is altered. Thus, the emission at time t_2 is correlated with the emission at t_1. If this feedback depends on an unknown parameter, these correlations can be used to gain information for its estimation. Hence, it is not surprising that quantum feedback is a powerful tool for quantum technology tasks. The quantum jump metrology approach has offered an alternative method to achieve enhancement in phase shift measurements of light pathways to obtain high accuracy beyond the SQL. The

enhancement in the parameter estimation has been demonstrated using an optical cavity inside a quantum feedback loop to perform measurements on the phase difference between two light pathways [13, 14]. The accuracy of the measurements in this model that based on the non-linear dynamics of quantum trajectories was found to beat the SQL. This scheme is thought to have a promising application in quantum metrology since it only requires more accessible linear optics, which are readily available. Moreover, the scheme may be extended to more sophisticated networks. The motivation behind using a quantum jump approach is the fact that both standard metrology and standard quantum metrology have their limitations when implemented experimentally or by extending the schemes to complex networks. On the other hand, the crucial factor that is a key element of quantum jump metrology is that it does not rely on entanglement.

2.4 Parameter estimation and Cramér-Rao bound

The determination of the lower bound of the precision in the estimation of a parameter φ is an essential component of parameter estimation. This lower bound can be evaluated by Cramér-Rao inequality [65, 66]. The Cramér-Rao bound tells us that the minimum uncertainty achievable by an estimator is bounded by the Fisher information as

$$(\Delta\hat{\varphi})^2 \geq \frac{1}{F(\varphi)}. \tag{2.15}$$

Here, $\Delta\hat{\varphi}$ is the uncertainty in estimating the unknown parameter φ and $F(\varphi)$ is the Fisher information.

In the parameter estimation, the amount of information that can be gained from a certain measurement is quantified by the Fisher information. Let $\mathbf{x}$ be a string of data of length N with elements $x_i \in \mathbb{Z}^+$, while $P_\varphi(\mathbf{x})$ is the probability for this string to occur given a certain φ. The Fisher information $F(P_\varphi)$ for such

data is defined as

$$
\begin{aligned}
F(P_\varphi) &\equiv \sum_{\mathbf{x}} P_\varphi(\mathbf{x}) \left[\partial_\varphi \ln \left(P_\varphi(\mathbf{x}) \right) \right]^2 \\
&= \sum_{\mathbf{x}} \frac{\left[\partial_\varphi P_\varphi(\mathbf{x}) \right]^2}{P_\varphi(\mathbf{x})} \, ,
\end{aligned}
\tag{2.16}
$$

where we sum over all possible combinations of output data $\mathbf{x}$. Since φ is the unknown parameter to be probed, the probability distribution $P_\varphi(\mathbf{x})$ must be a function of this variable. If the N data points are uncorrelated, each contributes an independent amount of information such that $(\Delta\hat{\varphi})^2$ scales like Eq. (2.1). However if the data possesses correlations, then the information contribution from each value may be beyond linear with respect to the number of data points. In particular, the correlations that may exist in quantum systems can lead to more precise measurements when compared with a classical system with the same number of particles [30, 31]. This can lead to scaling of the form of the HL in Eq. (2.13).

2.5 Quantum correlations and classical correlations

Quantum entanglement is a property of composite quantum systems that exhibit non-classical/quantum correlations between measurements of entangled systems even when they are spatially distant from each other. These correlations have been proven to be unreproducible classically, as Bell's inequality violation experiment has already demonstrated. Therefore, we can consider the phenomenon of entanglement as a quantum property of entangled systems, which produces non-classical correlations that cannot be described by classical formalism. Entanglement, that is considered the 'essence of quantum physics' as defined by Erwin Schrödinger [67], is currently receiving increasing interest in the field of quantum information. Since the identification of the implications of entanglement in composite quantum systems has been recognised, significant focus has been directed towards exploring the potential implementation of this resource in

quantum technology applications [67]. One of the recent methods to utilise entanglement in technology is through the generation of time-bin entangled photons, which is found to be a promising method in quantum communication applications [68, 69]. In addition, quantum entanglement experiments have been used to emphasise the inadequacy of alternative classical theories as a replacement for quantum theory. For example, theories that became known as hidden variable models would have to be non-local [1, 70–72].

Furthermore, extensive research has been conducted to quantify quantum entanglement, resulting in the proposal of various measures [73, 74]. Although quantifying entanglement is quite challenging, it can be argued that a measure of entanglement should satisfy the following conditions: the entanglement measure must be zero in the case of separable states; in addition, it should result in maximum value in the case of maximally entangled states; and the entanglement measure cannot increase under the local operation and classical communication (LOCC). In general, several approaches, such as the entanglement witnesses, the relative entropy, and the entanglement discord [75], can be used to measure the degree of entanglement. Entanglement is known to produce quantum correlations between measurements that do not generally exist in classical formalism. In general, unlike entangled systems, classically correlated systems are locally accessible, and the action of performing measurement on one part of the system does not affect the total state of the system. One of the methods to identify the distinction between classical and quantum correlations can be identified by determining the quantum discord of the system since the discord vanishes to zero in the case of classical systems [76].

Nevertheless, the presence of correlations between measurements may be utilised for quantum measurement enhancement. Quantum entanglement is one of the methods to introduce enhancement in measurement; however, other methods exist that exhibit correlations between measurements without entanglement, leading to measurement enhancement in parameter estimation [77–79]. As mentioned earlier, the open quantum systems can be regarded as an example of HQMMs. This kind of stochastic models has been known to show correlations between meas-

urements [19, 24]. Classically, the correlations between measurements represent an important aspect in the study of stochastic processes modelling. Stochastic process have well been understood as mathematical tools that employ probabilistic modelling in order to analyse random processes. Despite the extensive research on stochastic processes, the modelling of these processes remains a challenging task due to the complex nature of the system's evolution. One of the most well-known stochastic process modelling techniques is MMs. The MM is a stochastic model used for modelling random processes. It is widely recognised as an essential stochastic process modelling tool [80]. Due to the widespread use of stochastic processes, MMs play a crucial role in numerous fields, including machine learning, distribution sampling, and modelling DNA sequencing [81–83].

A more sophisticated model used to resemble more realistic stochastic processes is the HMMs. In this model, the system's state is not directly observed; however, it is rather deduced from a series of outcomes that arise from successive measurements performed on the system [84–87]. The HMM is recognised for its ability to solve three main problems in machine learning. The first is the maximum likelihood problem, which is modelled using the forward algorithm [85, 88]; the second is the decoding problem, which is addressed by the backward algorithm formulated by Vitberi [85, 89]; and lastly, the learning problem, which is modelled using the forward–backward algorithm developed by Baum and Welch [85, 90]. HMMs are utilised in numerous fields, including speech recognition [86, 91], finance [92] and genetics [93]. In the field of classical physics, HMMs have been employed in a variety of areas, including simulating stochastic thermodynamics [94] and tracking gravitational waves [95]. Moreover, the implementation of HMMs in quantum physics has been extensively investigated for the purpose of simulating stochastic processes. One such application involves the simulation of electron tunnelling in quantum dots through the use of HMMs [96]. Furthermore, these models can be implemented to study the quantum jumps in optical cavities [97]. However, as the complexity of the system increases, the HMMs encounter challenges in simulating stochastic processes. In addition, the presence of temporal correlations in consecutive measurements of the system cannot be sustained

for a longer period of time in most cases as the information about the previous state of the system is lost.

2.6 Summary

This chapter provided a comprehensive analysis of techniques for parameter estimation and phase measurement enhancement. As previously discussed, the standard approach for improving parameter estimation involves two primary methods: increasing the number of probing systems or conducting multiple repetitions of the experiment. This approach fails in many cases in which it is not feasible to conduct the experiment repeatedly on a large scale or due to resource constraints. Furthermore, classical methods are limited by the SQL, which imposes an upper limit on the maximum achievable accuracy. The utilisation of quantum properties of physical systems has demonstrated a notable benefit in enhancing parameter estimation beyond the SQL, ultimately attaining the HL while employing fewer resources through the application of quantum entanglement. Nevertheless, due to the complexity of implementing quantum entanglement on a large scale experimentally, alternative approaches are being explored to overcome the SQL.

Our study centered on quantum jump metrology approach that serves as a feasible alternative method that does not require entanglement. We focused on the quantum jump metrology with quantum feedback in which the temporal correlations formed as a result of sequential measurements on an optical network system using coherent states as an input that are subjected to instantaneous quantum feedback. We noted that such a scheme would exhibit measurement enhancements beyond the SQL with relativity accessible linear optics elements. Furthermore, the evaluation of the Cramér-Rao bound of the scheme is found to be a suitable measure of the maximum accuracy achievable by the proposed optical network. We concluded this chapter by discussing the correlations that exist between measurement in entangled systems. In addition, we focus on the correlations that exist in systems that do not relay on entanglement, i.e. quantum

jump metrology approach, which may be more accessible scheme than entangled system.

Chapter 3

Open quantum systems

The classical approach of viewing physical systems as isolated from their surroundings is inadequate for describing the irreversible evolution of quantum systems in the real world. In reality, any quantum system cannot be truly isolated from the environment. The leakage of information from quantum systems to the environment is unavoidable, and as a result, correlations eventually form between the system and the environment. Therefore, it is essential to employ a specialised approach that considers the influence of the surrounding environment on quantum systems and the dissipation of information into the environment. Since the wavefunction formalism is used to describe only pure states, we transition to the density matrix formalism, which is able to describe both pure and mixed states.

In this chapter, we will look at quantum mapping in open quantum systems in Section 3.1, in which we will start by reviewing the density matrix formalism for describing an open quantum system consisting of a principal quantum system and the environment. In addition, we thoroughly discuss the analysis of quantum mapping in terms of operator-sum representation, also known as Kraus representation. We introduce the master equation for evolving open quantum systems in Section 3.2, which incorporates all necessary approximations such as the Markov approximation and the coarse-grained time evolution needed to account for the environment's effect on the principal quantum system. Then, using

the Kraus operator representation, we arrive at the master equation form of an open quantum system. Finally, in Section 3.3, we discuss the concept of quantum trajectory theory and introduce a numerical tool for solving the master equation of an open quantum systems.

3.1 Quantum mapping in open quantum systesm

The quantum mapping of open quantum systems involves evolving the density matrix of the composite principal system and environment over time. As mentioned earlier, for closed quantum systems, the dynamics of the system are often described by a unitary time-evolution operator that can be written in terms of either wavefunctions or density matrices. However, once we move from closed quantum systems to open quantum systems, the dynamics formalism must be adjusted to comply with the properties of open quantum systems and the non-unitary evolution. In that sense, open quantum systems are often described by a density matrix to allow for monitoring the principal system part of the composite principal system and environment over time. In the case of open quantum systems, three equivalent approaches to quantum operations exist for quantum mapping: the physically motivated axioms approach, the system coupled to the environment approach, and the operator-sum representation [98]. In this section, we focus on the quantum mapping of quantum systems by operator- sum representation.

3.1.1 Density matrix

The formalism of the density matrix for mixed states is characterised by the summation of the projectors into the pure state $|\psi_i\rangle$ of the system, weighted by their respective probabilities p_i as [99]

$$\rho = \sum p_i |\psi_i\rangle \langle \psi_i|. \tag{3.1}$$

Here, the density matrix ρ must be a positive Hermitian matrix with positive eigenvalues where $\sum_i p_i = 1$.
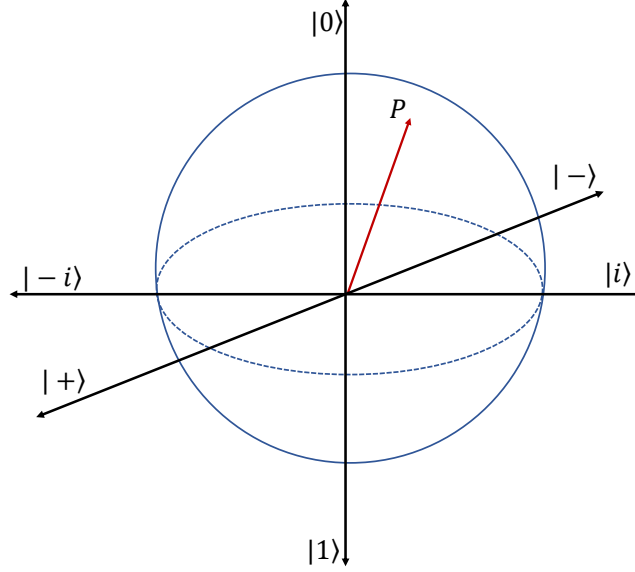
Figure 3.1: A Bloch sphere representation of a mixed state density matrix in which any vector is represented in the Bloch sphere using the density matrix elements. The z axis is the axis with states $|0\rangle$ and $|1\rangle$, the y axis is the axis with states $|-i\rangle$ and $|i\rangle$ and the x axis is the axis with states $|-\rangle$ and $|+\rangle$. Here, P represent a mixed state vector that lies inside the Bloch sphere.

Considering a two-level system such as a qubit with states $|0\rangle$ and $|1\rangle$, the density matrix of this system is given by [99],

$$\rho = \begin{pmatrix} \rho_{00} & \rho_{01} \\ \rho_{10} & \rho_{11} \end{pmatrix}. \tag{3.2}$$

The diagonal elements ρ_{00} and ρ_{11} of the matrix are the probability of the qubit to exist in states $|0\rangle$ and $|1\rangle$, respectively. Moreover, the off diagonal elements ρ_{01} and ρ_{10} represent superposition of states $|0\rangle$ and $|1\rangle$. The superposition terms are known as coherence. The mixed state density matrix can be identified by evaluating a trace of the square of the density matrix. In the case of a mixed state density matrix, $\text{Tr}(\rho^2) \neq \text{Tr}(\rho)$.

To conserve the normalization of the density matrix, the probabilities of finding the qubit in ground and excited states satisfy the following condition: $\rho_{00} + \rho_{11} = 1$. The density matrix ρ can be defined in Bloch representation, as

shown in Fig. 3.1, as

$$\rho = \frac{1}{2}(\mathbb{1} + \mathbf{P}.\sigma) \tag{3.3}$$

where σ is a vector defined in terms of the three Pauli matrices σ_x, σ_y and σ_z. The vector $P(u, v, w)$ is the qubit's polarisation that is a three-dimensional vector defined in terms of the density matrix elements as

$$
\begin{aligned}
u &= \rho_{01} + \rho_{10}\,, \\
v &= i(\rho_{01} - \rho_{10})\,, \\
w &= (\rho_{00} - \rho_{11})\,.
\end{aligned} \tag{3.4}
$$

As indicated previously, the density matrix is essential for describing open quantum system evolution. If we consider a principal quantum system S interacting with the environment E, the total density matrix of the open quantum system of composite $S + E$ is ρ_{SE}. If we are concerned only with monitoring the evolution density matrix of the principal system S, it can be obtained by performing a partial trace over the environment.

$$\rho_S = \text{Tr}_E(\rho_{SE})\,. \tag{3.5}$$

In an open quantum system, for a system consisting of a principal system and the environment ρ_{SE}, the expectation value of a certain observable $\hat{O}_S$ of the principal system S is given by

$$\langle \hat{O}_S \rangle = \text{Tr}_S(\hat{O}_S \rho_S)\,. \tag{3.6}$$

Here, the relation $\text{Tr}(\rho_S) = \text{Tr}(\rho_S^2)$ does not generally hold since the density matrix represents a mixed state. On this basis, the state of the principal system density matrix reads

$$\rho_S = \sum_i p_i^S \left| \psi_i^S \right\rangle \left\langle \psi_i^S \right|\,, \tag{3.7}$$

where the non-negative p_i^S must sum to 1, $\sum_i p_i^S = 1$.

In the field of quantum operations, the process of retrieving information from a quantum system requires an understanding of two key factors: first, the probability of observing a specific outcome, and second, the state of the system subsequent to the measurement of the observed outcome. These considerations are crucially significant in the context of quantum measurement. Since the open quantum systems employed involve monitoring the evolution of a subsystem (i.e. the principal system) of the total system consisting of the principal system and the environment, it is necessary to introduce the generalized measurements known as non-projective positive operator value measures (POVMs) to monitor the evolution of the principal system after performing measurement on the total composite system. The POVMs fulfil the following criteria: the operators are Hermitian, positive, and form a complete set that sums up to identity [98].

If the composite system of the principal system S and the environment E is too large to evaluate or the information about the surrounding environment is not fully known. Then we may use the description of an ancillary system to simulate the evolution of the composite system of the principal system and the environment using unitary operators. As an example, for a short time scale Δt, assuming that the correlations between the environment the and the system are eliminated initially, at $t = 0$, the density matrix of the environment can be assumed to be $\rho_E = |0\rangle \langle 0|$. Again, to determine the evolution of the density matrix of the system, we perform a partial trace over the environment. By imposing the above conditions, the evolution of the density matrix in which the outcomes of the measurements are unknown is given by [98]

$$\mathcal{E}(\rho_S) = \sum_k \langle k | U_{SE}(\rho_S \otimes |0\rangle \langle 0|)U_{SE}^\dagger |k\rangle \ . \tag{3.8}$$

The term $\langle k | U_{SE} |0\rangle$ forms a positive operators set $\{K_k\}$, where $K_k = \langle k | U_{SE} |0\rangle$. Therefore, the evolution in Eq.(3.8) can be written in terms of the operators $\{K_k\}$ as

$$\mathcal{E}(\rho_S) = \sum_k K_k(\rho_S)K_k^\dagger. \tag{3.9}$$

Here, the operators K_k satisfies the completeness relation $\sum_k K_k K_k^\dagger = I$.

3.1.2 Operator-sum representation/ Kraus representation

As mentioned in the previous section, the quantum mapping of a composite system of the principal system S and environment E can be quite cumbersome. Instead of looking at the total degrees of freedom of the environment, we can instead use an ancillary system that is allowed to interact with the principal system. In other words, the ancillary system can be used to describe the effect of the environment on the system. The introduction of the ancillary system simplifies the quantum mapping of the total system [99].

Theorem 1 *Kraus representation theorem: Any operator $\rho \rightarrow S(\rho)$ of dimension d_S^2 that is Linear, completely positive, Hermitian and trace preserving can be written in term of finite set of Kraus operators as* [100]

$$S(\rho) = \sum_{i=1}^{d_s^2} K_i \rho K_i^{\dagger}, \qquad \sum_{i=1}^{d_s^2} K_i K_i^{\dagger} = I \,. \tag{3.10}$$

The advantage of using operator-sum representation (in the form of Kraus operators) is that it allows one to monitor the evolution of the basic system without continuously monitoring the dynamical evolution of the surroundings. This formalism serves to simplify the analysis of an open quantum system, while retaining relevant information regarding the principal system.

The physical interpretation of operator-sum measurements can be deduced by taking a closer look at Eq. (3.8). As indicated previously, for a principal system ρ_S interacting with an environment represented by pure basis states $|k\rangle$ and assuming the density matrix of the environment initially is given by $\rho_E = |0\rangle \langle 0|$, the normalised density matrix of the system after measurement of outcome i is [98]

$$\rho_{S_i} = \frac{\sum_i K_i \rho_S K_i^{\dagger}}{\text{Tr}(\sum_i K_i \rho_S K_i^{\dagger})} \,. \tag{3.11}$$

where $K_i = \langle i| U_{SE} |0\rangle$. Here, the term in the denominator can be thought to be the probability of getting outcome i after evolving the system with the corresponding Kraus operator K_i. In other words, the quantum operator K_i evolves the

density matrix of the principal system ρ_S as in Eq. (3.11), where the probability that this evolution occurs is $\text{Tr}(\sum_i K_i \rho_S K_i^\dagger)$.

While it is true that the Kraus operator is not a unique expression for a given quantum system, it offers a significant advantage in quantum mapping using a finite set of operators scales as the square of the system dimension, regardless of the dimension of the environment. This can be achieved by recognising that the Hilbert space required to represent the system–environment is d_S^2, where d_S denotes the Hilbert space of the system. Furthermore, this approach guarantees that the mapping is completely positive.

3.1.3 Quantum mapping using Kraus representation

The quantum mapping of open quantum systems, as discussed earlier, can be performed by Kraus operators. The use of unitary operators is not restrictive, thus, in addition to that, one can also perform projective measurements P_n after evolving the system using the unitary operator U. If the total system $\rho = \rho_S \otimes \rho_E$ undergoing a unitary evolution given by

$$\rho' = P_n U_{SE}(\rho_S \otimes \rho_E) U_{SE}^\dagger P_n \,. \tag{3.12}$$

where U is the unitary transformation describing the system–environment interaction, while P_n are the projectors on the total density matrix ρ. The state of the total system after measurements is [98]

$$\rho' = \frac{P_n U_{SE}(\rho_S \otimes \rho_E) U_{SE}^\dagger P_n}{\text{Tr}(P_n U_{SE}(\rho_S \otimes \rho_E) U_{SE}^\dagger P_n)} \,. \tag{3.13}$$

Here, the denominator is the probability of getting outcome n.

The evolution of the principal system only is defined as a partial trace over the environment, thus, the state of the principal system reads [98]

$$\rho'_S = \frac{\text{Tr}_\text{E}(P_n U_{SE}(\rho_S \otimes \rho_E) U_{SE}^\dagger P_n)}{\text{Tr}(P_n U_{SE}(\rho_S \otimes \rho_E) U_{SE}^\dagger P_n)} \,. \tag{3.14}$$

If the state of the environment is given by $\rho_E = \sum_j b_j \, |j\rangle \langle j|$, and taking the orthonormal basis of the environment to be $|k\rangle$, then the mapping of the principal

system density matrix $\mathcal{E}(\rho_S)$ reads [98]

$$\mathcal{E}_n(\rho_S) = \sum_{jk} \langle k| \, P_n U_{SE}(\rho_S \otimes b_j \, |j\rangle \, \langle j|) U_{SE}^\dagger P_n \, |k\rangle) \, . \tag{3.15}$$

Looking at the equation closely, we can see that $K_{jk} = \sqrt{b_i} \, \langle k| \, P_n U_{SE} \, |j\rangle$. Hence $\mathcal{E}_n(\rho_S)$ can be equivalently expressed as

$$\mathcal{E}_n(\rho_S) = \sum_{jk} K_{jk} \rho_S K_{jk}^\dagger \, . \tag{3.16}$$

By employing this particular treatment, it becomes possible to establish a Kraus operator for a given open quantum system that undergoes a system–environment unitary interaction as well as performing a generalised measurement on the composite system-environment after the unitary interaction .

3.2 Master equation for open quantum systems

When addressing the dynamical evolution of an open quantum system, the most effective method is to use the Hamiltonian to describe the system's evolution over time. The process of evolution is subsequently described by the Schrödinger differential equation. For a quantum system with specific modes coupled to the environment, the equation governing the time-dependent evolution of the density operator is commonly referred to as the master equation. This section will outline the derivation of the master equation for an open quantum system. We will begin by establishing the necessary conditions that must be satisfied for the derivation of the master equation in Lindblad form, and then proceed to derive the master equation using the Kraus operator representation. The presented derivation of the Lindbald master equation is based on the quantum information approach [99, 100].

3.2.1 Markov approximation and coarse-grained time evolution

The dynamics of a composite quantum system and its surrounding environment can be described by employing first-order differential equations, commonly

referred to as master equations. These equations provide a method for modelling the time evolution of the system, taking into consideration the interactions between the system and its environment. This approach allows for a comprehensive understanding of the system's behaviour over time. If the principal quantum system S and the environment E demonstrate Markovian evolution, it is possible to adequately describe the system using the master equation in differential form. This is because the state of the system at time $t+\Delta t$, denoted as $\rho(t+\Delta t)$, is solely dependent on the state at time t, denoted as $\rho(t)$. Thus, the master equation in the differential form is sufficient to capture the dynamics of the system.

Nevertheless, the evolution of the principal system and its surrounding environment is a highly complex process, primarily due to the vast space of environmental degrees of freedom. As a result, it becomes necessary to adopt an incremental evolution approach, commonly referred to as the coarse-grained time evolution. It is essential to ensure that the incremental time is not only smaller than the characteristic evolution time of the principal system but also significantly greater than the correlation time of the environment [99]. Therefore, fluctuations in the environment can be neglected. Moreover, the Markov approximation holds significant importance as it assumes that the principal system and the environment are not initially entangled during the time interval of the coarse-grained evolution.

Hence by employing the Kraus representation of quantum mapping for a reduced density matrix describing the evolution of the principal system ρ_S only is given by

$$\mathcal{E}(\rho_S) = (\rho_S(t + \Delta t)) = \sum_i K_i(\Delta t)\rho_S(t)K_i(\Delta t)^\dagger \qquad (3.17)$$

where $K_i(\Delta t)$ are the Kraus operators. In the following section, we explicitly derive the master equation in Lindblad form using the Kraus representation of the principal system.

3.2.2 Master equation for open quantum systems in Lindbladian form

The analysis of the evolution of an open quantum system, which comprises a principal system coupled to an environment with infinite degrees of freedom, is a complex task. One possible approach is to compute the reduced trace of the density matrix for the open system consisting of the principal system and its environment. This enables us to effectively disregard the influence of the environment. Such a formalism can be described using the master equation with the super Liouvillian operator $\mathcal{L}$ [18, 101, 102]. This form of the master equation is known as the Lindbladian master equation. The Lindbladian master equation reads [99, 103]

$$\dot{\rho} = \mathcal{L}\rho \,. \tag{3.18}$$

The construction of the Liouvillian operator $\mathcal{L}$ can be achieved by coupling the principal system to the environment, and applying the Born approximation, in which the system is weakly coupled to one degree of freedom of the environment. In other words, the environment's properties can be considered to be time independent. Moreover, the system is hugely affected by environment modes, while the environment is not generally affected by changes introduced by the principal system. In addition, the Markov approximation is employed which states that the environment is able to return to a steady state faster than the principal system. In other words, the environment has no memory of past interactions. Finally, a partial trace over the environment gives the evolution of the principal system only.

Nevertheless, here we follow the derivation of the master equation using the Kraus representation of the density matrix. The operator-sum representation allows for describing the evolution of the principal system ρ_S as function of time in the most general method. This approach is considered to be based on quantum information fundamental concepts. Taking into consideration the Markov approximation and the coarse grained evolution approach, the differential form of

the density matrix of the principal system can be expressed as follows [99]

$$\frac{d\rho_S(t)}{dt} = \frac{\mathcal{E}(\rho_S(t)) - \rho_S(t)}{\Delta t} \tag{3.19}$$

where Δt is the infinitesimal time interval chosen for evolving the system that satisfies the coarse-grained evolution approach. Here we assume that the principal system and the environment are not entangled at $t = 0$. Hence, it is probable that they are not entangled at time Δt. The environment typically has a preferable state, such as the vacuum state of the free radiation field, and returns to it on the coarse-grained time scale given by Δt. Up to the first order in Δt, the action of the quantum map $\mathcal{E}$ on the density matrix of the principal system is expressed as

$$\mathcal{E}(\rho_S(t)) = \rho_S(t + \Delta t) = \rho_S(t) + O(\Delta t). \tag{3.20}$$

Moreover, we can assume that one of the Kraus operators governing the evolution to be near identity and it can be expressed as

$$K_0 = I - iB\Delta t. \tag{3.21}$$

Here, B is the operator that is independent of Δt. This operator B can be used to define two a Hermitian operators as

$$H = \hbar\frac{B + B^\dagger}{2} \quad J = i\frac{B - B^\dagger}{2}, \tag{3.22}$$

where $B = H/\hbar - iJ$. Therefore, using Eq. (3.17) and the definition operators of B in terms of H and J, one can see that by approximating the Kraus operator K_0 to the first order,

$$K_0(\Delta t)\rho_S K_0^\dagger(\Delta t) = \rho_S - \frac{i\Delta t}{\hbar}[H, \rho_S] - \Delta t(J\rho_S + \rho_S J). \tag{3.23}$$

The rest of the Kraus operators K_i are given by

$$K_i = \sqrt{\Delta t}L_i. \tag{3.24}$$

in first order of Δt. Here the L_i operators are independent of Δt. Moreover, following the completeness relation of the Kraus operators given in Eq. (3.10),

we can see that the completeness relation gives

$$\sum_{i=0} K_i(\Delta t)^\dagger K_i(\Delta t) = K_0^\dagger K_0 + \sum_{i>0} K_i^\dagger K_i$$
$$= I - 2J\Delta t + \sum_{i>0} \Delta t L_i^\dagger L_i = I \qquad (3.25)$$

where $J = \frac{1}{2}\sum_{i>0} L_i^\dagger L_i$. Here, the density matrix of the system in Kraus operator representation is given by

$$\rho_S(t + \Delta t) = K_0(\Delta t)\rho_S K_0^\dagger(\Delta t) + \sum_i K_i(\Delta t)\rho_S K_i^\dagger(\Delta t). \qquad (3.26)$$

These approximations lead to the final differential master equation

$$\frac{d\rho_S(t)}{dt} = -\frac{i}{\hbar}[H, \rho_S] + \sum_{i>0}(L_i\rho_S L_i^\dagger - \frac{1}{2}L_i^\dagger L_i\rho_S - \frac{1}{2}\rho_S L_i^\dagger L_i). \qquad (3.27)$$

The term L_i is considered to be a Lindblad operator or quantum jump operator. The first term in Eq. (3.27) represents the unitary evolution while the second term represents the quantum jumps of the system, and the term $\frac{1}{2}L_i^\dagger L_i\rho_S - \frac{1}{2}\rho_S L_i^\dagger L_i$ is needed to keep the normalisation in the event when no jump is observed. After careful examination of the derivation of the master equation in the Lindblad form using the operator-sum representation, the analogy between the evolution of a system using Kraus operators and the master equation of Lindbald form can be identified. In other words , we may consider a principal system coupled to the environment, where the environment is monitored continuously. At each time step, we project onto the basis of the environment; hence, the monitored environment experiences a quantum jump with a probability of order of $O(\Delta t)$ and no jump with a probability of order $1 - O(\Delta t)$, as indicate by Eq. (3.21) and Eq. (3.24) [100].

3.3 Quantum trajectory theory

Analytical solutions are not always possible for the master equation in the Lindblad form, since the master equation involves the exchange of information between the system and the environment. The complex nature of stochastic

processes and the challenges associated with solving the master equation analytically require an alternative approach to study the evolution of the system. One such method involves unravelling the master equation of the Lindbladian form, which refers to modelling the dynamics of individual trajectories over an extended period. Hence, a need exist for the adoption of a numerical approach to solve the master equation [99, 103, 104]. More specifically , quantum jump method, also known as quantum trajectory theory, can be utilised in the unravelling of the master equation [105, 106]. In this approach, the wavefunction of the system is evolved using a non-Hermitian Hamiltonian. The key difference between the utilisation of the master equation with density matrix formalism and the quantum trajectory theory lies in the fact that the latter employs wavefunctions instead of the density matrix to derive the photon statistics of the principal system [106–116]. The main advantage of employing this methodology lies in its ability to simulate the dynamics of individual trajectory of the quantum systems. Therefore, it is possible to examine both the individual trajectory of the system and the ensemble behaviour of a large number of trajectories. Furthermore, this approach allows for simplifying the quantum description of the whole open quantum system. This is achieved by reducing the size of the Hilbert state of the environment from d^2 in the density matrix representation of master equations to d through the use of the wavefunction formalism.

To illustrate the key difference between the individual trajectory and the ensemble average of trajectories of a quantum system, we study the spontaneous emission of a driven atom, that is one of the examples in which quantum trajectory theory can be employed. The atom experiences emission accompanied by a decay to the ground state and re-excitation to the excited level repeatedly. It has been observed experimentally that an atom exhibits these quantum jumps as a form of light and dark patterns [117, 118]. Taking the quantum jump method approach to simulate the dynamics of the atom, Fig. 3.2 shows the difference between a single trajectory of the probability of finding the atom in an excited state as a function of time for an average of 500 trajectories. Although both figures appear to oscillate with time, the behaviour of the single trajectories clearly differs from

the behaviour of the ensemble average of trajectories, as the latter experience a decay in amplitude as time progresses. Moreover, we note that the single trajectory shows instances where the probability decay to zero abruptly. These are the quantum jumps that the atom experiences while emitting a photon that is detected as a click in the photon detector. This figure has been created using a MATLAB code available in Ref. [119] [1].
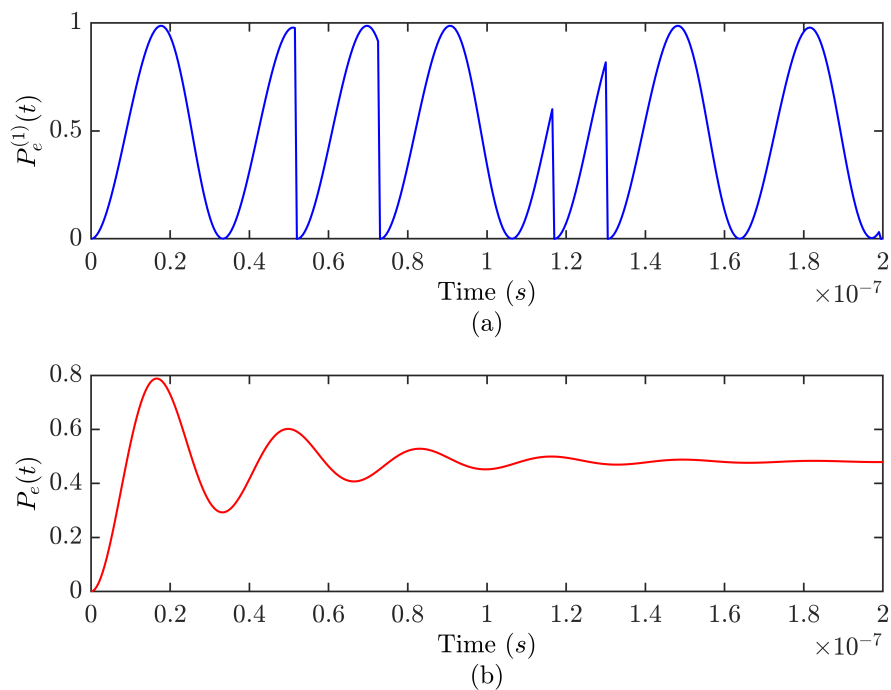
Figure 3.2: Quantum trajectory of a driven two-level atom. (a) A single trajectory of the probability of the atom being in the excited state as a function of time. (b) The average of 500 trajectories of the probability of finding the atom in an excited state as function of time. Here, the decay rate is $\Gamma = 2\pi \times 10^6$, the Rabi frequency is $\Omega = 5\Gamma$, the detuning is $\Delta = 0.5\Gamma$ and the evolution time for simulation is $\delta t = 0.5 \times 10^{-9}$.[1]

To establish the mathematical framework of quantum trajectory theory, we may look at an example of a relaxing two-level atom coupled to a cavity field [103]

---

[1] The Matlab simulation of two-level atom code
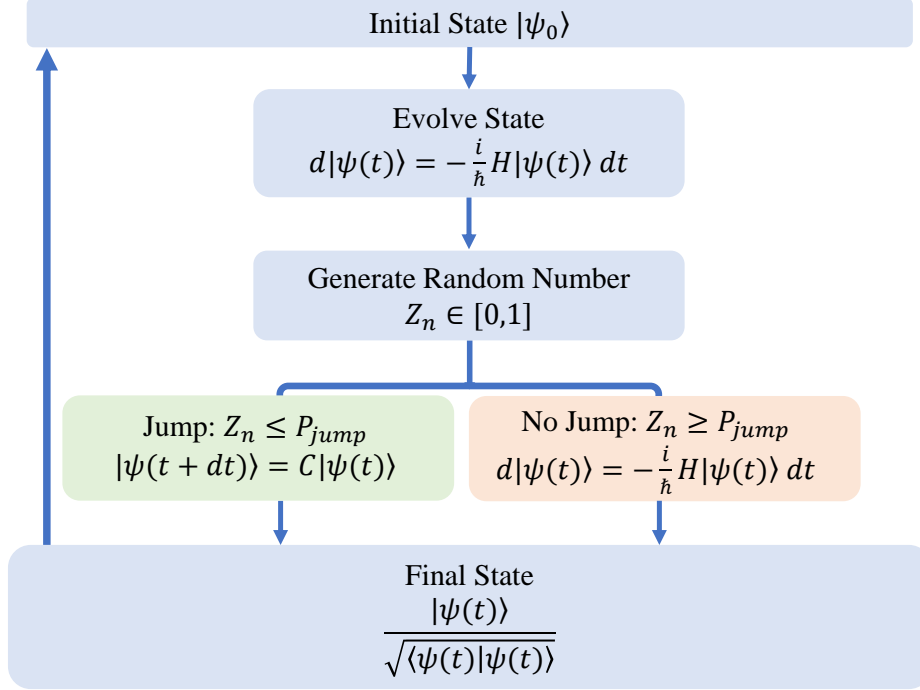
Figure 3.3: A flow chart showing the quantum trajectory theory method approach for evolving the wavefunction as function of time. At each time step, the evolution of state of the system $|\psi(t)\rangle$ is determined by comparing the probability of the system to undergo a jump P_{jump} to randomly generated number Z_n. In case P_{jump} is larger than Z_n, the system experiences a jump by emitting a photon; otherwise, the system decays exponentially with no photon emission. Here C is defined to be an annihilation operator [103].

in which we examine its dynamics. Following the quantum trajectory theory, the evolution of a quantum system is shown in Fig. 3.3. Suppose the system starts at initial state $|\psi(t)\rangle$, then the evolution of the state using the Schrödinger equation is defined as

$$\frac{d}{dt}|\psi(t)\rangle = -\frac{i}{\hbar}H_{eff}|\psi(t)\rangle \ . \tag{3.28}$$

Here, the non-Hermitian Hamiltonian $H_{eff} = H_S - i\hbar\Gamma\sigma_+\sigma_-/2$, where Γ is the

spontaneous decay rate , $H_S = \hbar\omega\sigma_z/2$ and σ_+/σ_- are the atomic raising/lowering operators, respectively.

To simulate the evolution of a relaxing two-level atom, at each time step t_n, the probability that the atom will experience a quantum jump P_{jump}, i.e. emit a photon. Thus, the probability density that the atom will experience a quantum jump is [103]

$$P_{jump}(t_n) = \Gamma \langle\psi(t_n)|\,\sigma_+\sigma_-\,|\psi(t_n)\rangle \ . \tag{3.29}$$

After calculating the probability of photon detection P_{jump}, a random number is generated Z_n, then the random number Z_n is compared to the probability of detecting a photon. If the random number is larger than or equal to $Z_n \geq P_{jump}$, then the atom is thought to experience a spontaneous emission decaying to the ground state. The evolution of the wavefunction in this event reads

$$|\psi(t_{n+1})\rangle = \frac{\sigma_-\,|\psi(t_n)\rangle}{\sqrt{\langle\psi(t_n)|\,\sigma_+\sigma_-\,|\psi(t_n)\rangle}} \ . \tag{3.30}$$

We note here that the non-Hermitian Hamiltonian leads to non-unitary evolution. Hence, re-normalization of the wavefunction is required at each time step. In the case that $Z_n \leq P_{jump}$, the atom experiences a continuous decay with no photon emission, and the evolution of the wavefunction is

$$|\psi(t_{n+1})\rangle = \frac{e^{-\frac{i}{\hbar}H_{eff}dt}\,|\psi(t_n)\rangle}{\langle\psi(t_n)|\,e^{\frac{i}{\hbar}(H_{eff}^\dagger - H_{eff})dt}\,|\psi(t_n)\rangle} \ . \tag{3.31}$$

The quantum jump method is an efficient tool for simulating the behaviour of an open quantum system in the presence of the environment. The system's wavefunction is used instead of the density matrix, and it evolves based on a randomly generated number that determines which event would occur. These events are determined by the calculated probability, that subsequently determines whether a jump has occurred or not. By averaging over multiple trajectories, we can obtain a reasonable approximation of the system's evolution over time.

3.4 Summary

In this chapter, we presented the study of open quantum systems undergoing an evolution in which the system is allowed to interact with the surrounding environment. We started by discussing the density matrix formalism of open quantum systems. Then, we discussed the quantum mapping of open quantum systems, where the state of the system is commonly represented by the density matrix rather than the wavefunction. The evolution of open quantum systems in this framework is commonly described through the use of Kraus operators. This approach accounts for the non-unitary evolutions. The use of Kraus operators provides a significant advantage in simulating the evolution of open quantum systems and the master equation of open quantum systems. Nonetheless, the analytical solution of the master equation is often difficult; thus, a numerical method is required to analyse the evolution of the system. The presented numerical analysis of the master equation is based on the quantum trajectory theory. Using the quantum trajectory theory approach, instead of attempting to solve the entire differential equation at once, this method uses the average of multiple trajectories to approximate the dynamics of the system as function of time. The numerical solution enables the simulation of the evolution of a quantum system by assuming that the system's state changes randomly in response to certain conditions. This framework is essential in the field of quantum optics, which studies the quantum-level behaviour of light and matter, providing a realistic treatment of the evolution of quantum systems in the presence of environment interaction.

Chapter 4

An open quantum system description of one-cavity networks

Quantum jump metrology has emerged as a promising technique for enhancing the precision of phase shift measurements in light pathways beyond the SQL. In this approach, an optical cavity inside a quantum feedback loop, that was treated as an open quantum system, is utilised to deduce information about the phase shift difference between two light pathways [13]. In this model, the phase shift measurement accuracy was found to exceed the SQL. The absence of entanglement in the methodology is a crucial element in their quantum jump metrology scheme. Moreover, the quantum jump approach is motivated by the limitations of standard metrology and standard quantum metrology in terms of experimental implementation or extending the schemes to more complex networks. The scheme exhibits potential for quantum metrology by using readily available linear optics and scaling it to complex networks is possible.

In this chapter, we introduce a theoretical framework for analysing the dynamics of a single cavity network as an open quantum system. To establish the theoretical groundwork for the subsequent proposed scheme, we begin by examining the fundamental characteristics of coherent states, which are being employed

as a resource in the single cavity network. Next, we will proceed to discuss the effect of the instantaneous quantum feedback loop on the optical network. Subsequently, we proceed with defining the evolution of the optical network through the use of the quantum jump metrology approach and quantum trajectory theory. We thoroughly examine the system dynamics in two scenarios: one in which photon detection is absent, and another in which photon detection is present. Subsequently, we employ the quantum jump methodology to examine the impact of quantum feedback on both the master equation and the dynamics of the system. Additionally, we explore the behaviour of the trajectories of the network under varying initial states of the cavity and quantum feedback pulse strength. Finally, we discuss the evaluation of the scaling of the network in a phase shift measurement using the one-cavity optical network.

4.1 One-cavity network

In the context of an optical cavity that is subject to external laser driving and quantum feedback, all interactions have been designed such that the quantized electromagnetic field confined within the optical cavity is maintained in a coherent state at all times. In the following, we present the theoretical framework characterising the dynamics of the stated coherent states in the absence of photon emission and in the event of photon emission. Moreover, we shall conduct a comprehensive analysis of the mentioned scheme, with the aim of utilising it subsequently for the purpose of benchmarking more complex measurement schemes. The one-cavity optical network that is prepared in a coherent state is placed inside a quantum feedback loop, as shown in Fig. 4.1. The optical network consists of a single cavity, a phase shifter and a photon detector. In the first stage, the optical cavity is prepared in a coherent state by applying a laser pulse that is affected by presence of the phase shifter in front of the cavity. In the second stage, the phase shifter is removed and the optical cavity is excited by a laser source that is triggered instantaneously upon the detection of a photon at the detector. The presence of the phase shifter in the first stage has an impact on the

(a)

(b)
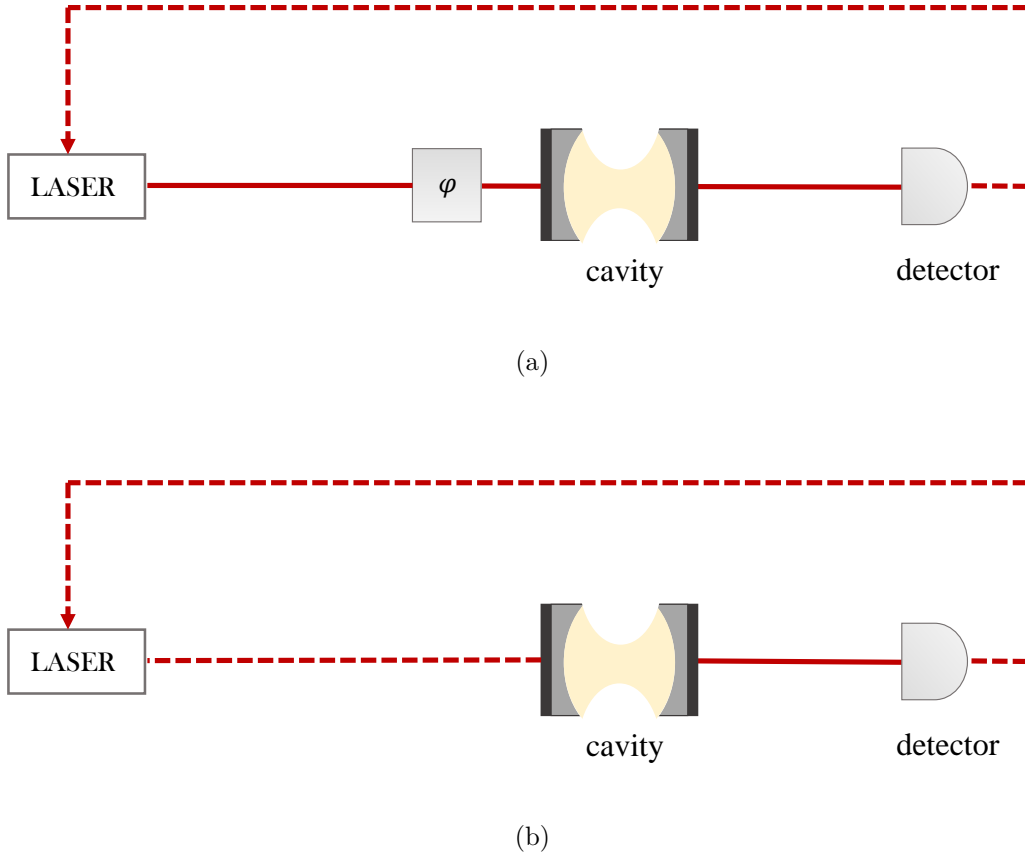
Figure 4.1: A schematic view of a single optical cavity inside an instantaneous quantum feedback loop. Here, the optical cavity is driven using a laser source, and the photons leaking from the cavity are detected by a photon detector. (a) In the first stage, the state of the cavity is prepared in a coherent state $|\gamma\rangle$ by applying a laser where the state of the cavity is affected by the phase shift φ in front of the cavity. (b) In the second stage, an instantaneous feedback laser pulse is applied when a photon leaks from the cavity and is detected by the detector.

coherent state of the cavity. The determination of the relative phase between the initial state of the cavity and the state of the displaced cavity field subsequent to the application of the feedback laser pulse can be determined through the photon statistics observed at the detector.

4.1.1 Coherent state

In the quantum optical network inside a quantum feedback loop, the cavity is prepared in a coherent state. Coherent states are specific quantum states that have properties similar to classical states. Therefore, they are often thought to be semi-classical states since they are easier to prepare compared to other quantum states [103]. The key difference that distinguishes coherent states from other quantum states is the time evolution of the system state that is set to interact with the surrounding environment. For instance, let us consider a lossy cavity prepared in a coherent state, in which the photon emission is monitored via a photon detector. In the case of a photon detection, there is no change in the cavity state undergoing photon emission since the coherent state $|\gamma\rangle$ is an eignestate of the annihilation and creation operators $c/c^{\dagger}$ as shown in Fig. 4.2. Furthermore, supposing the coherent state evolves under the non-Hermitian operator H_{eff}, then the coherent state decay to vacuum $|0\rangle$ after a long time if no photon is detected as $\left| e^{i\hbar H_{eff}\Delta t}\gamma \right\rangle$, as illustrated in Fig. 4.3. This peculiar behaviour of the coherent states is a consequence of the Poissonian statistics nature of the coherent states.

To better understand the unintuitive behaviour of coherent states, let us examine the probability of two events occurring: first, the probability of having n photons in the field knowing that a photons have been detected. The second probability is the probability of detecting a photons knowing that n photons are present in the field. Let us look at the conditional probability that the field has n photons when a photon a has been detected, $p(n|a)$ at time $t + \Delta t$. Using Baye's law, it is possible to determine the conditional probability $p(n|a)$ by knowing the probability of detecting a photons when the field has exactly n photons $p(a|n)$. If the number of photons present at a certain time t is known, then the probability to detect a photons is $p(a|n) = \kappa n \Delta t$. Here, κ is the decay rate, n is the total number of photons at time t. Thus, the conditional probability $p(n|a)$ reads [99]

$$p(n|a) = p(n)\frac{p(a|n)}{p(a)} \, . \tag{4.1}$$

where Eq. (4.1) is deduced from the relation $p(n, a) = p(a|n)p(n) = p(n|a)p_a$.
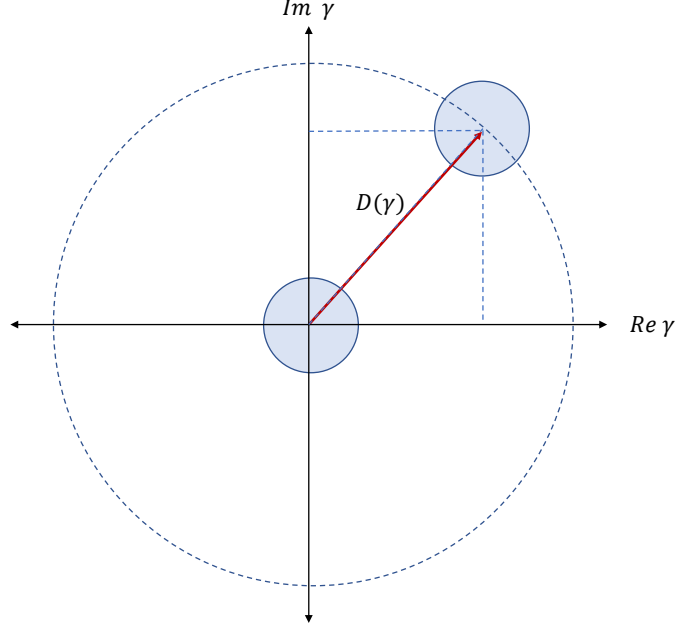
Figure 4.2: The action of the displacement operator $D(\gamma)$ on the coherent state $|\gamma\rangle$ is represented by the red arrow from the origin to the position $|\gamma|$. Here, $D(\gamma) = |\gamma_0 + \gamma\rangle$, since $\gamma_0 = 0$, then $D(\gamma) = |\gamma\rangle$.

Thus, the conditional probability that the field has n photons when a photons has been detected, $p(n|a)$ is given by

$$p(n|a) = \frac{e^{-\bar{n}}(\bar{n})^{n-1}}{(n-1)!} = p(n-1).$$ (4.2)

Here, a priori probability of detecting photon in time interval Δt is $p_a = \kappa \bar{n} \Delta t$ and the probability that the field has n photons at time t where the mean value of photons $\bar{n}$ is given by a priori Poissonian distribution [99],

$$p(n) = \frac{e^{-\bar{n}}\bar{n}^n}{n!}.$$ (4.3)

Hence, by examining Eq. (4.2), we can deduce that since detecting a single photon shifts the prior photon distribution number before the detection by $\bar{n} + 1$, and the conditional probability that the field has n photons when a photons has been detected, $p(n|a)$ reduces the number of photons in the field by unit quanta. These
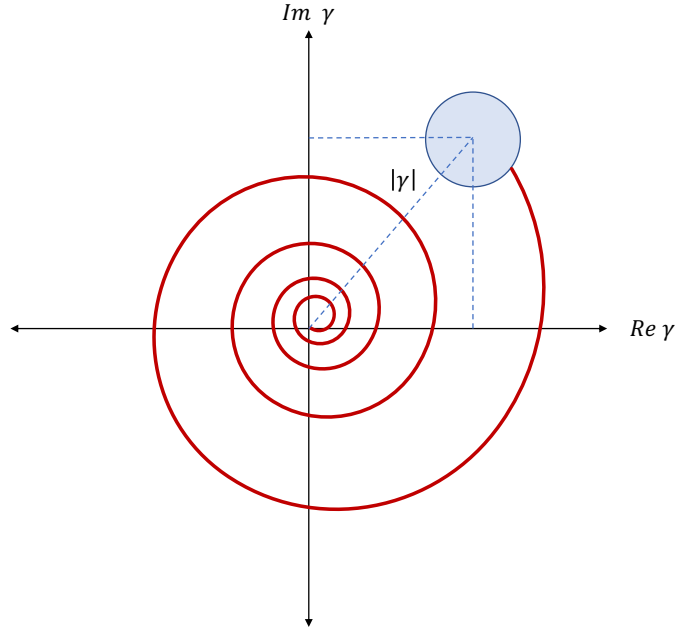
Figure 4.3: The evolution of the coherent state in case of no photon emission, the coherent state decays in time, and that is represented by the spiral motion towards the origin. Here the evolution is governed by $|\gamma\rangle \rightarrow \left|\gamma e^{-\kappa \Delta t/2}\right\rangle$

two events cancel one another out, keeping the coherent state unchanged in the case of photon detection.

Furthermore, looking at the one-cavity network, in the absence of photon detection, the state of the cavity field evolves according to the non-Hermitian Hamiltonian $H = 1 - i\hbar\kappa c^{\dagger}c/2$, where $c/c^{\dagger}$ denotes the annihilation and creation operators respectively, where the no photon detection shifts the priori probability towards a smaller photon distribution number.

Taking these properties into consideration, the coherent state resembles a competent candidate to be used in quantum jump metrology since the state is not affected by quantum jumps, and the evolved state can be obtained by calculating the coarse grained time sequential evolution while maintaining the state of the system in a purely coherent state.

In the following, c denotes the annihilation operator for a single photon inside

an optical cavity. Since photons are bosons, c and $c^\dagger$ obey the commutator relation

$$[c, c^\dagger] \;=\; 1 \,. \tag{4.4}$$

The coherent states $|\gamma\rangle$, where γ is a complex number, are the eigenstates of c with eigenvalue γ,

$$c\,|\gamma\rangle = \gamma\,|\gamma\rangle \,. \tag{4.5}$$

Thus, the expectation value $\langle n \rangle$ of the photon number of the operator $n = a^\dagger a$ equals

$$\langle n \rangle = \langle\gamma|\, c^\dagger c\, |\gamma\rangle = |\gamma|^2 \,. \tag{4.6}$$

Expanding the coherent state in terms of the Fock state basis as [120]

$$|\gamma\rangle = \exp\left(-\frac{1}{2}|\gamma|^2\right)\sum_{n=0}^{\infty}\frac{\gamma^n}{\sqrt{n!}}\,|n\rangle \,. \tag{4.7}$$

Here, $|n\rangle$ is the state with exactly n photons inside the resonator. When prepared in a coherent state $|\gamma\rangle$, the mean number of photons inside the cavity equals $|\gamma|^2$.

4.1.2 Instantaneous quantum feedback

The scheme of the one-cavity network has been incorporated within an instantaneous quantum feedback loop. In addition to the phase shifter before the cavity, the feedback loop acts as an additional factor that makes photon statistics dependent on the photons detected by the detector. In other words, it enhances the correlations between the measurements of the photons and the state of the cavity. For a single optical cavity inside a quantum feedback loop, as seen in Fig. 4.1, we assume in the following that the emission of a photon might trigger an instantaneous feedback pulse, i.e. a very strong, short, resonant laser pulse. Moving to the interaction picture allows for microscopic treatment of the evolution of the open quantum system. If the feedback is triggered faster than the evolution time duration of the density matrix of the system, then we define an instantaneous feedback laser beam. In the interaction picture with respect to the

free Hamiltonian $H_0 = \hbar\omega_0 c^\dagger c$, where ω_0 denotes the cavity frequency, the laser Hamiltonian equals

$$H_\mathrm{I} = \frac{\hbar\Omega}{2}\,(c + c^\dagger) \tag{4.8}$$

where Ω denotes the laser Rabi frequency and results in the time evolution operator

$$U_\mathrm{I}(t,0) = \exp\left[-\frac{\mathrm{i}}{2}\Omega(c + c^\dagger)t\right]. \tag{4.9}$$

A closer look at this equation shows that $U_\mathrm{I}(t,0)$ coincides with the displacement operator

$$D_c(\gamma_0) = \mathrm{e}^{\gamma_0 c^\dagger - \gamma_0^* c}, \tag{4.10}$$

with $\gamma_0 = -(\mathrm{i}/2)\Omega t$. If the feedback pulse is much shorter than the mean time between photon emissions, spontaneous emission can be neglected while the feedback pulse is applied, and we can describe its effect by simply applying the unitary operator $U_\mathrm{I}(t,0) = D_c(\gamma_0)$ to the state of the optical resonator.

Next, we study the effect of this operator on a coherent state $|\gamma\rangle$, since the states we are primarily considering in our scheme are coherent states. To do so, we first analyse the effect of the displacement operator $D_c(\gamma_0)$ on the vacuum state $|0\rangle$ [120]. Using the Baker–Campbell–Hausdorff (BCH) theorem, which implies

$$\mathrm{e}^{A+B} = \mathrm{e}^A\,\mathrm{e}^B\,\mathrm{e}^{-1/2[A,B]}, \tag{4.11}$$

one can show that $D_c(\gamma_0)\,|0\rangle$ equals

$$D_c(\gamma_0)\,|0\rangle = \mathrm{e}^{\gamma_0 c^\dagger}\,\mathrm{e}^{-\gamma_0^* c}\,\mathrm{e}^{-1/2|\gamma_0|^2}\,|0\rangle. \tag{4.12}$$

Taking into account that $(c^\dagger)^n\,|0\rangle = \sqrt{n!}\,|n\rangle$, this equation can be used to show that

$$D_c(\gamma_0)\,|0\rangle = \exp\left(-\frac{1}{2}|\gamma_0|^2\right)\sum_{n=0}^{\infty}\frac{\gamma_0^n}{n!}(c^\dagger)^n\,|0\rangle = |\gamma_0\rangle. \tag{4.13}$$

Hence, displacing the vacuum state $|0\rangle$ by $D_c(\gamma_0)$ transfers the vacuum state into the coherent state $|\gamma_0\rangle$.

Using Eq. (4.11) again, we can show that the action of consecutive displacement operators is

$$D_c(\gamma_0)D_c(\gamma) = D_c(\gamma_0 + \gamma)\, e^{i\,\mathrm{Im}(\gamma\gamma_0^*)}\,. \tag{4.14}$$

Applying the displacement operator $D_c(\gamma_0)$ to the coherent state $|\gamma\rangle$ therefore yields the coherent state

$$\begin{aligned}
D_c(\gamma_0)\,|\gamma\rangle &= D_c(\gamma_0)D_c(\gamma)\,|0\rangle \\
&= e^{i\,\mathrm{Im}(\gamma\gamma_0^*)}\,|\gamma + \gamma_0\rangle\,. \tag{4.15}
\end{aligned}$$

In the following calculations, we can ignore the overall phase factor $e^{i\,\mathrm{Im}(\gamma\gamma_0^*)}$ since the cavity remains always in a coherent state. It always corresponds to a global phase with no physical consequences. In other words, applying the displacement operator $D_c(\gamma_0)$ changes the coherent state $|\gamma\rangle$ effectively into the coherent state $|\gamma + \gamma_0\rangle$.

4.1.3   The quantum jump approach

Considering the cavity as an open quantum system that couples to the surrounding radiation field, it can be described by the quantum jump approach [106]. In the following, we use this approach to model all the different types of dynamics of an optical cavity inside a quantum feedback loop. Since the cavity field remains in a coherent state, we only consider the specific dynamics of these states.

4.1.3.1   No photon evolution

In the absence of photon emission, the coherent state of the cavity progressively decays towards the vacuum state, because the absence of photon detection indicates that there are fewer photons in the cavity than were initially anticipated. The quantum jump method shows that the electromagnetic field within the cavity field evolves in the interaction picture with respect to its free Hamiltonian $H_0 = \hbar\omega_{\mathrm{cav}}\,c^\dagger c$. The conditional non-Hermitian Hamiltonian of the evolution of

the coherent cavity reads

$$H_{\text{cond}} = -\frac{\text{i}}{2}\hbar\kappa c^{\dagger}c \,. \tag{4.16}$$

Here, $\hbar\omega_{\text{cav}}$ denotes the energy of a single cavity photon, and κ denotes its spontaneous decay rate. In the Fock basis, H_{cond} can be written as

$$H_{\text{cond}} = -\frac{\text{i}}{2}\hbar\kappa \sum_{n=0}^{\infty} n \, |n\rangle \langle n| \,. \tag{4.17}$$

Hence, its unitary time evolution operator reads

$$U_{\text{cond}}(t + \Delta t, t) = \sum_{n=0}^{\infty} \exp\left(-\frac{1}{2}\kappa n \Delta t\right) |n\rangle \langle n| \,. \tag{4.18}$$

Here, $\hbar$ is set to be 1. Moreover, in the quantum jump approach probability for no photon detection in a short time interval $(t, t + \Delta t)$ equals

$$P_0(\Delta t) = \|U_{\text{cond}}(t + \Delta t, t) \, |\psi(t)\rangle\|^2 \,, \tag{4.19}$$

where $|\psi(t)\rangle$ denotes the (normalised) state vector of the cavity field at time t. Since H_{cond} is a non-Hermitian Hamiltonian, its time evolution operator does not preserve the norm of a state vector, and the right hand side of Eq. (4.19) is in general smaller than one. In fact, H_{cond} has been constructed such that the right hand side equals $P_0(\Delta t)$.

Now let us have a closer look at what this implies for an initial coherent state $|\gamma(t)\rangle$. Under the condition of no photon emission, the normalised coherent state of the cavity, up to some normalisation constant, at time $t + \Delta t$ equals

$$|\gamma(t + \Delta t)\rangle = U_{\text{cond}}(t + \Delta t, t) \, |\gamma(t)\rangle \,. \tag{4.20}$$

Using the definition of the operator $U_{cond} = \text{e}^{-\frac{i}{\hbar} H_{cond}\Delta t}$, where the conditional non-Hermitian Hamiltonian H_{cond} is defined in Eq. (4.17), then the coherent state in Eq. (4.20) reads

$$|\gamma(t + \Delta t)\rangle = \exp\left(-\frac{i}{\hbar} - \frac{i}{2}\hbar\kappa \sum_{n=0}^{\infty} n \, |n\rangle \langle n| \, \Delta t\right) \exp\left(-\frac{1}{2}|\gamma|^2\right) \sum_{n=0}^{\infty} \frac{\gamma^m}{\sqrt{m!}} \, |m\rangle \,. \tag{4.21}$$

Rearranging Eq. (4.21), we arrive to the following expression,

$$|\gamma(t + \Delta t)\rangle = \exp\left(\frac{-\mid\gamma\mid^2}{2}\right) \sum_{n=0}^{\infty} \exp\left(-\frac{1}{2}\kappa\Delta t m\right) \frac{\gamma^m}{\sqrt{m!}} |m\rangle$$

$$= \exp\left(\frac{-\mid\gamma\mid^2}{2}\right) \sum_{n=0}^{\infty} \frac{(e^{-\frac{1}{2}\kappa\Delta t\gamma})^m}{\sqrt{m!}} |m\rangle \ . \tag{4.22}$$

Using the above equations, we find that

$$|\gamma(t + \Delta t)\rangle = \exp\left(\frac{-\mid\gamma\mid^2}{2}(1 - e^{-\kappa\Delta t})\right) \left|e^{-\frac{1}{2}\kappa t}\gamma(t)\right\rangle \tag{4.23}$$

under the condition of no photon emission. Moreover, we find that the probability for no photon emission in $(t, t + \Delta t)$ is given by

$$P_0(\Delta t) = \exp\left(-|\gamma(t)|^2(1 - e^{-\kappa\Delta t})\right) \tag{4.24}$$

which is always between zero and one.

4.1.3.2   Photon emission

In case of the spontaneous leakage of a photon through the cavity mirrors, an energy quanta is lost from the resonator field. Its normalised state immediately after an emission at time t when prepared in a state $|\psi(t)\rangle$ is given by [121]

$$|\psi(t + \Delta t)\rangle = c\,|\psi(t)\rangle\,/\|c\,|\psi(t)\rangle\,\| , \tag{4.25}$$

where Δt denotes a short time interval. When a feedback loop is used and the detection of a photon triggers the application of a short strong laser pulse, the state of the cavity evolves instead such that

$$|\psi(t + \Delta t)\rangle = D_c(\gamma_0)c\,|\psi(t)\rangle\,/\|c\,|\psi(t)\rangle\,\| , \tag{4.26}$$

where γ_0 characterises the strength of the laser driving. Moreover, the quantum jump approach [121] tells us that the probability density $I(t)$ for an emission in $(t, t + \Delta t)$ equals

$$I(t) = \kappa\,\|c\,|\psi(t)\rangle\,\|^2 . \tag{4.27}$$

Here, κ denotes the spontaneous decay rate of the cavity. The above equations apply, as long as Δt is much smaller than $1/\kappa$, so that the feedback laser is considered instantaneous.

In this network scheme, we are especially interested in a system that remains always in a coherent state. Since coherent states are the eigenstates of the annihilation operator c, Eq. (4.25) shows that the state of the cavity will remain unchanged in case of an emission. Moreover, Eq. (4.26) simplifies to

$$|\gamma(t + \Delta t)\rangle = |\gamma(t) + \gamma_0\rangle \tag{4.28}$$

and the probability density $I(t)$ in Eq. (4.27) becomes

$$I(t) = \kappa \, |\gamma(t)|^2 \, , \tag{4.29}$$

if the state of the cavity equals $|\gamma(t)\rangle$ at time t.

4.1.4 Master equations

If we are only interested in the dynamics of ensemble averages and ignore the individual trajectories of every possible realisation of the experiment, it is easier to describe the resonator by its density matrix ρ_I in the interaction picture. Suppose that the cavity field is subjected to instantaneous feedback pulses with a displacement operator $D_c(\beta)$. Then, the density matrix in the interaction picture $\rho_\mathrm{I}(t + \Delta t)$ a short time Δt after the system was prepared in $\rho_\mathrm{I}(t)$, equals [14, 121]

$$\rho_\mathrm{I}(t + \Delta t) = P_0(\Delta t) \, \rho_\mathrm{I}^0(t + \Delta t) + P_1(\Delta t) \, \rho_\mathrm{I}^1(t + \Delta t) \, . \tag{4.30}$$

In the above equation, the first term represents the evolution of the cavity state in the absence of photon emission, and the second term takes into account the cavity evolution under photon emission. The density matrix can be written in terms of the quantum optical master equation as,

$$\begin{aligned}
\rho_\mathrm{I}(t + \Delta t) & = U_\mathrm{cond}(t + \Delta t, t)\rho_\mathrm{I}(t)U_\mathrm{cond}^\dagger(t + \Delta t, t) \\
& \quad + \kappa c \rho_\mathrm{I}(t) c^\dagger (1 - \eta)\Delta t + \eta \kappa D(\beta) c \rho_\mathrm{I}(t) c^\dagger D^\dagger(\beta) \, .
\end{aligned} \tag{4.31}$$

Here, η is the efficiency to detect photon leakage out of the cavity in the case of a photon detection with finite efficiency with decay rate κ. For small Δt,

$$\dot{\rho}_{\mathrm{I}}(t) = \frac{\rho_{\mathrm{I}}(t + \Delta t) - \rho_{\mathrm{I}}(t)}{\Delta t} . \tag{4.32}$$

Hence, the master equation describing the evolution of the system with the instantaneous feedback laser is given by

$$\begin{aligned}
\dot{\rho}_{\mathrm{I}} &= -\frac{\mathrm{i}}{\hbar} \left[H_{\mathrm{cond}} \rho_{\mathrm{I}}(t) - \rho_{\mathrm{I}}(t) H_{\mathrm{cond}}^{\dagger} \right] \\
&\quad + (1 - \eta) \kappa c \rho_I(t) c^{\dagger} + \eta \kappa D(\beta) c \rho_I(t) c^{\dagger} D^{\dagger}(\beta) .
\end{aligned} \tag{4.33}$$

Substituting the conditional Hamiltonian H_{cond} in Eq. (4.16) into Eq. (4.33), and setting $\hbar$ to be unity, yields

$$\dot{\rho}_{\mathrm{I}} = \kappa \left[(1 - \eta) c \rho_{\mathrm{I}} c^{\dagger} + \eta D(\beta) c \rho_{\mathrm{I}} c^{\dagger} D^{\dagger}(\beta) - \frac{1}{2} c^{\dagger} c \rho_{\mathrm{I}} - \frac{1}{2} \rho_{\mathrm{I}} c^{\dagger} c \right] , \tag{4.34}$$

which is a master equation of Lindblad form.

4.2 Possible trajectories

The complex dynamics of the cavity state may be illustrated through an investigation of the system state trajectories of the state of the cavity as a function of time for various feedback pulse strengths while maintaining the same initial cavity state. Fig. 4.4(a)–(c) shows a simulation of the trajectories that exhibit quantum jumps. Upon observation of the trajectories for various values, it is evident that the trajectories exhibit a significant dependence on the feedback pulse strength. Moreover, in the case of a low feedback pulse, the majority of trajectories ultimately undergo exponential decay over time, resulting in a limited number of photon emissions, as shown in Fig. 4.4(a). However, increasing the feedback pulse results in the emergence of novel trajectory paths. In Fig. 4.4(b), it is observed that the state of cavity dynamics becomes increasingly complex. It can be stated that certain trajectories demonstrate exponential decay, whereas others appear to experience exponential growth and periods of emission and periods of no-emission. Nevertheless, it is observed that in Fig. 4.4(c), a significant number

of trajectories exhibit exponential evolution, which is indicative of a strongly driven optical cavity due to the presence of many strong feedback pulses.

(a)

(b)

(c)
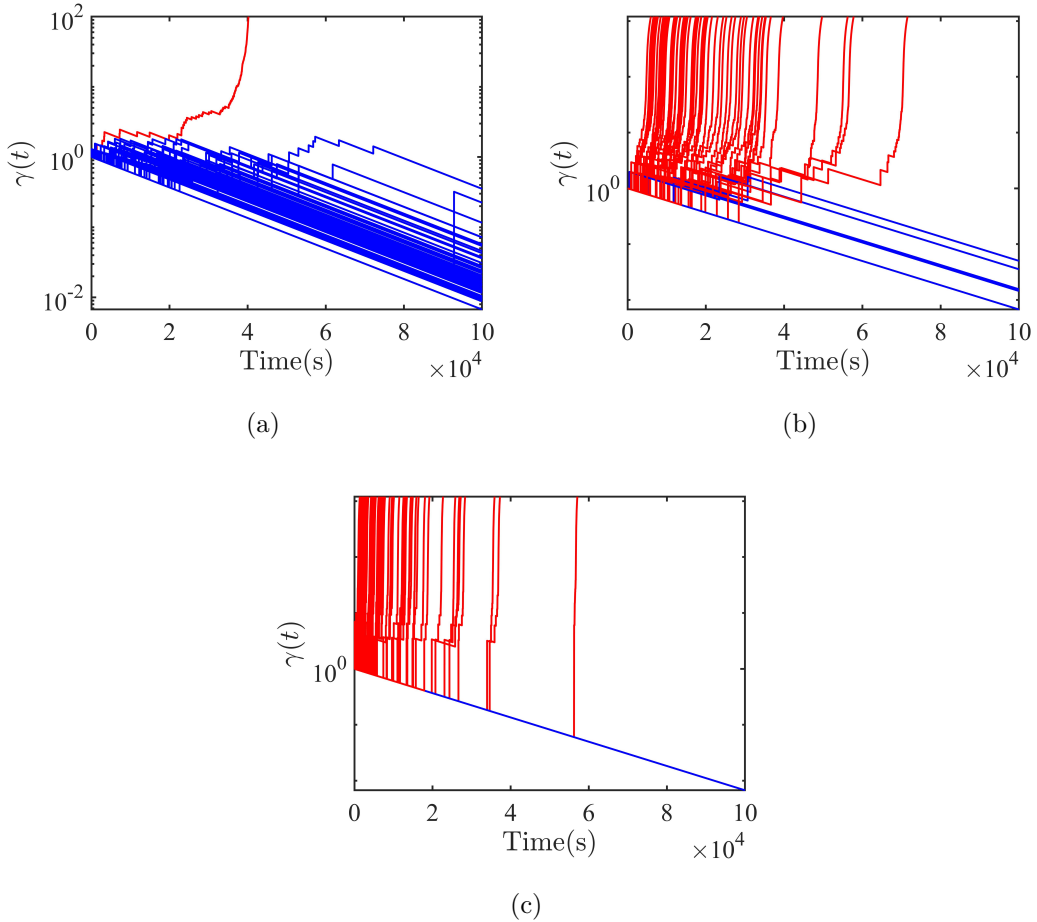
Figure 4.4: The possible trajectories generated by driving a single optical cavity inside a quantum feedback loop in a y-log axis for a fixed initial cavity state and varying laser pulse strength. Here is the plot of the cavity state $\gamma(t)$ as a function of time for feedback strength equal (a) $\beta = 0.3$ (b) $\beta = 1$ and (c) $\beta = 3$. Here, the initial state of the cavity is $\gamma_0 = 1$, phase shift $\varphi = 2\pi$, time step $\Delta t = 10^{-4}\kappa^{-1}$.

Furthermore, Fig. 4.5 shows the effect of varying the initial state of the cavity, while maintaining a constant feedback laser intensity. In Fig. 4.5 (a), the majority of trajectories decay exponentially to vacuum because the initial state of the cavity is low compared to the feedback laser; consequently, the probability that

the cavity field becomes excited is low. In Fig. 4.5(b), the trajectories exhibit two distinct dynamics: some decay to vacuum while the others diverge exponentially, while occasionally emitting some photons. This is because the initial cavity state is comparable to the feedback laser strength. In Fig. 4.5(c), the majority of trajectories diverge exponentially, indicating that the cavity is highly excited due to the presence of a significant number of photons despite the low feedback strength.

The trajectories of the state of the cavity as a function of time illustrated in Fig. 4.4 and Fig. 4.5 indicate the complexity of the dynamical evolution of the cavity under the influence of the quantum feedback pulses.

4.3   Parameter estimation performance

To estimate the phase shift measurements for a single cavity network, the second order correlation function $g^{(2)}(t_2, t_1)$ over a time interval T, is found to be the best network phase-dependent signal. The signal $g^{(2)}(t_2, t_1)$ was calculated numerically by averaging over large number of trajectories. Here, the second order correlation function reads [64]

$$g^{(2)}(t_2, t_1) = \frac{I(t_2|t_1)}{I(t_1)} \, , \tag{4.35}$$

where $I(t_2|t_1)$ is the probability of detecting a photon at t_2 conditioned on the detection of a photon at t_1.

More concretely, the scaling of the previously mentioned optical network was evaluated using the second-order correlation function $g^{(2)}(T, 0)$ between the initial time $t = 0$ and total time T averaging over a large number of trajectories as the phase dependant signal [64]. Therefore, the scaling was evaluated using error propagation as follows

$$\Delta(\hat{\varphi}) = \frac{\Delta O}{|\frac{\partial O}{\partial \varphi}|} \, , \tag{4.36}$$

where the variance and the visibility of the signal were determined numerically, using simulations of the optical cavity by quantum jump method.

(a)

(b)

(c)

Figure 4.5: The possible trajectories generated by driven a single optical cavity inside a quantum feedback loop in a y-log axis for a fixed laser pulse strength and varying initial cavity state. Here is the plot of the cavity state $\gamma(t)$ as a function of time: (a) $\gamma_0 = 0.3$ (b) $\gamma = 1$ and (c) $\gamma = 2.6$. Here the initial state of the cavity is $\beta = 0.5$, phase shift $\varphi = 2\pi$, time step $\Delta t = 10^{-4}\kappa^{-1}$.

A numerical simulation of the optical network revealed that the accuracy of the phase shift measurement as a function of total time T shows a scaling beyond the SQL, more specifically at phase shift $\varphi = \pi$, the scaling of the network is given by [14]

$$\Delta(\hat{\varphi}) \propto T^{-0.71} . \tag{4.37}$$

61

Furthermore, an examination of the Fisher information of such a measurement scheme revealed that the quantum jump metrology method produces temporal correlations between sequential measurements. These correlations allow for a scaling beyond the SQL. Thus, the presence of temporal correlations in this optical network scheme results in a measurement enhancement for parameter estimation. These correlations is believed to be the result of the non-ergodicity of the optical system as a result of the quantum feedback loop [13, 14, 64].

4.4 Summary

In this chapter, we presented the theoretical framework of the one-cavity optical network inside an instantaneous quantum feedback loop for phase shift measurements. We reviewed the fundamental properties of coherent states, focusing on the Poissonian photon statistics of the photon number distribution of coherent states within a lossy optical cavity. The effect of quantum feedback on the coherent cavity field was then discussed. Then, we presented the quantum jump approach for simulating the dynamics of the optical network and established an overall mathematical description of the system for the two distinct events of photon detection and the case of no photon detection. Moreover, we included a discussion of the quantum jump method to analyse the evolution of the cavity state during the two mentioned events. In addition, we presented the individual trajectories of the cavity state as a function of time for varying feedback laser intensities and initial cavity states. We observed a significant quantum feedback effect on photon detection, which, in turn, impacted the cavity state. The three distinct dynamics resulting from various selections of the initial cavity state and the feedback pulse intensity revealed the significance of selecting the simulation parameters with care to achieve enhancement in phase shift measurements. Finally, we reviewed the assessment of the one-cavity scheme in terms of performance and maximum attained accuracy compared to the SQL. The one-cavity network was found to beat the SQL for the selected measurement signal.

Part II

Novel Results

Chapter 5

A two-mode cavity network with quantum feedback

The quantum optics scheme that we are proposing here is founded on the principles of quantum jump metrology and is further enhanced by the implementation of a quantum feedback loop. This innovative approach holds great promise for advancing the field of quantum information processing since it has the capability of achieving parameter estimation enhancement without relying on entanglement. By utilising the unique properties of quantum mechanics, our scheme offers a novel way of achieving high-precision measurements. Through continuously monitoring an open quantum system and conducting a sequence of measurements, we anticipate surpassing the SQL, as shown in Fig. 2.5. The proposed scheme, as presented in Fig. 5.1, is the optical cavity network that utilises quantum jump metrology for measurement enhancement. Temporal correlations are employed as a valuable resource in this quantum optical scheme in which a series of repeated measurements are performed to continuously monitor the dynamic evolution of the system to generate and reveal these correlations. This approach appears to be able to reach an accuracy that exceeds the SQL without requiring entangled photons. In Fig. 2.5, we show the proposed scheme of quantum jump metrology. Such a scheme uses time as a resource, in which multiple sequential measurements are done to monitor the evolving system.

Using the quantum jump formalism, we measure the difference φ between two phases φ_1 and φ_2, corresponding to two different pathways through a linear optics setup. The proposed scheme involves the use of two cavities inside a quantum feedback loop, and the measurement of the phase shift difference between two light paths is performed, achieving quantum scaling better than SQL by taking advantage of the temporal correlations in an open quantum system with sequential measurements. In the proposed scheme, the state of the system depends on the phase difference, and the generalised measurement should also depend on the phase difference. The outcomes obtained are non-Markovian and highly correlated, which allow for a potential practical use of the scheme. Nevertheless, the scheme that we propose here relies only on coherent states, yet it is capable of producing correlated photon statistics and thus surpassing the standard scaling due to the presence of quantum feedback. Hence, as well as demonstrating a simple scheme with enhanced sensing capabilities, our proposal also demonstrates the power of using quantum feedback to induce quantum effects, even in 'classical-like' states, such as coherent states. The observed outcomes exhibit significant quantum correlations, which could potentially facilitate their practical implementation in quantum technologies.

This chapter provides an overview of the principal theoretical methods used to model the experimental configuration described in Section 5.1. The system maintains a coherent state when analysing the cavities that are solely driven by laser pulses, resulting in displacements of the cavity field. In the subsequent analysis, we will investigate the dynamical behaviour of the coherent states, both in the case of no photon emission and photon emission. In addition, we provide quantum optical master equations that can be used to predict ensemble expectation values. In Section 5.2, the general dynamics of the two-cavity network are extensively discussed by analysing the influence of the variable parameters on the evolution of the optical cavities, using the quantum jump method. Then, in Section 5.3, we highlight the fundamental measurement protocol for the parameter estimation of the phase shift. Following that, we address the performance of the two-cavity network by evaluating the parameter estimation of the phase shift

measurement accuracy and the Fisher information scaling of the scheme. This chapter concludes in Section 5.4 with a comprehensive analysis of the simulation of the two-cavity network with variable parameters, highlighting the best set of variables that enables us to exceed the SQL effectively.
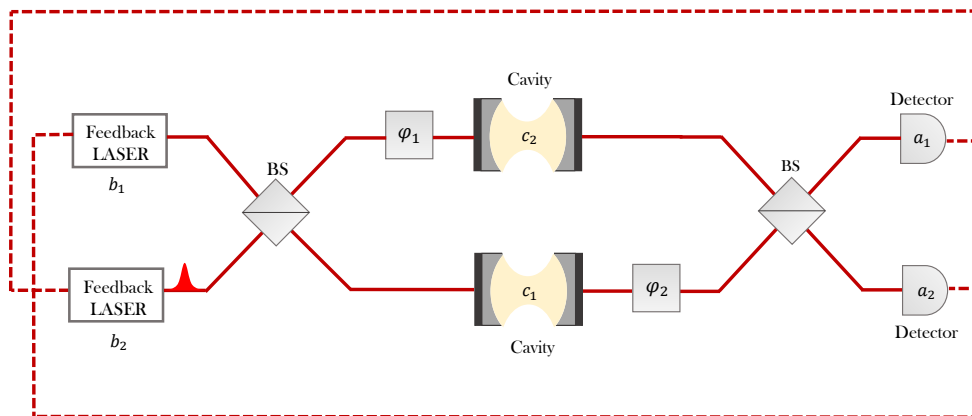
Figure 5.1: Two optical cavities are monitored through a linear optical network with photon detectors. Upon the detection of a photon, quantum feedback is triggered and applied to the cavities, also through a linear optics network. Throughout this section, we assume the feedback acts instantaneously after a photon detection. In this diagram and our subsequent analysis of the system, we consider the specific case of the dynamics presented in Section 5, in which feedback is triggered only in mode b_2 from a photon detection in detector 1 and only in mode b_1 from a photon detection in detector 2. The aim of the scheme is to estimate the uncertainty in the phase difference $\varphi = \varphi_1 - \varphi_2$ from the photon statistics in the detectors.

5.1   Theoretical modelling

In this section, we review the main tools for the theoretical modelling of the experimental setup shown in Fig. 5.1. As we simply consider cavities subject only

to laser driving, in the form of pulses resulting in displacements of the cavity field, the system remains in a coherent state. In the following, we take a closer look at the dynamics of these coherent states: under the condition of no photon emission and in the case of an emission. In addition, we introduce quantum optical master equations that can be used for the prediction of ensemble expectation values.

5.1.1 Multi-mode coherent states and transformation matrices

As mentioned above, in this section, we consider a network of two leaky optical cavities that are always kept in a coherent state. In Fock state representation, the coherent state $|\gamma_i\rangle$ of cavity i can be solely parametrised by a complex number γ_i such that

$$|\gamma_i\rangle = \exp\left(-\frac{|\gamma_i|^2}{2}\right) \sum_{n_i=0}^{\infty} \frac{\gamma_i^{n_i}}{\sqrt{n_i}} |n_i\rangle .\tag{5.1}$$

Here, $|n_i\rangle$ is the Fock state with exactly n_i photons in cavity i. If c_i is the annihilation operator for a single photon in cavity i, with $c_i |n_i\rangle = \sqrt{n_i} |n_i - 1\rangle$, then for coherent states, one can show that $c_i |\gamma_i\rangle = \gamma_i |\gamma_i\rangle$. Using this notation, as we shall see below, the state $|\psi(t)\rangle$ of both cavities at time t is always of the form

$$|\psi(t)\rangle = \bigotimes_{i=1,2} |\gamma_i(t)\rangle ,\tag{5.2}$$

and its dynamics can be modelled simply by tracking two complex numbers $\gamma_i(t)$. Hence, we can also express the state of the two cavities as

$$\underline{\gamma}(t) = \begin{pmatrix} \gamma_1(t) \\ \gamma_2(t) \end{pmatrix} .\tag{5.3}$$

In the following, we adopt a vector and matrix notation for convenience when considering photon counting and quantum feedback processes.

The experimental setup in Fig. 5.1 contains phase shifters and beamsplitters. Hence, quantum feedback pulses do not perturb the cavities directly. Similarly,

photons arriving at a detector do not come directly from a single cavity. To take this into account more easily, we denote the annihilation operator of the field mode seen by detector i in the following by a_i and the annihilation operator of the field mode affected by laser i by b_i. With respect to these alternative modes, the state $|\psi(t)\rangle$ of the cavities is given by the complex vectors

$$\underline{\alpha}(t) = \begin{pmatrix} \alpha_1(t) \\ \alpha_2(t) \end{pmatrix} , \quad \underline{\beta}(t) = \begin{pmatrix} \beta_1(t) \\ \beta_2(t) \end{pmatrix} \tag{5.4}$$

with the complex numbers $\alpha_i(t)$ and $\beta_i(t)$, such that $a_i|\alpha_i(t)\rangle = \alpha_i(t)|\alpha_i(t)\rangle$ and $b_i|\beta_i(t)\rangle = \beta_i(t)|\beta_i(t)\rangle$. To switch from one representation of the cavity network in Fig. 5.1 to another, we define transformation matrices M_{yx} with

$$\begin{pmatrix} y_1 \\ y_2 \end{pmatrix} = M_{yx} \begin{pmatrix} x_1 \\ x_2 \end{pmatrix} , \tag{5.5}$$

where $x_i, y_i = \alpha_i(t), \beta_i(t)$ and $\gamma_i(t)$ for the coefficients of the vectors, and where $x, y = a, b, c$ for the subscripts of the transition matrices M_{yx}. Below we have a closer look at these matrices that describe the effect of the beamsplitters and the phase shifters shown in Fig. 5.1. If we define the transformation matrices as

$$S_{\mathrm{BS}} = \frac{1}{\sqrt{2}} \begin{pmatrix} 1 & \mathrm{i} \\ \mathrm{i} & 1 \end{pmatrix} , \quad S_{\varphi_1} = \begin{pmatrix} 1 & 0 \\ 0 & \mathrm{e}^{\mathrm{i}\varphi_1} \end{pmatrix} , \quad S_{\varphi_2} = \begin{pmatrix} \mathrm{e}^{\mathrm{i}\varphi_2} & 0 \\ 0 & 1 \end{pmatrix} , \tag{5.6}$$

where S_{BS} is the beam splitter transformation matrix, S_{φ_1}, and S_{φ_2} are the phase shifter transformation matrices. Then, the transition matrices M_{cb}, M_{ac} and M_{ab} take the form

$$\begin{aligned} M_{cb} &= S_{\varphi_1} S_{\mathrm{BS}} = \frac{1}{\sqrt{2}} \begin{pmatrix} 1 & \mathrm{i} \\ \mathrm{i}\,\mathrm{e}^{\mathrm{i}\varphi_1} & \mathrm{e}^{\mathrm{i}\varphi_1} \end{pmatrix} , \\ M_{ac} &= S_{\mathrm{BS}} S_{\varphi_2} = \frac{1}{\sqrt{2}} \begin{pmatrix} \mathrm{e}^{\mathrm{i}\varphi_2} & \mathrm{i} \\ \mathrm{i}\,\mathrm{e}^{\mathrm{i}\varphi_2} & 1 \end{pmatrix} , \\ M_{ab} &= M_{ac} M_{cb} = \frac{1}{2} \begin{pmatrix} -\mathrm{e}^{\mathrm{i}\varphi_1} + \mathrm{e}^{\mathrm{i}\varphi_2} & \mathrm{i}\left(\mathrm{e}^{\mathrm{i}\varphi_1} + \mathrm{e}^{\mathrm{i}\varphi_2}\right) \\ \mathrm{i}\left(\mathrm{e}^{\mathrm{i}\varphi_1} + \mathrm{e}^{\mathrm{i}\varphi_2}\right) & \mathrm{e}^{\mathrm{i}\varphi_1} - \mathrm{e}^{\mathrm{i}\varphi_2} \end{pmatrix} . \end{aligned} \tag{5.7}$$

These defined matrices may now be utilised to simulate the system dynamics on various bases. Thus, the introduction of these transition matrices allows for

detailed monitoring of the evolution of the state of the cavities fields, the control of the feedback laser pulses and the photon statistics registered by the detectors.

5.1.2 The effect of quantum feedback

Suppose an instantaneous, strong laser pulse is applied directly to cavity i. Then the effect of this operation on the coherent state $|\gamma_i(t)\rangle$ of mode i in the c basis can be described by a displacement operator of the form

$$D_i^{(c)}(\beta) \;=\; \exp\left(\beta\, c_i^\dagger - \beta^*\, c_i\right), \tag{5.8}$$

where β is a complex number that describes the strength and phase of the feedback pulse and can assume any value. Taking this into account, one can show that the result is a change such that

$$\gamma_i(t) \;\to\; \gamma_i(t) + \beta. \tag{5.9}$$

However, in the experimental setup in Fig. 5.1, quantum feedback does not trigger a laser pulse that disturbs the cavities directly. Instead, because of the presence of a beamsplitter, each laser pulse usually affects the field in both cavities.

For simplicity, we take the feedback strengths of the laser pulses as constant in time, although it could be made time-dependent for further generality. This allows us to model the effect of the feedback by four complex numbers $\beta_i^{(d)}$, which characterise the quantum feedback strength generated by laser i upon detection of a photon in detector d with $d = 1, 2$. For convenience, we arrange these numbers into two vectors

$$\underline{\beta}^{(d)} \;=\; \begin{pmatrix} \beta_1^{(d)} \\ \beta_2^{(d)} \end{pmatrix}. \tag{5.10}$$

Given that the feedback is triggered by the detection of a photon in detector d, we observe the following effect of quantum feedback on the state $\underline{\gamma}(t)$ of the cavities

$$\underline{\gamma}(t) \;\to\; \underline{\gamma}(t) + M_{cb}\,\underline{\beta}^{(d)}. \tag{5.11}$$

69

Alternatively, in the bases of the detector modes, the state of the cavities changes such that

$$\underline{\alpha}(t) \quad \rightarrow \quad \underline{\alpha}(t) + M_{ab}\,\underline{\beta}^{(d)}\,. \tag{5.12}$$

These equations provide a comprehensive description of the quantum feedback required to numerically generate all possible trajectories of the cavity network shown in Fig. 5.1. The only variable that remains to be specified is the probability that a photon emitted will trigger a feedback pulse. In the following, for the sake of simplification, we will assume the detector efficiency η is ideal and ignore its possible dependence on time and the number of photons arriving at the detector. This assumption is well-justified if both detectors, like the majority of detectors, have a finite dark count rate [122, 123]. When this occurs, the first photon detected triggers the detector and prevents it from registering subsequent photons for a period of time. Here, we assumed that no additional photons would be detected until the end of the relevant time interval.

5.1.3 Master equations and quantum jump approach

Next, we study the effect of the possible leakage of photons through the cavity mirrors on the state of the resonator fields. Because of the presence of spontaneous photon emission, the calculation of expectation values for ensemble averages requires the introduction of a density matrix ρ. In what follows, we work in the detector basis a_d and define all subsequent evolutions and probabilities in terms of this, as it is most convenient for the numerical implementations that follow, although these quantities could in principle be calculated in any basis. For example, in the absence of quantum feedback, ρ evolves such that

$$\dot{\rho} \;\; = \;\; \sum_{d=1,2} \kappa_d\, a_d\, \rho\, a_d^\dagger - \frac{1}{2}\kappa_d \left[a_d^\dagger a_d, \rho\right]_+ , \tag{5.13}$$

where κ_d denotes the spontaneous decay rate of a single photon in the a_d mode, and $[a_d^\dagger a_d, \rho]_+$ denotes the anti-commutator. We are assuming an ideal detector with efficiency $\eta = 1$ and the effect of the feedback represented by the displacement operator. In the presence of quantum feedback, this master equation

70

changes into

$$\begin{aligned}
\dot{\rho} &= \sum_{d=1,2} \kappa_d \, D_2^{(a)}(\beta_2^{(d)}) D_1^{(a)}(\beta_1^{(d)}) a_d \, \rho \, a_d^\dagger D_1^{(a)\dagger}(\beta_1^{(d)}) D_2^{(a)\dagger}(\beta_2^{(d)}) \\
&\quad -\frac{1}{2}\kappa_d \left[a_d^\dagger a_d, \rho \right]_+ .
\end{aligned}$$
(5.14)

This equation takes into account that quantum feedback can be interpreted as a modification of the system-bath coupling, thereby resulting in a transformation of the Lindblad operators. The reason for this change of operators is that the emission of a photon is immediately followed by the application of the feedback pulse(s) [13, 14, 64]. In obtaining this equation, we have made the standard quantum optical approximations of Markovianity and a rotating wave approximation, while assuming classical driving fields for the laser pulses. In the following, we take a closer look at the unravelling of the above ensemble dynamics into individual quantum trajectories. These can be studied analytically relatively easily, especially if the cavities are initially prepared in a pair coherent state.

5.1.3.1 The no-photon time evolution

We first consider how the system evolves under the condition that there is no photon emission. To obtain the conditional no-photon evolution, we write the master equation in Eq. (5.14) as

$$\begin{aligned}
\dot{\rho} &= -\frac{\mathrm{i}}{\hbar} \left(H_{\mathrm{cond}}\rho - \rho H_{\mathrm{cond}}^\dagger \right) \\
&\quad + \sum_{d=1,2} \kappa_d \, D_2^{(a)}(\beta_2^{(d)}) D_1^{(a)}(\beta_1^{(d)}) a_d \, \rho \, a_d^\dagger D_1^{(a)\dagger}(\beta_1^{(d)}) D_2^{(a)\dagger}(\beta_2^{(d)})
\end{aligned}$$
(5.15)

with the conditional Hamiltonian H_{cond} provided by

$$H_{\mathrm{cond}} = -\frac{\mathrm{i}}{2}\hbar \sum_{d=1,2} \kappa_d \, a_d^\dagger a_d .$$
(5.16)

While the last terms in Eq. (5.15) describe dynamics of the subensembles of systems with a photon detection in the output port d, the first two terms describe the subensemble without an emission. In other words, the non-Hermitian Hamiltonian H_{cond} is the generator for time evolution of the experimental setup

in Fig. 5.1, conditioned on no photon emission. The corresponding time evolution operator

$$U_{\text{cond}}(t, t_0) = \exp\left(-\frac{\mathrm{i}}{\hbar} H_{\text{cond}}(t - t_0)\right) \tag{5.17}$$

reduces the norm of state vectors and can be used to calculate the probability $P_{00}(t, t_0)$ for no photon detection in both detectors in a time interval $[t_0, t]$. This probability equals

$$P_{00}(\Delta t) = \|U_{\text{cond}}(t, t_0)|\psi(t_0)\rangle\|^2. \tag{5.18}$$

for a given initial state $|\psi(t_0)\rangle$ and $\Delta t = t - t_0$. For example, given an initial pair coherent state $|\psi(t_0)\rangle = |\alpha_1\rangle |\alpha_2\rangle$ with respect to the modes a_1 and a_2 seen by the detector, one can show that

$$
\begin{aligned}
U_{\text{cond}}(t, t_0) |\alpha_1\rangle |\alpha_2\rangle &= \exp\left(\frac{-|\alpha_1|^2}{2}\left(1 - \mathrm{e}^{-\kappa_1 \Delta t}\right)\right) \\
&\quad \times \exp\left(\frac{-|\alpha_2|^2}{2}\left(1 - \mathrm{e}^{-\kappa_2 \Delta t}\right)\right) \\
&\quad \times \left|\alpha_1 \mathrm{e}^{-\frac{1}{2}\kappa_1 \Delta t}\right\rangle \left|\alpha_2 \mathrm{e}^{-\frac{1}{2}\kappa_2 \Delta t}\right\rangle.
\end{aligned} \tag{5.19}
$$

Hence, using the notation introduced in Section 5.1.1, we can summarise the effect of the no-photon time evolution of the field inside the cavities as $\underline{\alpha}(t) = M_{00}(t)\underline{\alpha}(t_0)$ with

$$M_{00}(\Delta t) = \begin{pmatrix} \mathrm{e}^{-\frac{1}{2}\kappa_1 \Delta t} & 0 \\ 0 & \mathrm{e}^{-\frac{1}{2}\kappa_2 \Delta t} \end{pmatrix}. \tag{5.20}$$

The probability of such an evolution occurring is

$$
\begin{aligned}
P_{00}(\Delta t) &= \exp\left[-|\alpha_1(t_0)|^2\left(1 - \mathrm{e}^{-\kappa_1 \Delta t}\right)\right] \\
&\quad \times \exp\left[-|\alpha_2(t_0)|^2\left(1 - \mathrm{e}^{-\kappa_2 \Delta t}\right)\right]
\end{aligned} \tag{5.21}
$$

due to Eq. (5.18).

5.1.3.2   Photon emission probabilities

Next, we calculate the probabilities of photon emission in a time interval of length Δt. Taking a closer look at the two factors in Eq. (5.21), we see that the probability for an individual detector mode i not to detect a photon equals

$$P_0^{(i)}(\Delta t) \;\; = \;\; \exp\left[-|\alpha_i(t_0)|^2 \left(1 - \mathrm{e}^{-\kappa_i \Delta t}\right)\right] . \tag{5.22}$$

Moreover, we know that the probability to find at least one photon in detector i is given by $1 - P_0^{(i)}(\Delta t)$. Thus, the probability of no photon in detector 1 and at least one photon in detector 2 equals

$$\begin{aligned} P_{01}(\Delta t) \;\; = \;\; & \exp\left[-|\alpha_1(t_0)|^2 \left(1 - \mathrm{e}^{-\kappa_1 \Delta t}\right)\right] \\ & \times \left(1 - \exp\left[-|\alpha_2(t_0)|^2 \left(1 - \mathrm{e}^{-\kappa_2 \Delta t}\right)\right]\right) . \end{aligned} \tag{5.23}$$

Analogously,

$$\begin{aligned} P_{10}(\Delta t) \;\; = \;\; & \left(1 - \exp\left[-|\alpha_1(t_0)|^2 \left(1 - \mathrm{e}^{-\kappa_1 \Delta t}\right)\right]\right) \\ & \times \exp\left[-|\alpha_2(t_0)|^2 \left(1 - \mathrm{e}^{-\kappa_2 \Delta t}\right)\right] \end{aligned} \tag{5.24}$$

is the probability of at least one photon in detector 1 and no photon in detector 2. To cover all possibilities (i.e. to have probabilities that sum to unity), we also consider in the following the probability

$$\begin{aligned} P_{11}(\Delta t) \;\; = \;\; & \left(1 - \exp\left[-|\alpha_1(t_0)|^2 \left(1 - \mathrm{e}^{-\kappa_1 \Delta t}\right)\right]\right) \\ & \times \left(1 - \exp\left[-|\alpha_2(t_0)|^2 \left(1 - \mathrm{e}^{-\kappa_2 \Delta t}\right)\right]\right) \end{aligned} \tag{5.25}$$

for the case in which at least one photon has been emitted into both detector modes.

For relatively short time intervals Δt, the presence of two photons in one detector becomes negligible, and the probabilities $P_{01}(\Delta t)$, $P_{10}(\Delta t)$ and $P_{11}(\Delta t)$ become the probabilities of having exactly one photon in mode 2, exactly one photon in mode 1 and exactly one photon in each mode, respectively to a good approximation, so long as $\Delta t \ll \kappa |\alpha_i|^2$. In fact, the probability $P_{11}(\Delta t)$ would

also be negligible by the same argument, as its first non-zero term when expanded is $O(\Delta t^2)$, compared to $O(\Delta t)$ for single photon emissions, but we nevertheless persist in keeping this term to maintain probabilities summing to exactly one, and to prevent the accumulation of numerical errors. In this case, the corresponding changes of the state vector $\underline{\alpha}(0)$ of the cavity fields can be described by transformation operators $M_{ij}(\Delta t)$, such that $\underline{\alpha}(t) = M_{ij}(\Delta t)\,\underline{\alpha}(0)$. To a very good approximation, the $M_{ij}(\Delta t)$ are given by

$$
\begin{aligned}
M_{01}(\Delta t)\,\underline{\alpha}(0) &= M_{00}(\Delta t)\left(\underline{\alpha}(0) + \underline{\beta}^{(2)}\right), \\
M_{10}(\Delta t)\,\underline{\alpha}(0) &= M_{00}(\Delta t)\left(\underline{\alpha}(0) + \underline{\beta}^{(1)}\right), \\
M_{11}(\Delta t)\,\underline{\alpha}(0) &= M_{00}(\Delta t)\left(\underline{\alpha}(0) + \underline{\beta}^{(1)} + \underline{\beta}^{(2)}\right),
\end{aligned}
\tag{5.26}
$$

with $M_{00}(\Delta t)$ given in Eq. (5.20). Specifically, we assume that the cavity field freely decays in the time interval of size Δt but is first displaced by the feedback. Therefore, as long as Δt is sufficiently small, according to the same assumption of $\Delta t \ll \kappa|\alpha_i|^2$, the exact moment of the feedback pulse does not significantly change the evolution of the system. For the simulations, the transition matrices, as defined in Eq. (5.7), may be needed in case that transition between bases is required We now have a complete toolbox for modelling quantum trajectories through piecewise evolution of the system, as suggested by standard quantum jump methods [124–126].

5.2   General dynamics and temporal correlations

In this section, we study the behaviour of the experimental setup in Fig. 5.1 in more detail to better understand how it can be used to estimate the phase $\varphi = \varphi_1 - \varphi_2$. We then consider the fundamental limits of the estimation accuracy that we can expect for the proposed cavity network based on the photon statistics.

5.2.1   Dynamics and quantum trajectories

In the proceeding discussions, we analyse the behaviour and the sensing capabilities of the cavity network shown in Fig. 5.1 for a specific example of quantum

feedback, which can be described by

$$\underline{\beta}^{(1)} = \begin{pmatrix} 0 \\ \beta_2^{(1)} \end{pmatrix}, \quad \underline{\beta}^{(2)} = \begin{pmatrix} \beta_1^{(2)} \\ 0 \end{pmatrix}. \tag{5.27}$$

As pointed out in the previous section, we treat the quantum feedback as approximately instantaneous. For simplicity, we also consider the case of perfect photon detection and assume that all photons are counted and trigger feedback pulses. Losses could be incorporated but do not largely affect the overall behaviour of the cavity network and are therefore neglected here [13]. As we shall see below, the performance of the measurement scheme that we propose here does not depend strongly on the exact number of emitted photons. It is, therefore, also widely independent of the detector efficiency η, as longs as η differs sufficiently from zero, which allows us to only study the case $\eta = 1$ for simplicity.
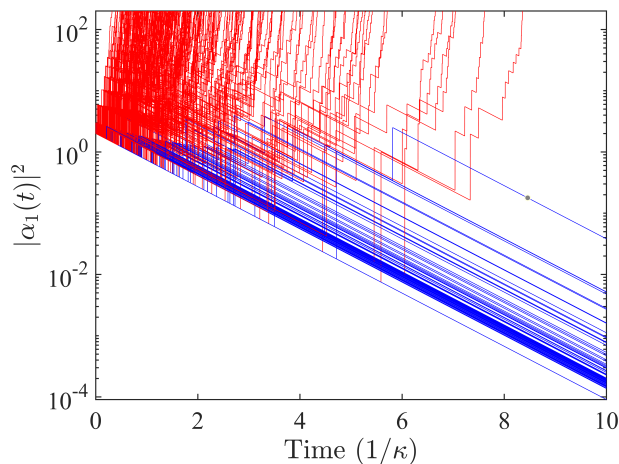
Figure 5.2:   Illustration of the dynamics of the state first cavity $\alpha_1(t)$ in the detector mode basis. Here we present 500 individual trajectories for initial parameters $\gamma_1(0) = \gamma_2(0) = 1$, quantum feedback as described by Eq. (5.27) with $\beta_2^{(1)} = 1$ and $\beta_1^{(2)} = 2$, $\kappa_1 = \kappa_2 = \kappa$, $\Delta t = 10^{-3}\kappa^{-1}$ and $\varphi = 0$. We show the population $|\alpha_1(t)|^2$ of detector 1. The difference in the cavity behaviour is clear, as some trajectories diverge, while others decay towards the vacuum, as signified by the different line shades.

Although the experimental setup that we analyse here always remains in a coherent state, its dynamics are nevertheless non-trivial. While optical cavities with continuous laser driving smoothly evolve into a steady state, the same does not always apply in the presence of quantum feedback. For example, when the feedback is in the form of strong laser pulses, the free decay of the cavity field is perturbed by 'kicks' to the dynamics. These kicks occur more often when there are more photons inside the resonator and hence, result in a divergence of the average photon number. This highly non-linear behaviour prevents us from obtaining a straightforward closed analytic solution to the master equation and its statistical moments, despite the cavities always being in a coherent state.

However, instead of studying the ensemble behaviour, considering the individual quantum trajectories of the system in Fig. 5.2 for cavity 1 reveals more subtle behaviour. In particular, in Fig. 5.2 we see the creation of two types of dynamics. In one case, we see a divergence of cavity photon numbers, with each feedback pulse making the state even more likely to emit another photon and thus diverging further due to subsequent feedback pulses. However, we also see trajectories that do not follow this evolution and decay towards the vacuum state, with only a small number of photon emissions. Generally, after a reasonable amount of time has passed, trajectories do not swap trajectory classes and clearly belong to one of two subensembles, which leads to effective ergodicity breaking [64].

Let us emphasise here that this behaviour emerges as a result of manipulating quantum trajectories and, as such, is not reproducible classically. By way of illustration consider a classical analogue to the experimental setup shown in Fig. 5.1. For example, an optical cavity could have the output intensity monitored. Then, based upon the measured intensity, feedback could be applied. However, this would lead to a well-defined evolution of the dynamics that would not vary over multiple trajectories. As such, the above described generation of individual stochastic trajectories is a true quantum feature. Measurements depending on this quantum feature will be capable of showing non-classical correlations [19, 24]. It is this property that we exploit in this work to develop a quantum jump metrology scheme [13, 14]. To see how this quantum enhancement

manifests, we now more precisely consider the limits of estimation precision.

In the previous section, we formalised the process of a two-cavity network inside an instantaneous feedback loop. We now present the numerical simulation results of such a stochastic process. At first, we discuss the special case of the two-cavity network, then we can focus on the optical input parameters for optimum phase shift measurement and finally, we generalise the simulation scheme to test with more general parameters.

5.2.1.1 Special case $\varphi_1 = \varphi_2$

In this section, we present the optimal input signal for the optical network for achieving enhanced uncertainty measurement of the phase shift difference $\varphi = \varphi_1 - \varphi_2$. Initially, we examine a special scenario where φ_1 and φ_2 are both equal to $\pi/2$. We anticipate that the two cavities will be uncoupled. In other words, the input signal is exclusively emitted from a singular output port. In terms of photon statistics of the detectors, an initial cavity field is denoted as $\underline{\gamma}_i(0)$. As Fig. 5.3 demonstrates, the signal output from the second detector is zero, and it remains unchanged over time, whereas the signal from the first detector exhibits a rapid increase. This observation suggests that the two cavities have become decoupled. The proposed optical network scheme encompasses multiple variable parameters.

To optimise the accuracy of the obtained outcomes, it is essential to select the variable parameters carefully. Here, we examine the intensity of the feedback pulse denoted by $\beta_1^{(2)}$ and $\beta_2^{(1)}$ when paired with the initial cavity field $\underline{\gamma}_i(0)$. To examine these parameters, we will revisit the particular scenario where $\varphi_1 = \varphi_2$. Figure 5.4 illustrates the utilisation of two different sets of intensity feedback laser for the input laser beams, namely $\beta_1^{(2)} = \beta_2^{(1)}$ and $\beta_1^{(2)} = 2\beta_2^{(1)}$. By examining various input parameters, we present the outcomes obtained from utilising diverse feedback laser beams. The plot shown in Fig. 5.4 illustrates that when feedback pulses strengths $\beta_1^{(2)} = 2\beta_2^{(1)}$ and the initial state of cavities $\gamma_1(0) = \gamma_2(0) = 1$ are employed, it is evident from the observation that the feedback laser pulse set $\beta_1^{(2)} = 2\beta_2^{(1)}$ exhibits a slightly faster rate of divergence in the photon statistics

for the first detector in comparison to the scenario where the feedback pulses strengths are $\beta_1^{(2)} = \beta_2^{(1)}$. Therefore, we can anticipate that the sensing performance of the optical network will become attainable slightly faster in the case where $\beta_1^{(2)} = 2\beta_2^{(1)}$, than the case where $\beta_1^{(2)} = \beta_2^{(1)}$. However, no significant change is observed for the signal detected by the second detector.
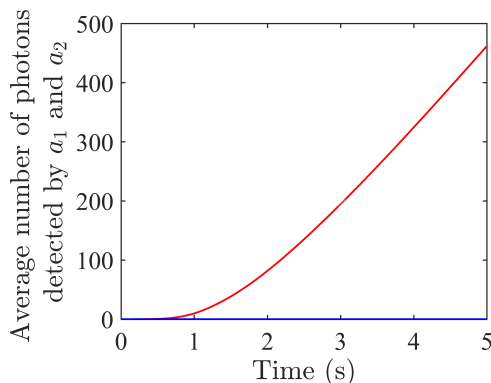
Figure 5.3: The average number of photons detected at detector 1 (red) and detector 2 (blue) as a function of time for feedback laser pulses $\beta_1^{(2)} = 2$ and $\beta_2^{(1)} = 1$ with $\gamma_1(0) = \gamma_2(0) = 1$, $\kappa_1 = \kappa_2 = \kappa$, $\Delta t = 10^{-3}\kappa^{-1}$, $\varphi_1 = \pi/2$, $\varphi_2 = \pi/2$ and $\varphi = \varphi_1 - \varphi_2 = 0$. We show here 500 trajectories for a total time of 5 s. We note that while the photon counts in the first detector 1 increase rapidly, no photons are detected at detector 2.

5.2.1.2 General case $\varphi_1 \neq \varphi_2$

Considering the general case where $\varphi_1 \neq \varphi_2$ with $\gamma_1(0) = \gamma_2(0) = 1$ and $\beta_1^{(2)} = 2\beta_2^{(1)}$, Fig. 5.5 reveals that the only time the second detector 2 will not detect any particles is when $\varphi_1 = \varphi_2$. Otherwise, once the phase shift difference is larger than zero, both detectors will detect photons simultaneously at different rates. In addition, detailed analysis about the behaviour of the estimator as a function of phase shift differences will be discussed in Section 5.3.2.

(a)   (b)
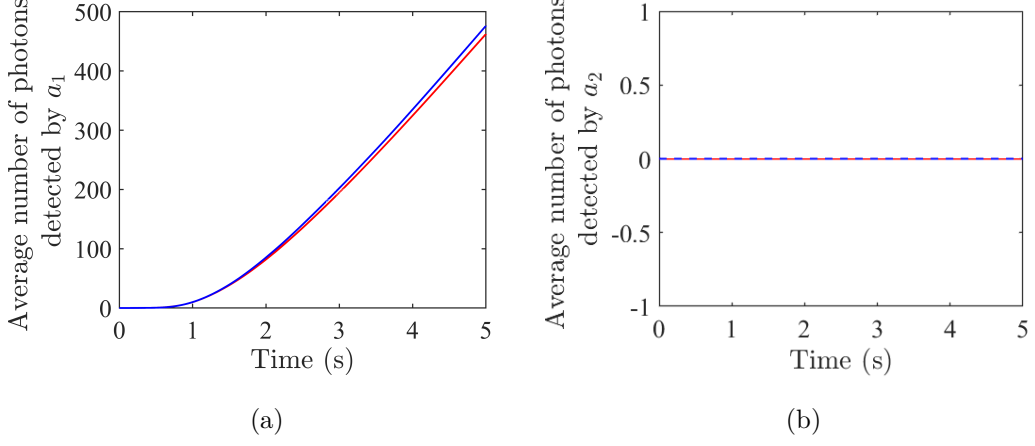
Figure 5.4:   The average number of photons detected at (a) detector 1 and (b) detector 2 as a function of time for feedback laser pulse $\beta_1^{(2)} = 1$, $\beta_2^{(1)} = 1$ (red) and $\beta_1^{(2)} = 2$, $\beta_2^{(1)} = 1$(blue). We present here the simulation of 500 trajectories with a total time of 5 s for $\gamma_1(0) = \gamma_2(0) = 1$, $\kappa_1 = \kappa_2 = \kappa$, $\Delta t = 10^{-3}\kappa^{-1}$ and $\varphi = 0$.

(a)   (b)
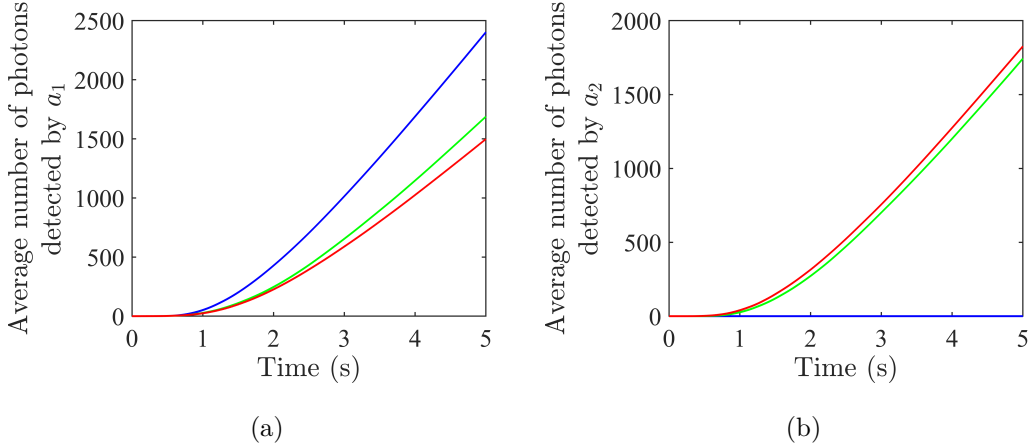
Figure 5.5:   The average number of photons detected at detector 1 and detector 2 as a function of time for different phase differences $(\varphi_1 - \varphi_2)$ for $\varphi = 0$ (blue), $\varphi = \pi/6 + \pi/10$ (green) and $\varphi = \pi/2 + \pi/10$ (red). We show here 500 trajectories for a total time of 5 s with $\gamma_1(0) = \gamma_2(0) = 1$, $\kappa_1 = \kappa_2 = \kappa$, $\Delta t = 10^{-3}\kappa^{-1}$, $\varphi_1 = \pi/2$ and $\varphi_2 = \pi/2$.

5.3   Basic quantum jump metrology

In this section, we present the fundamental protocol for phase shift estimation using the proposed two-cavity network subjected to an instantaneous quantum feedback loop. The simulation results of the dynamics of the two-cavity network are discussed, based on the mathematical framework established in earlier sections. We evaluate the performance and precision of parameter estimation by calculating the ensemble mean for multiple trajectories of the network dynamics evolved by the quantum jump method. Furthermore, the error propagation formula is used to quantify the scaling of the parameter estimation methodology. We examine the Fisher information associated with the photon statistics of the two optical cavity networks to further assess the presence of temporal correlation between the sequential measurements.

We focus on how quantum jumps may induce strong temporal correlations into the dynamics of the quantum trajectories of a single quantum system. These correlations can then be used to realise measurements with outcomes that manifest themselves in the properties of the trajectories rather than through ensemble averages. To see that such measurements are capable of enhanced performance, as pointed out previously in Refs. [13, 14], consider Eq. (5.15), which describes the time evolution of our system. Defining the Lindblad operators,

$$L_d = \sqrt{\kappa_d}\, D_2^{(a)}(\beta_2^{(d)}) D_1^{(a)}(\beta_1^{(d)}) a_d \tag{5.28}$$

for ease of writing, we can then write the master equation as

$$\dot{\rho} \;=\; \sum_{d=1,2} \left(L_d \rho L_d^\dagger - \frac{1}{2} \left[L_d^\dagger L_d, \rho \right]_+ \right). \tag{5.29}$$

To see these correlations, consider the Kraus decomposition of the dynamics, with Kraus operators

$$K_0 = U_{\text{cond}}(\Delta t, 0) \approx I - \sum_{d=1,2} \left(\frac{1}{2} L_d^\dagger L_d \right) \Delta t$$

$$K_1 \approx \sqrt{\Delta t}\, L_1$$

$$K_2 \approx \sqrt{\Delta t}\, L_2. \tag{5.30}$$

The coarse-grained time evolution of the system can thus be modelled by applying Kraus operator K_x after each observation $x = \{0, 1, 2\}$ at every time step Δt. The probability of observing a specific sequence of measurement outcomes is then

$$p(x_1, \ldots, x_N) = \text{Tr}\left[\left(\prod_{i=1}^{N} K_{x_{N+1-i}}\right) \rho \left(\prod_{i=1}^{N} K_{x_i}^\dagger\right)\right]. \tag{5.31}$$

Next, note that the Kraus operators do not commute due to the effect of the feedback. Thus, the events and measurements are not independent from one another. This can be seen more clearly by comparing the probabilities

$$p(x_N|x_{N-1}) = \frac{\text{Tr}\left[K_N K_{N-1} \mathcal{T}_1^{N-2}(\rho) K_{N-1}^\dagger K_N^\dagger\right]}{\text{Tr}\left[K_{N-1} \mathcal{T}_1^{N-2}(\rho) K_{N-1}^\dagger\right]} \tag{5.32}$$

and

$$p(x_N|x_{N-1}x_{N-2}) = \frac{\text{Tr}\left[K_N K_{N-1} K_{N-2} \mathcal{T}_1^{N-3}(\rho) K_{N-2}^\dagger K_{N-1}^\dagger K_N^\dagger\right]}{\text{Tr}\left[K_{N-1} K_{N-2} \mathcal{T}_1^{N-3}(\rho) K_{N-2}^\dagger K_{N-1}^\dagger\right]}. \tag{5.33}$$

Here, $p(x_N|x_{N-1})$ is the probability of measuring x_N after x_{N-1} in the previous time step, and $p(x_N|x_{N-1}x_{N-2})$ is the probability of measuring X_N after x_{N-1} and x_{N-2}, while the superoperator $\mathcal{T}_i^j$ describes a Markovian evolution from time-step i to j. In general, Eqs. (5.32) and (5.33) differ, meaning the measurement statistics do not form a Markov chain and thus possess non-trivial correlations [13, 14]. If the Kraus operators are dependent on the unknown parameter, these correlations may lead to a Fisher information growing faster than linearly, and thus, potentially resulting in an enhanced sensing precision. As we shall see below, in the case of the cavity network with quantum feedback that we consider here, this is indeed the case.

5.3.1 A simple measurement scheme for estimating phase difference

In this section, we finally discuss how the phase difference $\varphi = \varphi_1 - \varphi_2$ between two pathways of the network, as shown in Fig. 5.1, can be measured. We propose

a simple experimental scheme and analyse its performance by calculating the uncertainty $\Delta\hat{\varphi}$, based on an ensemble of simulated quantum trajectories. Throughout this analysis, we assume perfect photon detection; although, as mentioned already earlier, losses are not expected to significantly harm the performance of the scheme [14].

5.3.2 The basic protocol

As Fig. 5.2 demonstrates, in the presence of quantum feedback, the cavity network in Fig. 5.1 generates two classes of trajectory. One class of trajectories prepares both cavities rapidly in their respective vacuum states, while the other class quickly results in huge photon number populations in both resonators. Our simulations show that the relative size of the subensemble associated with each class has a relatively strong dependence on the phase difference φ that we want to estimate. The probability that the total number of photons being emitted within a certain time interval of length t is above a certain threshold therefore acts as a reliable measurement signal for the type of trajectory being observed. The threshold is introduced since we can notice that the signal becomes saturated quickly as the signal diverges exponentially after some time T. Rather than relying on the average of the total number detected, we introduce a threshold to the signal to prevent it from diverging exponentially.

As we shall see below, it is important to choose the experimental parameters and the photon number threshold carefully in order to ensure that useful information is revealed. For example, if the threshold number of photons is too low, it will not faithfully distinguish between the trajectory classes. Moreover, attention needs to be paid to the strength of the feedback and the choice of the initial state. Finding a balance between these parameters is essential when determining the phase difference φ as precisely as possible.

An analytic calculation of the expected measurement signal is not straightforward due to the non-linear dynamics of the cavity network and its lack of a stationary state [64]. Hence, to determine the uncertainty of the above-introduced estimator of φ for the chosen measurement signal, we numerically simulate and

sample a large number of trajectories over a coarse-grained timescale. This then allows us to estimate the probability of the system emitting a number of photons surpassing the threshold we set, to estimate φ as a function of the time t. Here, we are especially interested in the uncertainty $\Delta\hat{\varphi}(t)$ of this signal.

In the following, we consider a specific, carefully chosen set of parameters to demonstrate the possible quantum advantage of our measurement scheme. As with the threshold value, it is important to choose feedback parameters that are both not too small and not too big. For example, for very weak feedback, we are unlikely to deduce information about φ over reasonable timescales. Moreover, for very strong feedback, the dynamics of the cavity network become dominated by the feedback; almost all trajectories diverge and the measurement outcomes are essentially independent of the unknown phase that we want to identify. Finally, in order to avoid starting in the vacuum state and for the practicality of implementation, we start each trajectory with the same initial state to prepare a non-trivial initial state. Following some experimentation with different sets of variables, a set of parameters is selected eventually to execute the simulations below of the parameter estimation of the phase shift difference of the two-cavity network.

With all of these factors in mind, Figs. 5.6–5.8, show two different measurement signals, i.e. the probability $(P_{N>N_{threshold}})_{d_i}$ of detecting more than $N = N_{threshold}$ photons within a time interval $(0, t)$ at the first detector 1 and the second detector 2, respectively, for three different values of total time t and three values of thresholds $N_{threshold}$. As expected, this probability increases as t increases. Moreover, it depends on the phase shift difference φ. Considering Figs. 5.6–5.8, we see that the optimal phase to conduct an estimation at is around $\varphi = 0$ due to the sharpness of the gradient of the measurement signal at this point. This corresponds to a crucial point in the dynamics. When $\varphi = 0$, only one detector mode is ever occupied. However, moving away from this point, the other detector mode begins to be occupied too. Thus, taking advantage of this distinction in the signal allows for the best measurement. Due to numerical instabilities, evaluating $(P_{N>N_{threshold}})_{d_i}$ exactly at this point is, however, difficult. Therefore, we take our
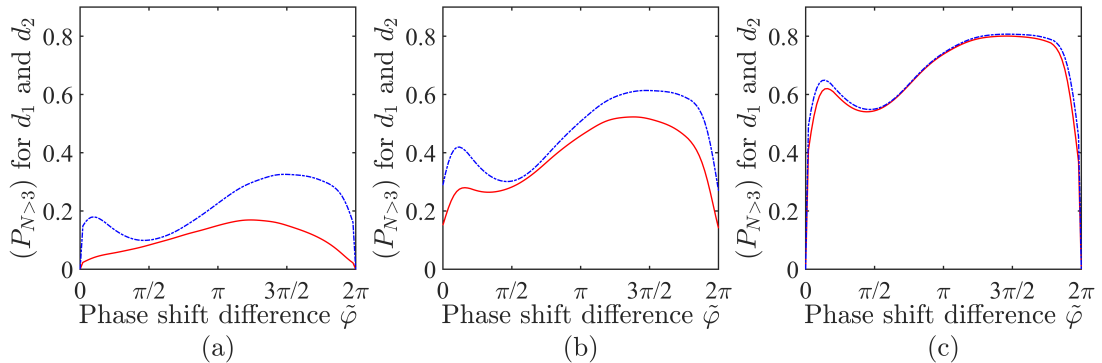
Figure 5.6: The probability $(P_{N>3})_{d_i}$ with $i = 1$ (red-solid) and $i = 2$ (blue-dot-dashed), respectively, of surpassing the threshold number of $N = 3$ photon emissions within a certain time interval $(0, t)$ as a function of the phase shift difference φ. Here, (a) $t = 0.7\,\kappa^{-1}$, (b) $t = 1.5\,\kappa^{-1}$ and (c) $t = 5\,\kappa^{-1}$. We average over 10^4 trajectories with $\Delta t = 10^{-3}\kappa^{-1}$, $\gamma_1(0) = \gamma_2(0) = 1$ and apply quantum feedback as described in Eq. (5.27) with $\varphi_1 = \pi/2$, $\varphi_2 = \pi/2 + \pi/10$, $\beta_1^{(2)} = 2$ and $\beta_2^{(1)} = 1$.

data at a nearby value of $\varphi = \pi/10$ where the gradient is still high for reasonable amounts of time.

5.3.3 Fisher information for the photon statistics of an optical cavity network

Before further analysing the performance of the proposed quantum optical sensor, we now calculate the Fisher information of the photon statistics, using the methods outlined in Section 2.4. This way, we obtain a bound on the optimum precision that our measurement scheme can achieve. The probability of a certain trajectory with a given number of time steps can be calculated using Eq. (5.31). To do so, it has to be taken into account that every individual time step has one of four different possible event types, quantified by the probabilities P_{ij} introduced in Section 5.1: no-photon, photon only in detector 1, photon only in detector 2 or photons in both detectors. A drawback of this, however, is
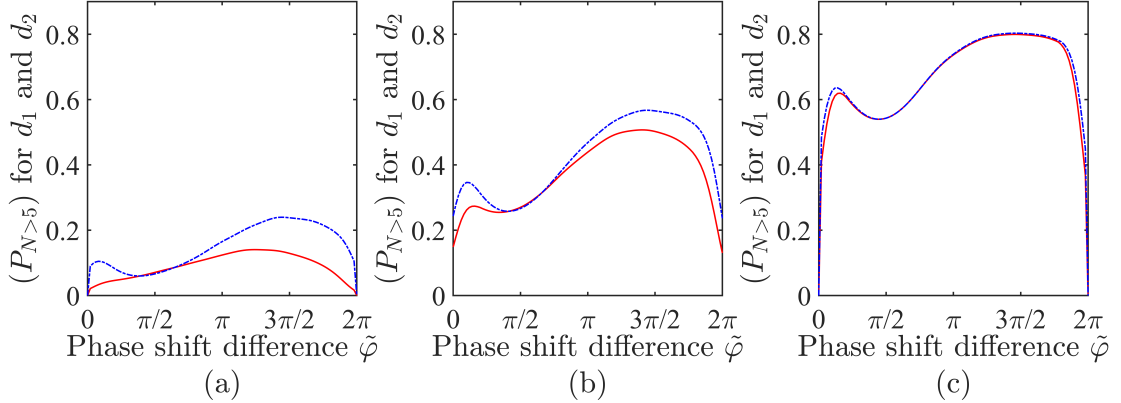
Figure 5.7: The probability $(P_{N>5})_{d_i}$ with $i = 1$ (red-solid) and $i = 2$ (blue-dot-dashed), respectively, of surpassing the threshold number of $N = 5$ photon emissions within a certain time interval $(0, t)$ as a function of the phase shift difference φ. Here, (a) $t = 0.7\,\kappa^{-1}$, (b) $t = 1.5\,\kappa^{-1}$ and (c) $t = 5\,\kappa^{-1}$. We average over 10^4 trajectories with $\Delta t = 10^{-3}\kappa^{-1}$, $\gamma_1(0) = \gamma_2(0) = 1$ and apply quantum feedback as described in Eq. (5.27) with $\varphi_1 = \pi/2$, $\varphi_2 = \pi/2 + \pi/10$, $\beta_1^{(2)} = 2$ and $\beta_2^{(1)} = 1$.

that an exact calculation of the Fisher information for a trajectory of length N requires summing over 4^N possible trajectories. Hence, this approach becomes computationally very challenging for large N. Nevertheless, for small N, we find scaling beyond linear of the form

$$F(N) \quad \propto \quad O(N^2) - O(N)\,, \tag{5.34}$$

as can be inferred from the behaviour of the Fisher information curve in in Fig. 5.9.

The limitation of only having exact results for the Fisher information for a small number of time steps means we do not have a strict bound for the system for larger times. Instead, we extrapolate the scaling shown for short times as in Fig. 5.9. Nevertheless, we expect that this approach provides an upper bound on the Fisher information, as it is likely that at large times the scaling will reduce rather than increase due to a breakdown in correlations between faraway time steps. This observation suggests that the estimated bound can nevertheless be
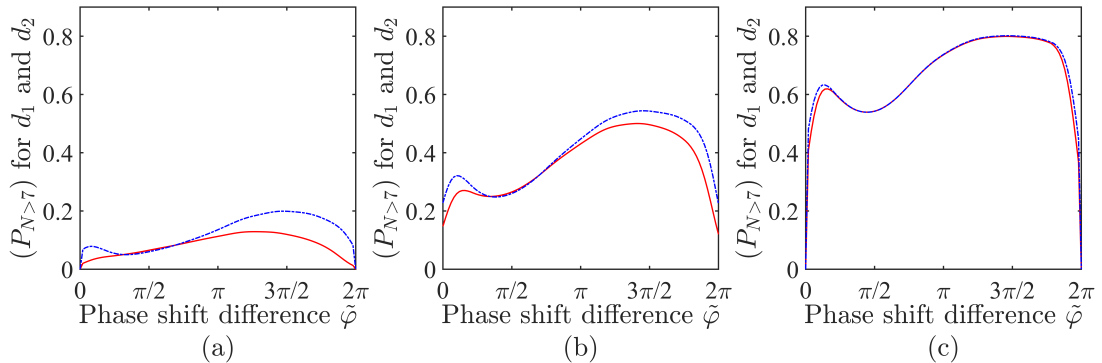
Figure 5.8: The probability $(P_{N>7})_{d_i}$ with $i = 1$ (red-solid) and $i = 2$ (blue-dot-dashed), respectively, of surpassing the threshold number of $N = 7$ photon emissions within a certain time interval $(0, t)$ as a function of the phase shift difference φ. Here, (a) $t = 0.7\,\kappa^{-1}$, (b) $t = 1.5\,\kappa^{-1}$ and (c) $t = 5\,\kappa^{-1}$. We average over 10^4 trajectories with $\Delta t = 10^{-3}\kappa^{-1}$, $\gamma_1(0) = \gamma_2(0) = 1$ and apply quantum feedback as described in Eq. (5.27) with $\varphi_1 = \pi/2$, $\varphi_2 = \pi/2 + \pi/10$, $\beta_1^{(2)} = 2$ and $\beta_2^{(1)} = 1$.

useful when compared to the uncertainty of our proposed measurement scheme. We note that general methods of obtaining more accurate estimations of the Fisher information in Eq. (5.34) would require being able to obtain solutions to the master equation of the cavity network and to determine the stationary state of its dynamics [127], neither of which are present within our system.

5.4   Sensing performance

In this section, we provide a thorough investigation of the scaling phenomenon in the phase shift measurement estimation technique. Since the dynamics of the system are highly non-linear, the scaling of the phase shift measurement of the two-cavity network is estimated numerically. We consider the relative number of trajectories with multiple successive emissions which generate an above-threshold photon count in a given time interval as a measurement observable. We determine
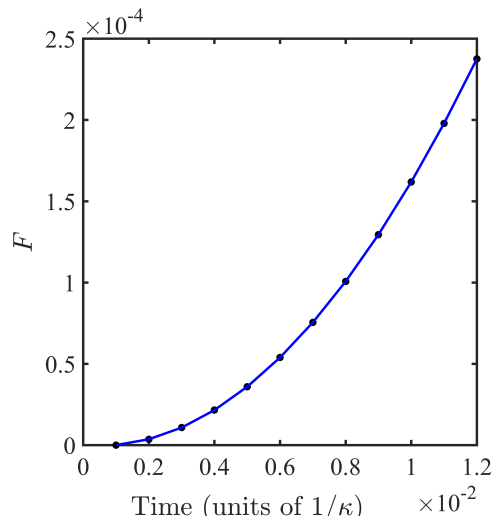
Figure 5.9: The Fisher information of the two-cavity network for $\varphi = \pi/10$, where $\varphi_1 = \pi/2$ and $\varphi_2 = \pi/2$, as a function of time. The Fisher information is obtained exactly for $N = 12$ time steps $\Delta t = 10^{-3}\kappa^{-1}$, and the subsequent fit is extended for all time.

the estimation uncertainty $\Delta\hat{\varphi}$ in the following with the help of the standard error propagation formula

$$(\Delta\hat{\varphi})^2 \quad = \quad \frac{\left(\Delta\hat{O}\right)^2}{\left|\frac{\partial\langle\hat{O}\rangle}{\partial\varphi}\right|^2}, \tag{5.35}$$

where $\hat{O}$ denotes the relevant observable. The variance in the numerator of this equation is obtained by sampling over 10 subensembles with 10^4 trajectories in each subensemble, while the visibility in the denominator is obtained numerically. Utilising this technique, we can study how the error in estimating the phase difference behaves for the sensing protocol that we propose here. Here, we consider a specific set of parameters to demonstrate the utility of our system for estimating a phase in an optical cavity network. It is important to choose feedback parameters that are both not too small, such that the induced effects are observable over reasonable timescales, and also not too large, such that the dynamics are completely dominated by the feedback and thus, almost independent of the

initial conditions and, crucially, the unknown phase of the system. Similarly, the photon emission threshold of our signal should also be appropriately sized such that good results can be obtained on relatively short timescales but not so short that distinguishability between different phases is small.

5.4.1 Variable threshold

The uncertainty of the phase shift measurements $\Delta\hat{\varphi}$ for the selected measurement signal is evaluated numerically using Eq. (5.35) for a set of chosen parameters. As mentioned earlier, the uncertainty in the phase shift difference measurement $\Delta\hat{\varphi}$, for the phase shifts $\varphi_1 = \pi/2$ and $\varphi_2 = \pi/2 + \pi/10$, is evaluated numerically by sampling over 10 subensembles each of 10^4 trajectories. The numerator of Eq. (5.35) is evaluated by looking at the variance of 10 subensembles, while the denominator that is known as the visibility or sensitivity of the signal is calculated numerically by evaluating the gradient in the signal as a function of the phase shift difference. More specifically we look at the change in signal $\partial\varphi$ at $\varphi_1 = \pi/2$ and $\varphi_2 = (\pi/2 + \pi/10) \pm \pi/10$. Fig. 5.10 (a) shows the uncertainty $\Delta\hat{\varphi}$ for detector 1 mode with different threshold photon numbers $N_{threshold} = 3$, $N_{threshold} = 5$ and $N_{threshold} = 7$. In detector 1 mode, we see that for the chosen threshold photon numbers, the exact value of the threshold only has a small effect on the obtained results; even with a small number of emissions, the total number of photons in the system is likely to diverge. We also plot the extrapolated bound obtained from the Fisher information for comparison. We see that at early times, we get close to the estimated measurement uncertainty $\Delta\hat{\varphi}$ for detector 1 which then plateaus at later times. An analogous pattern of behaviour can be observed in Fig. 5.10 (b), which shows the uncertainty associated with the measurement of phase shift when using the photon statistics obtained from detector 2. Furthermore, it is worth noting that during the initial stages, we observe slight variations in the scaling behaviour across different threshold values. However, as time progresses, the scaling curves begins to overlap for extended periods of time, even across different threshold values. For both detectors and all three thresholds, we are able to get close to the projected bound, thus suggesting that the proposed

bound is feasible and our estimation strategy is effective. For the specific values chosen here, the initial performance of detector 2 is worse, but $\Delta\hat{\varphi}$ of detector 2 steadily decreases and eventually beats that of detector 1, before plateauing much later. Furthermore, the simulations error analysis is carried out by evaluating the variance of the uncertainty in phase shift estimation across multiple subensembles produced by the simulation. As displayed in Fig. 5.10, the error in the stochastic simulation, which is represented as a shaded area surrounding the curves, starts off large before decreasing through time. This behaviour is quite expected, as the fluctuations in the signal are fairly strong at the beginning, but they progressively decrease as the effect of the quantum feedback on the system becomes more prominent.

(a)   (b)
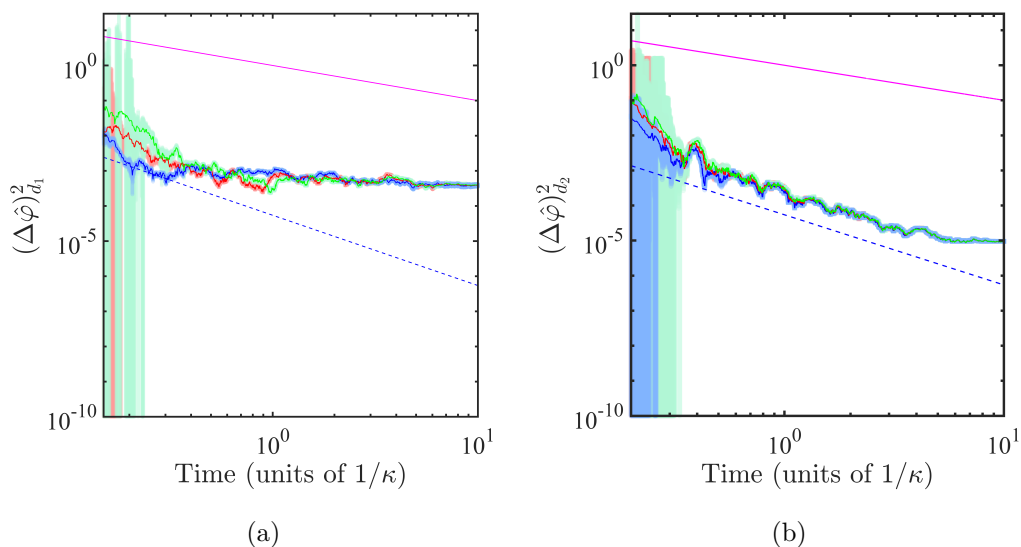
Figure 5.10:   The uncertainty in the phase shift measurement for phase differences $\varphi = \pi/10$, where $\varphi_1 = \pi/2$ and $\varphi_2 = \pi/2$, as a function of time for (a) detectors 1 and (b) detector 2 and for three different thresholds, $N = 3$ (blue-solid), $N = 5$ (red-solid) and $N = 7$ (green-solid). The blue dashed line shows the extrapolated value of the reciprocal of the Fisher information, providing an estimated lower bound on the potential sensitivity of the data, and the magenta solid line shows the scaling of the SQL .

5.4.2 Variable phase

Next, we have a closer look at the performance of the proposed sensing scheme for different values of φ. Figure. 5.11 (a) shows $\Delta\hat{\varphi}$ for detector 1 as a function of time. As expected, we find that the sensor performs best when φ is close to 0. This result is confirmed when looking at the bounds for different values of φ, which also suggests that the distinguishability of the photon statistics is sharpest around $\varphi = 0$, although the differences for the different phases are relatively small. A similar behaviour is observed in Fig. 5.11 (b), where we see that at $\varphi = \pi/10$, the scaling performs better for detector 2 for a relativity longer time. For completeness, we note that we have already seen in Figs. 5.6– 5.8, that the gradient of the signal is generally the sharpest at this point. The sharp gradient of the estimator indicates the high sensitivity of the signal to the change in the phase shift difference. We find that the sensor performance can approach the projected bound for large parts of the evolution when evaluating at $\varphi = \pi/10$ with a threshold of $N = 3$, as seen in Fig. 5.11, for the parameters chosen here. This is a promising result, as it justifies the projection of the bound by following the same trend, even if the exact values do not match. It is also likely that the signal we use as an estimator here is not optimal, and as such, we would not expect it to fully saturate the bound. Moreover, the parameter choices are not necessarily optimised, meaning other regimes may yield stronger results. As mentioned earlier, the error in the simulations is displayed as a shaded surrounding the curves. Similar to the Fig. 5.10, the error is large at the start of the stimulations but declines rapidly at time increases. Nevertheless, the scaling of our signal is promising and therefore a strong result for demonstrating the quantum enhancement of the quantum jump metrology scheme that we analyse here.

(a)

(b)

(c)
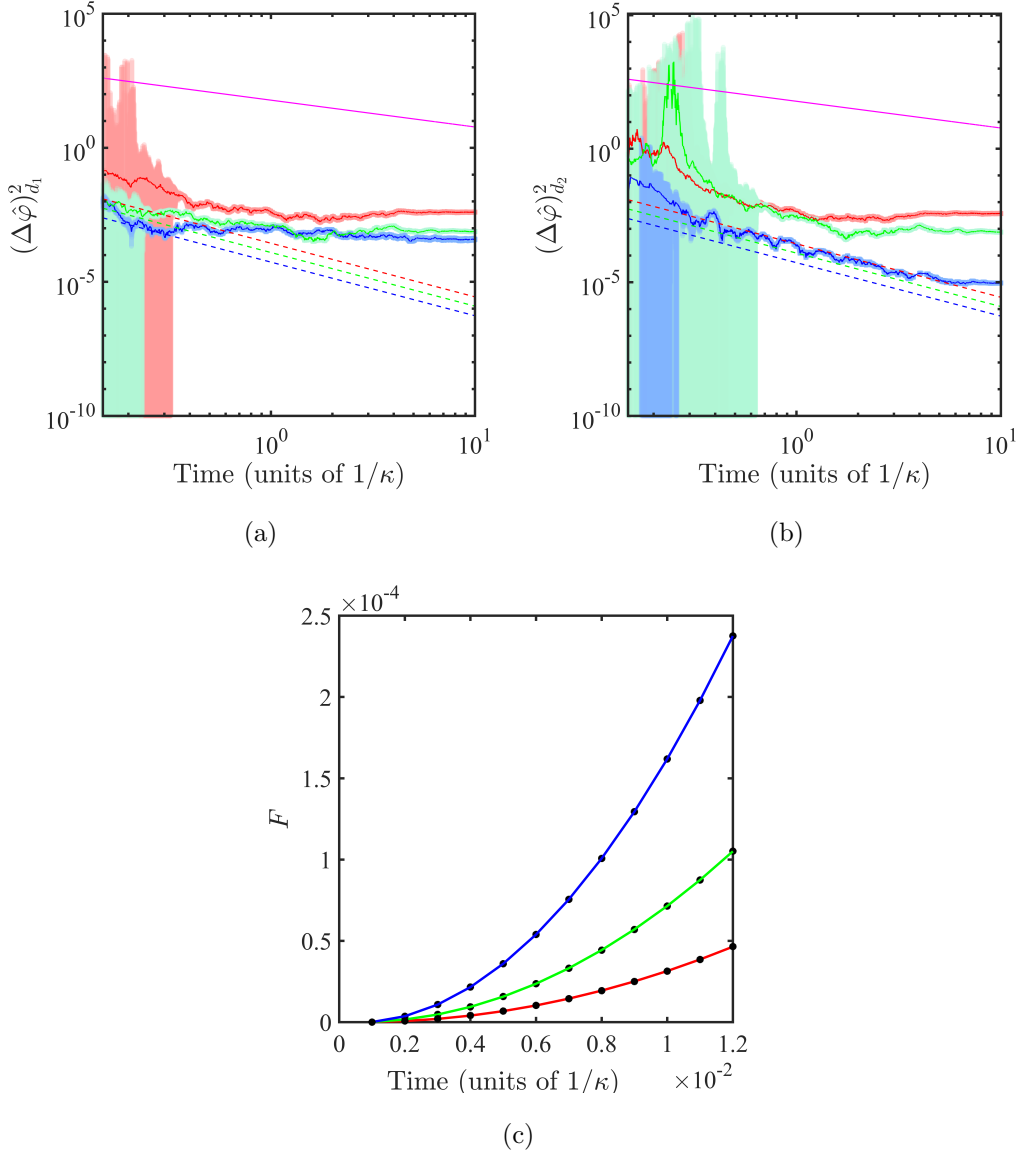
Figure 5.11: The uncertainty in the phase shift measurement for phase differences $\varphi = \pi/10$, where $\varphi_1 = \pi/2$ and $\varphi_2 = \pi/2$, for (a) detectors 1 and (b) detector 2 as a function of time. Here, the threshold number is fixed to $N = 3$, and we consider $\varphi = \pi/10$ (blue-solid), $\varphi = \pi/10 + \pi/2$ (red-solid) and $\varphi = \pi/10 + 3\pi/4$ (green-solid), with all other parameters and generation data as before. Now, we also have different bounds for the different phase estimations (shown as dashed lines for the respective line colours). In (c) we show the exact Fisher information for each phase, with the extrapolation of it shown in the bounds in (a) and (b) as the dashed lines. We again shown the SQL scaling for illustrative purposes with the magenta line.

91

5.5 Summary

In the previous section, a comprehensive examination was conducted on the two-cavity network inside an instantaneous feedback loop. In the theoretical modelling of the optical network, we have taken into account the utilisation of two optical cavities that are in a coherent state. To enable photon detection, the cavities are permitted to leak in one direction. In addition, when a photon is detected at either of the two detectors, it triggers a laser pulse. The optical cavities are subject to the influence of the feedback driving laser, which causes a displacement in the state of the cavity. The examination of the evolution of the cavity field is represented by the master equation of Lindblad form. Furthermore, the process of evolution is defined by the event of photon emission and the absence of photon detection at the detectors. Since, solving the master equation analytically poses a significant challenge, therefore, a numerical approach has been chosen. The fundamental principles of the optical network were established within the framework of quantum jump meteorology.

A preliminary examination was conducted on the photon statistics behaviour of the optical network to identify the most suitable parameters for assessing the network's scaling in parameter estimation for phase shift measurement. The determination of the optical network scaling was based on a selected observable. Specifically, the probability of detecting a certain threshold number of photons was selected as an observable and the accuracy of the phase shift measurements as a function of time was estimated using the error propagation formula. The network's performance was evaluated through the assessment of the Fisher information and the introduction of error bars in the plotted signal. In general, the overall dynamics of the two-cavity network have been simulated utilising various input parameters that determine the evolution of the system. The simulations have demonstrated non-linear dynamics that exhibit a significant dependence on the phase shift difference between the two arms of the optical network. The scaling of the phase shift measurement was found to exceed the SQL, demonstrating quantum enhancements of the quantum jump metrology scheme as a result of the presence of the temporal correlations.

Chapter 6

Quantum advantage without entanglement

The development of mathematical frameworks designed to study the time evolution of quantum systems has been studied extensively. In general, the interaction between the surrounding environment and the quantum systems is unavoidable. Therefore, the development of tools to simulate open quantum systems has been a focal point due to their importance in understanding many physical phenomena [128]. Nevertheless, modelling the evolution of quantum systems is known to be quite a challenging task. While it is theoretically feasible to model quantum systems with classical models, the latter rapidly became exceedingly complex. As an illustration, it is essential that the classical models violate fundamental principles of physics, such as locality. However, instead of examining entangled composite quantum systems to demonstrate the need for quantum physics, we may investigate whether we can model a single quantum system equally well with a classical stochastic model. In general, classical stochastic models can be used to model how a quantum system evolves unitarily while no measurements are performed, or even when a single measurement is performed at the end of the dynamics. However, quantum systems that experience sequential measurements can produce highly correlated measurement outcomes [129]. In general, these measurement outcomes cannot be produced by complex classical machines. Instead

of examining entanglement (i.e. nonclassical local correlations), we identify the following non-classical correlations in time. These have also been referred to as entanglement in time [130–133]. Recently, it has been understood that quantum systems can generate not only local but also temporal non-classical correlations, and the search for the best quantum machines that exploit these correlations is currently underway.

Furthermore, recent studies have demonstrated that the temporal correlations exhibited by quantum systems surpass those of classical systems [134]. The quantum description of finite state generator machines has been thoroughly investigated in many articles. They show the advantage of adopting the quantum approach for simulating stochastic processes [20]. In addition, utilising the quantum properties also aid in reducing the complexity of the mathematical models needed to simulate a certain stochastic process [135–137]. Quantum advantages of quantum devices extend to the reduction of the complexity and memory needed to simulate stochastic processes [135, 138, 139].

Consequently, the existence of such robust correlations motivated researchers to investigate a quantum version of the HMM. The HQMM appears to be able to model stochastic processes with fewer resources while maintaining longer temporal correlations [19, 22, 24]. In such a model, the system is allowed to interact with the environment, and a projective measurement is performed on the combined system. This kind of system is considered to be an analogue to an open quantum system where the composite state of the principle system and the environment is a mixed state and has to be represented by a density matrix [24]. Other mathematical versions of the quantum description of the HMM have appeared in literature, introducing a new method of simulating quantum systems [21, 22, 140, 141]

Furthermore, the open quantum system used in the quantum jump metrology scheme can be understood to be an example of a HQMM [24]. Hence, to gain a better understanding of the quantum advantage experienced in the quantum jump metrology scheme of two-cavity optical network scheme presented in Section 5, we investigate the temporal correlations that exists in HQMMs. Therefore, in this

chapter, we fully characterise and review the main properties of such a quantum machine, namely a one-qubit HQMM. In this chapter, we systematically examines quantum correlations in HQMMs and compares them to classical models such as HMMs and MMs.

This chapter contains four sections. In Section 6.1, we present an overview of the definitions and characterisation of the MM, HMM and HQMM. In Section 6.2, we give a full parametrisation of the MM, HMM and HQMM. After presenting all the necessary theoretical characterisation of the three models, we show a numerical comparison of the complexity of the models in Section 6.3. Finally, we summarise our findings in Section 6.4.

6.1 Hidden quantum Markov models and their classical counterparts

The MMs which are also known as Markov models, are memoryless generators of stochastic processes. One way of simulating more complex stochastic processes is to replace these machines with HMMs with an internal memory. Alternatively, more complex stochastic sequences can be generated without adding memory by taking advantage of quantum physics. The resulting quantum machines, which are generalisations of earlier, less powerful quantum processors [20], have been named HQMMs [19]. In this section, we examine the definitions of all three machines. As already mentioned above, here, we are only interested in machines with two possible outputs, *A* and *B*.

6.1.1 Markov models

First, we examine the definition of discrete-time MMs. These evolve on a coarse-grained time scale and their dynamics are dominated by the generation of random output signals and random transitions from one state i to another state j in a fixed time interval Δt [80]. The output signals and the dynamics of MMs depend solely on the current state of the machine, which is known as the *Markov*

Figure 6.1: A schematic view of a Markov model with two states 1 and 2. Here $t_{j|i}$ denotes the probability of the machine to transition from state i into state j. During each transition, an output symbol is created. All red arrows are accompanied by the generation of an output A, while the blue arrows correspond to transitions that generate an output B. In this way, the obtained output symbol is a clear indication of the state of the machine. Therefore, state of the machine is not hidden.

property. Therefore, state of the machine is not hidden. Discrete MMs are fully characterised by 3-tuples $(\mathcal{S}, \mathcal{T}, \boldsymbol{p}(0))$, where $\mathcal{S}$ describes the available state space, $\mathcal{T}$ specifies all possible transition probabilities between the states of the machine, and $\boldsymbol{p}(0)$ presents the initial state populations [142].

Since we only consider stochastic machines with two possible outputs A and B, in every time step, our MMs switch randomly into one of only two possible states. In the following, we denote them by 1 and 2 and $\mathcal{S} = \{1, 2\}$. As illustrated in Fig. 6.1, preparing the machine in 1 or in 2 generates an output A or B, respectively. Suppose $S(n) = i$ is the state of an individual machine after n time steps. Then

$$S(n+1) = j, \tag{6.1}$$

with transition probability $t_{j|i}$.

However, if all measurement outcomes are ignored, or if ensemble averages for a large number of MMs are considered, the states $S(n)$ of individual MMs are generally unknown. In this case, we describe the state of a machine by a

two-dimensional vector $\boldsymbol{p}(n)$ of the form

$$\boldsymbol{p}(n) = \begin{pmatrix} p_1(n) \\ p_2(n) \end{pmatrix} , \tag{6.2}$$

where $p_i(n)$ is the probability of finding the machine after n time steps in state i. The probabilities $p_1(n)$ and $p_2(n)$ are both positive and always add up to one,

$$p_1(n) + p_2(n) = 1 . \tag{6.3}$$

The state vector $\boldsymbol{p}(n)$ can be used to calculate the probability of finding the MM in the $n+1$ th measurement in one of its two states. As mentioned already above, $\boldsymbol{p}(0)$ is the initial state of the MM.

Notice also that the dynamics of the state vectors $\boldsymbol{p}(n)$ can be described by a single transition matrix $T \in \mathcal{T}$. More concretely, it is defined such that

$$\boldsymbol{p}(n+1) = T \, \boldsymbol{p}(n) . \tag{6.4}$$

The operator T contains all the probabilities $t_{j|i}$ that govern the dynamics of the MM while generating a stochastic sequence of A's and B's. For example, for the two-state Markov chain in Fig. 6.1, we have

$$T = \begin{pmatrix} t_{1|1} & t_{1|2} \\ t_{2|1} & t_{2|2} \end{pmatrix} . \tag{6.5}$$

However, as we will show in Section 6.3, the relative simplicity of MMs has the drawback of resulting in relatively weak measurement correlations.

6.1.2   Hidden Markov models

As illustrated in Fig. 6.2, like MMs, HMMs are generators of stochastic processes that obey the Markov property and whose output symbols only depend on the current state of the machine. However, like their name suggests, HMMs have a hidden state space, and their outputs are no longer an indication of their current state. The internal states of these machines remain *hidden*. Hence HMMs are characterised not by 3-tuples but by 5-tuples $(\mathcal{S}, \mathcal{T}, \mathcal{O}, \mathcal{B}, \boldsymbol{p}(0))$. As in the case
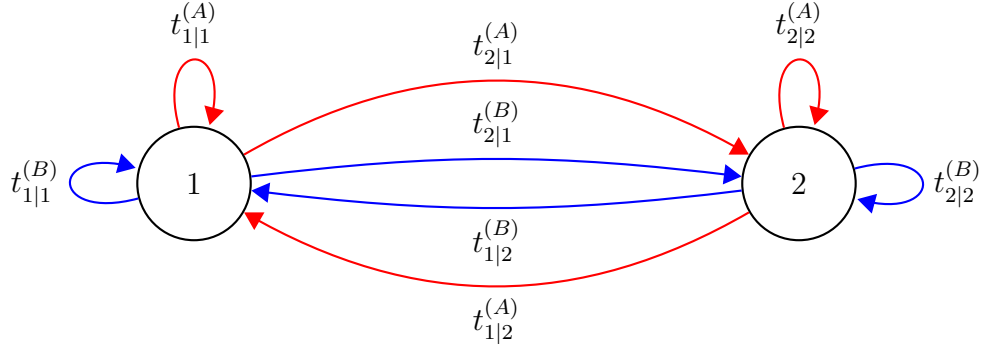
Figure 6.2: A schematic view of a hidden Markov model with two states 1 and 2. Here $t_{j|i}^{(m)}$ denotes the probability of the machine to transition from state i into state j while generating an output m. During each transition, an output symbol is created. All red arrows are accompanied by the generation of an output $m = A$, while the blue arrows correspond to transitions that generate an output $m = B$.

of MMs, $\mathcal{S}$ determines the states space of the machine, $\mathcal{T}$ represents the transition probabilities and $\boldsymbol{p}(0)$ describes the initial state populations. Moreover, $\mathcal{O}$ specifies the possible measurement outcomes, and $\mathcal{B}$ contains the probabilities for generating these outcomes [87].

Next, we notice that there are two different types of HMMs known as Moore and Mealy [143]. In the first type, the generated stochastic output depends only on the current state of the machine. In the latter type, it depends on the current state and on the observed output symbol, as illustrated in Fig. 6.2. We focus on Mealy HMMs, which contain Moore HMMs as a subset. In general, we are interested in comparing quantum machines to the most general possible classical stochastic generators.

As mentioned already in the previous subsection, here, we are especially interested in machines with only two possible outputs, namely A and B. However, in the case of HMMs, this does not restrict the number of internal states N. In the following, we denote the hidden states of the HMM by i, with i varying from 1 to N. Suppose $t_{j|i}^{(m)}$ is the probability for a HMM prepared in state i to transition into j while generating output m. In this case, given $S(n) = i$, we again find that

$S(n+1) = j$, as in Eq. (6.1). The probability of obtaining this state now equals the sum of the probabilities of generating an A and a B,

$$t_{j|i} = t_{j|i}^{(A)} + t_{j|i}^{(B)} \,. \tag{6.6}$$

Furthermore, for an external observer with access only to the outputs of the machine but no access to its hidden states, the state of the machine can only be estimated. If we introduce two sub-transition matrices T_m where $m = A, B$ such that

$$T_m = \begin{pmatrix} t_{1|1}^{(m)} & t_{1|2}^{(m)} & \cdots & t_{1|N}^{(m)} \\ t_{2|1}^{(m)} & t_{2|2}^{(m)} & \cdots & t_{2|N}^{(m)} \\ \vdots & \vdots & & \vdots \\ t_{N|1}^{(m)} & t_{N|2}^{(m)} & \cdots & t_{N|N}^{(m)} \end{pmatrix}, \tag{6.7}$$

then the state of the HMM conditional on obtaining the output m can again be described by a vector $\boldsymbol{p}(n)$ with coordinates $p_i(n)$. These now denote the probability of finding the HMM after n time steps in a certain state i, if the state of the machine were to be observed. Using the above notation and for a given state vector $\boldsymbol{p}(n)$, the state $\boldsymbol{p}(n+1)$ of the HMM conditional on output m equals

$$\boldsymbol{p}(n+1) \;=\; T_m \, \boldsymbol{p}(n)/\mathrm{Pr}_n(m) \,. \tag{6.8}$$

Here, $\mathrm{Pr}_n(m)$ denotes the probability of obtaining the output m in step n. The state vectors $\boldsymbol{p}(n)$ are now real vectors of dimension N, with coordinates $p_i(n)$, which must add up to one.

In addition, we can calculate the probability of a HMM being in a certain state i after n steps, even when all its measurement outputs are ignored. As in the previous subsection, the dynamics of the state vectors of the HMM can be described by a transition matrix T in this case,

$$T \;=\; T_A + T_B \,, \tag{6.9}$$

which is the sum of the two subtransition matrices T_A and T_B and

$$\boldsymbol{p}(n+1) \;=\; T \, \boldsymbol{p}(n) \,, \tag{6.10}$$

in analogy to Eq. (6.1). The matrix elements of the total transition matrix T are the $t_{j|i}$ in Eq. (6.6). If $\eta = (1, 1, \ldots, 1)$ is a row vector with all N coordinates equal to 1, then the probability $\Pr_{n+1}(m)$ of getting output m after $n + 1$ steps equals

$$\Pr_{n+1}(m) \;\; = \;\; \eta\, T_m\, \boldsymbol{p}(n)\,. \tag{6.11}$$

For a Moore HMM, the transition probabilities $t_{j|i}^{(m)}$ are the product of a function that depends only on i and j and a function that depends only on m. In general, no such restrictions apply.

6.1.3   Hidden quantum Markov models

To obtain a quantum version of HMMs, all we need to do is to replace its hidden state $S(n)$ by quantum state $|\psi(n)\rangle$. The possible transitions between the internal states of the system are again specified by linear stochastic process transition matrices [19]. For Markov processes, these transition matrices are the same for every time step and do not depend on the history of the quantum version of HMMs. As a result, the output of the machine and the transition that occurs depend only on the current internal state of the HQMM. Hence, the internal quantum states $|\psi(n)\rangle$ evolve by experiencing generalised quantum operators, so-called Kraus operators K_m, as shown in Fig. 6.3. These operators are routinely used, for example, to describe general quantum measurements in quantum information processing [98, 144–146].

Here, we are especially interested in one-qubit HQMMs with a two-dimensional internal state space where this machine has one-qubit memory. This means that the hidden state of the machine after n time steps is a two-dimensional quantum state $|\psi(n)\rangle$ of the general form

$$|\psi(n)\rangle \;\; = \;\; \alpha(n)|1\rangle + \beta(n)|2\rangle\,, \tag{6.12}$$

where $|1\rangle$ and $|2\rangle$ are two orthogonal quantum states that the machine can assume, and $\alpha(n)$ and $\beta(n)$ are complex coefficients with

$$|\alpha(n)|^2 + |\beta(n)|^2 \;\; = \;\; 1\,. \tag{6.13}$$
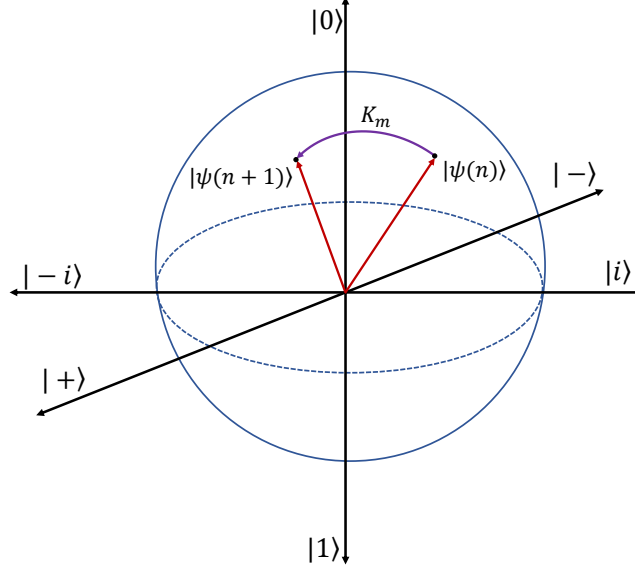
Figure 6.3: Hidden quantum Markov model evolution in a Bloch sphere representation. The evolution of the wavefunction $|\psi(n)\rangle$ is represented by the three-dimensional vector in the Bloch sphere. The evolution of the wavefunction $|\psi(n)\rangle$ is governed by the Kraus operators K_m that evolve the state $|\psi(n)\rangle$ to $|\psi(n+1)\rangle$ at each time step while generating an output m.

Hence, a HQMM not only has two internal states but also stores its information in a continuum of state vectors, which are characterised by the complex coefficients $\alpha(n)$ and $\beta(n)$. Within each time step, the state of the HQMM changes such that

$$|\psi(n+1)\rangle = \frac{K_m |\psi(n)\rangle}{\|K_m |\psi(n)\rangle\|}, \tag{6.14}$$

given the output m of the respective measurement. The probability of obtaining this outcome for the given initial state $|\psi(n)\rangle$ now equals

$$\mathrm{Pr}_{n+1}(m) = \|K_m |\psi(n)\rangle\|^2. \tag{6.15}$$

which is different from the probability $\mathrm{Pr}_{n+1}(m)$ in Eq. (6.11). Given that the internal state space is two-dimensional, only two different measurement outcomes, $m = A, B$ can be obtained. The probabilities for these two outcomes add up to

one when

$$K_A^\dagger K_A + K_B^\dagger K_B \;=\; I \,, \tag{6.16}$$

where I denotes the identity operator.

Again, when the measurement outputs are ignored, we cannot know the states $|\psi(n)\rangle$ of individual HQMMs after n time steps, even when their initial state $|\psi(0)\rangle$ is known. In this case, we describe the quantum states of the machine by density matrices $\rho(n)$, which replace the probability vectors $\boldsymbol{p}(n)$ that we used in the previous two subsections. The density matrices $\rho(n)$ allow us to predict the dynamics of expectation values, like the probability of finding the HQMM at a certain time step in a certain internal state. Instead of Eq. (6.1), the dynamics of the density matrix of a HQMM is given by

$$\rho(n+1) \;=\; \mathcal{K}(\rho(n)) \,, \tag{6.17}$$

with the superoperator $\mathcal{K}$ defined such that

$$\mathcal{K}(\rho(n)) \;=\; \sum_{m=A,B} K_m \rho(n) K_m^\dagger \,. \tag{6.18}$$

In other words, the Kraus operators K_A and K_B replace the transition matrices T_A and T_B which we introduced in the previous subsection. For example, the probability $\mathrm{Pr}_{n+1}(m)$ of generating an output m in step $n+1$ now equals

$$\mathrm{Pr}_{n+1}(m) \;=\; \mathrm{Tr}\left(K_m \rho(n) K_m^\dagger \right) \,, \tag{6.19}$$

where the trace, Tr, denotes the sum of all the diagonal matrix elements.

6.2 Parametrisation, stationary states and different observable properties

In this section, we parametrise the machines that we introduced in the previous section and highlight the constraints that must be satisfied by each model. In addition, we determine stationary state distributions whenever possible and

calculate the probabilities for certain output sequences. For simplicity, we assume in the following that all three machines are ergodic due to their finite size and, therefore, possess a stationary state. Therefore, calculated sequence probabilities apply to the outputs of large ensembles of machines, which have all already reached their stationary states.

6.2.1 Markov models
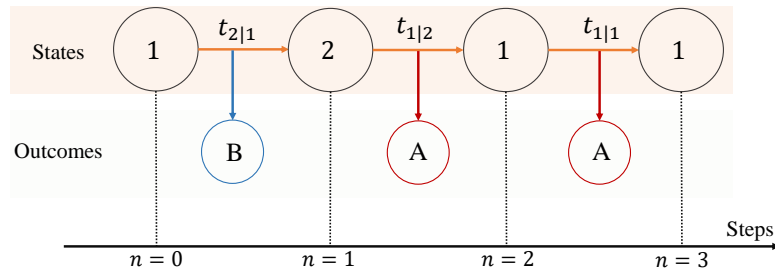
Figure 6.4: A Markov model that has two states 1 and 2, and the transition between states over time is governed by the transition probability matrix T. The orange arrows show the evolution of the Markov model with time, while the blue and red arrows show the generated outputs, A and B, at each time step n.

From probability theory, we know that the matrix elements of the transition matrix T in Eq. (6.5) are all between zero and one. In addition, they must obey the condition

$$t_{1|i} + t_{2|i} = 1,\tag{6.20}$$

for $i = 1, 2$ to ensure that the machine always transitions into one of its two available states, A and B. For a two states MM, the transition matrix T has four matrix elements and there are two constraints, we can parametrise one-bit MMs using only two independent parameters, p and q. More concretely, we write T in

the following as

$$T = \begin{pmatrix} p & 1-q \\ 1-p & q \end{pmatrix}, \tag{6.21}$$

with parameters $p, q \in (0, 1)$. Here, $t_{1|1} = p$, $t_{2|2} = q$, $t_{2|1} = 1-p$ and $t_{1|2} = 1-q$. In the next section, we will choose p and q randomly to generate a large set of all possible random machines and study the properties of their output sequences.

The possible output sequences of each machine depend, for example, on their respective initial state $\boldsymbol{p}(0)$. However, if the machine is ergodic and its outputs are ignored for a certain initial minimum amount of time, it soon assumed that the machine has reached a stationary state $\boldsymbol{p}_{\text{ss}} = (p_1, p_2)^{\text{T}}$ with

$$T\,\boldsymbol{p}_{\text{ss}} \;=\; \boldsymbol{p}_{\text{ss}}. \tag{6.22}$$

Using Eq. (6.21) and taking into account that p_1 and p_2 must add up to one, one can show that [147]

$$p_1 = \frac{1-q}{2-p-q}, \quad p_2 = \frac{1-p}{2-p-q}. \tag{6.23}$$

These probabilities give the likelihood to find a certain machine in states 1 and 2, respectively. Hence, they also equal the probabilities to obtain the outputs A and B at any time n, respectively, if the previous outputs of the machine are unknown and cannot be taken into account. A schematic diagram representing the dynamics of state evolution in the MM is shown in Fig. 6.4.

Suppose the machine has initially been prepared in its stationary state $\boldsymbol{p}_{\text{ss}}$. Then the probability $P(i_1 i_2 \ldots i_m)$ of obtaining the output sequence $i_1 i_2 \ldots i_m$ of length m simply equals

$$P(i_1 i_2 \ldots i_m) \;=\; t_{i_m|i_{m-1}} \ldots t_{i_3|i_2} t_{i_2|i_1}\, p_{i_1}, \tag{6.24}$$

with p_{i_1} given in Eq. (6.23). For example, the probability of creating a sequence of length $m+2$ that starts and ends with the output symbol A and otherwise only contains B's equals

$$P_m(AB \ldots BA) \;=\; \frac{(1-p)(1-q)^2}{2-p-q}\, q^{m-1}. \tag{6.25}$$

Furthermore, we can evaluate the probability of a sequence of length $m + 2$ to start and to end with the output symbol A as

$$P_m(A * \ldots * A) \;\; = \;\; \frac{1-q}{2-p-q} \, (1,0) \, T^{m-1} \begin{pmatrix} 1 \\ 0 \end{pmatrix} . \tag{6.26}$$

Probabilities like the ones above may be utilised to assess the complexity of the machine. For example, the probability $P_m(A * \ldots * A)$ can tell us how long correlations persist in the output sequences of a machine. For large m, the probability $P_m(A * \ldots * A)$ tends to p_1, and any knowledge about having been prepared in state 1 exactly $m + 1$ steps earlier is lost.

6.2.2 Hidden Markov models
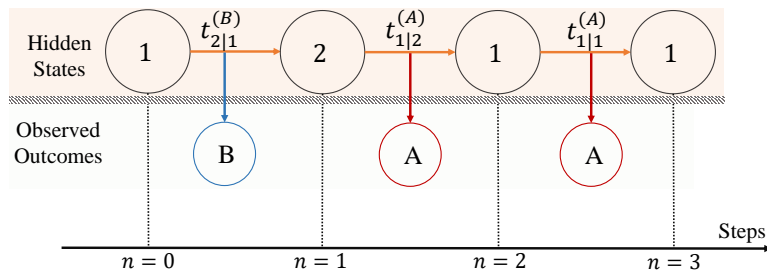
Figure 6.5: A hidden Markov model that has two states 1 and 2, and the transition between states over time is governed by the transition probability matrix T_m evolution over time. The diagram shows one possible route for evolving the hidden Markov model with time. The orange arrows show the evolution of the hidden Markov model with time, while the blue and red arrows show the generated outputs, A and B, at each time step n.

As we have seen in Section 6.1.2, the description of Mealy HMMs [143] with two outputs and N internal states requires two transition matrices T_m with N^2 matrix elements $t_{j|i}^{(m)}$. A schematic diagram representing the dynamics of state evolution in the HMM is shown in Fig. 6.5.

To identify the number of independent parameters needed to numerically simulate all possible HMMs, we first notice that the matrix elements $t_{j|i}^{(m)}$ and the elements $t_{j|i}$ in Eq. (6.6) are all between zero and one. To further ensure that the machine always transitions into a new state, while producing an output, we also require that

$$\sum_{j=1}^{N} t_{j|i} \;=\; 1\,, \tag{6.27}$$

with the matrix elements $t_{j|i}$ defined as in Eq. (6.6). Hence, the transition matrix T in Eq. (6.9) is an $N \times N$ matrix with $N(N-1)$ free parameters. Once this matrix is fixed, the sub-transition matrix T_A can assume N^2 positive free parameters, but these are bounded from above by the matrix elements of T. Hence, in total, the characterisation of a Mealy HMM requires $(2N-1)N$ independent parameters.

The stationary state is again the distribution vector $\boldsymbol{p}_{\mathrm{ss}}$, which is an eigenvector of the transition matrix T such that $T\boldsymbol{p}_{\mathrm{ss}} = \boldsymbol{p}_{\mathrm{ss}}$, as stated in Eq. (6.22). In cases of ergodicity, the state vector $\boldsymbol{p}_{\mathrm{ss}}$ can be found, for example, numerically by applying T repeatedly to an initial state until the state of the machine remains the same. For simplicity, we assume in the following, that our HMMs always have only one stationary state.

Since the transitions of a HMM are governed by two sub-transitions matrices, namely T_A and T_B, the probability $P(i_1 i_2 \ldots i_m)$ for generating the output sequence $i_1 i_2 \ldots i_m$ now reads

$$P(i_1 i_2 \ldots i_m) \;=\; \eta\, T_{i_m} \ldots T_{i_2} T_{i_1}\, \boldsymbol{p}_{\mathrm{ss}}\,, \tag{6.28}$$

where $\eta = (1, 1, \ldots, 1)$ is now a row vector of dimension N. More concretely, the probability $P_m(AB \ldots BA)$ in Eq. (6.25) becomes

$$P_m(AB \ldots BA) \;=\; \eta\, T_A T_B^m T_A\, \boldsymbol{p}_{\mathrm{ss}}\,. \tag{6.29}$$

If we ignore the m output symbols between the first and the last A, this probability changes into

$$P_m(A * \ldots * A) \;=\; \eta\, T_A T^m T_A\, \boldsymbol{p}_{\mathrm{ss}}\,. \tag{6.30}$$

All three probabilities differ significantly from the probabilities in Eqs. (6.24)–(6.26). As we shall see in the next section, HMMs can produce slightly more correlated output sequences because of their hidden memory.

6.2.3 Hidden quantum Markov models
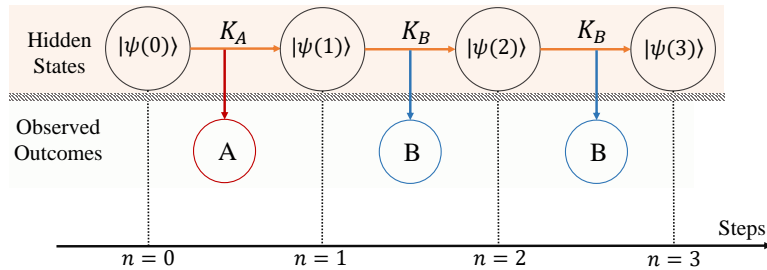
Figure 6.6: A hidden quantum Markov model evolution over time. Here the transition between states over time is governed by the transition probability matrix K_m. The orange arrows show the evolution of the hidden quantum Markov model state $|\psi(n)\rangle$ with time, while the blue and red arrows show the generated outputs, A and B, at each time step n.

Next, we examine how to parametrise HQMMs. Their generalised measurements can be realised by allowing the qubit, which encodes the hidden state of the machine, to interact with an ancillary quantum system (i.e. an environment), followed by projective measurements on a coarse-grained time scale Δt. In every time step, some hidden information can leak into the environment. Markovianity requires that the ancilla (i.e. the environment), be reset to the same initial state after each measurement. In this way, the dynamics of the HQMM depend only on the current state of its qubit. In Fig. 6.6, we illustrate the stochastic dynamics of the qubit and the random measurement outcomes that might be produced in a single run of such a machine.

6.2.3.1 Parametrisation of Kraus operators

To parametrise the Kraus operators K_A and K_B of one-qubit HQMMs, we write them in the following as

$$K_m = \begin{pmatrix} k_{00}^{(m)} & k_{01}^{(m)} \\ k_{10}^{(m)} & k_{11}^{(m)} \end{pmatrix} . \tag{6.31}$$

The eight complex matrix elements of K_A and K_B can be represented by 16 real parameters. However, as pointed out in Eq. (6.16), these operators must obey a matrix equation, which implies that

$$
\begin{aligned}
\sum_{m=A,B} |k_{00}^{(m)}|^2 + |k_{10}^{(m)}|^2 &= 1 \,, \\
\sum_{m=A,B} |k_{01}^{(m)}|^2 + |k_{11}^{(m)}|^2 &= 1 \,, \\
\sum_{m=A,B} k_{00}^{(m)} k_{01}^{(m)*} + k_{10}^{(m)} k_{11}^{(m)*} &= 0 \,, \\
\sum_{m=A,B} k_{00}^{(m)*} k_{01}^{(m)} + k_{10}^{(m)*} k_{11}^{(m)} &= 0 \,.
\end{aligned}
\tag{6.32}
$$

These four equations impose four (real) constraints on the above-mentioned 16 real parameters, thereby reducing the total number of free (real) parameters needed to fully characterise one-qubit HQMMS to 12. This means, HQMMs can be characterised by fewer parameters than HMMs with the same number of outputs, A and B, in case the HMM has more than two internal states.

6.2.3.2 Stationary states

If a track record of all measurement outcomes is kept, a HQMM that has initially been prepared in a pure state $|\psi(0)\rangle$, can always be described by a pure state $|\psi(n)\rangle$. However, as mentioned already in the previous section, if this is not the case and measurement outcomes are ignored, the HQMM must be described by a density matrix $\rho(n)$ instead. How this density matrix evolves from one time step to the next is shown in Eq. (6.17). Its stationary state is, therefore, the density matrix ρ_{ss} with

$$\mathcal{K}(\rho_{\text{ss}}) = \rho_{\text{ss}} \tag{6.33}$$

with the superoperator $\mathcal{K}$ defined in Eq. (6.18). Since the HQMM is a two-level system, its stationary state density matrix $\rho_{\rm ss}$ can be written as

$$\rho_{\rm ss} \;=\; \begin{pmatrix} \rho_{00} & \rho_{01} \\ \rho_{10} & \rho_{11} \end{pmatrix} , \tag{6.34}$$

with two real matrix elements, ρ_{00} and ρ_{11}, and two complex matrix elements, ρ_{01} and ρ_{10}, and with

$$\rho_{00} + \rho_{01} \;=\; 1 \,,$$
$$\rho_{01} \;=\; \rho_{10}^{*} \,. \tag{6.35}$$

In principle, using Eqs. (6.31)–(6.35), it is now possible to calculate the stationary state density matrix $\rho_{\rm ss}$ of HQMMs analytically, but the resulting equations do not provide much insight, since they still contain 12 free parameters.

6.2.3.3 Sequence probabilities

As before, we now have a closer look at sequence probabilities. For example, the probability $P(i_1 i_2 \ldots i_m)$ in Eqs. (6.24) and (6.28) now equals

$$P(i_1 i_2 \ldots i_m) \;=\; {\rm Tr}\left(K_{i_m} \ldots K_{i_2} K_{i_1} \, \rho_{\rm ss} \, K_{i_1}^{\dagger} K_{i_2}^{\dagger} \ldots K_{i_m}^{\dagger} \right) , \tag{6.36}$$

with the Kraus operators K_m given in Eq. (6.31). Moreover, the probabilities $P_m(AB \ldots BA)$ and $P_m(A * \ldots * A)$ are now given by

$$P_m(AB \ldots BA) \;=\; {\rm Tr}\left(K_A K_B^m K_A \, \rho_{\rm ss} \, K_A^{\dagger} K_B^{m\,\dagger} K_A^{\dagger} \right) , \tag{6.37}$$
$$P_m(A * \ldots * A) \;=\; {\rm Tr}\left(K_A \, \mathcal{K}^m \left(K_A \rho_{\rm ss} K_A^{\dagger} \right) K_A^{\dagger} \right) , \tag{6.38}$$

with the superopertor $\mathcal{K}$ given in Eq. 6.18.

6.3 A comparison of the complexity of MMs, HMMs and HQMMs

In this section, we use the parametrisation of MMs, HMMs, and HQMMs with two output symbols, which we introduced in the previous section, to study

the sequence probabilities that these machines can generate. As we shall see below, there is not much difference between the complexity of MMs and HMMs. Moreover, we find that increasing the number of internal states does not significantly change the correlation range of output symbols in case of HMM. The possible correlations between output symbols seem to disappear relatively quickly, after only a few time steps.

6.3.1 Markov model

The analysis of Markov chains is considered relatively straightforward due to the availability of information regarding both the states and the transition matrix. However, Markov chain-based systems exhibit a lack of long-term correlations between measurements. As a measure of the correlations between measurements, we examine the autocorrelation function of a MM. As an example, for evaluating the autocorrelation function, we consider an ergodic MM that has two states. We assume that the transition matrix T that governs the transitions between states is defined as,

$$T = \begin{pmatrix} p & 1-p \\ 1-p & p \end{pmatrix}.$$
(6.39)

where $p = 0.4$. The autocorrelation function exhibit a decay pattern over time, as shown in Fig. 6.7, which occurs rapidly as the duration between measurements increases. The rapid decline suggests that there are no or limited correlations between measurements. This outcome is not surprising, as MMs have a Markov property that indicates the dependence of the future state on the current state only. Therefore, long-term correlations between states are lost as the time between states increases. Here, stationary states are assessed by computing the probability distribution iteratively and evaluating the results. As illustrated in Fig. 6.8, the probability of detecting the system in a particular state experiences some fluctuations until it reaches a stationary state. For the transition matrix used for examining the behaviour of the probability distribution of the MM for a long time, we consider an ergodic MM that has three states. Let the initial state

of the MM is given by

$$\boldsymbol{p}(0) = \begin{pmatrix} 1 \\ 0 \\ 0 \end{pmatrix}. \tag{6.40}$$

Moreover, the transition matrix T of the model is chosen to be

$$T = \begin{pmatrix} 0.2 & 0.8 & 0.3 \\ 0.7 & 0 & 0 \\ 0.1 & 0.2 & 0 \end{pmatrix}. \tag{6.41}$$
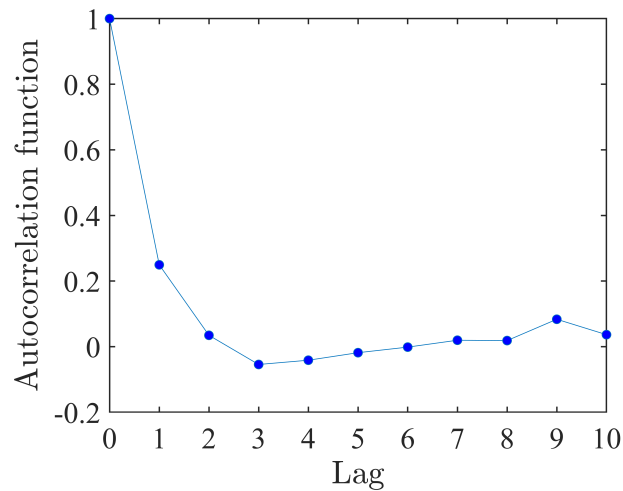
Figure 6.7: The plot of the autocorrelation function of a Markov model as a function of time lag. Here, we see the rapid decline in the autocorrelation function with the increase in the time lag as the correlations between measurements decrease significantly after few time steps.
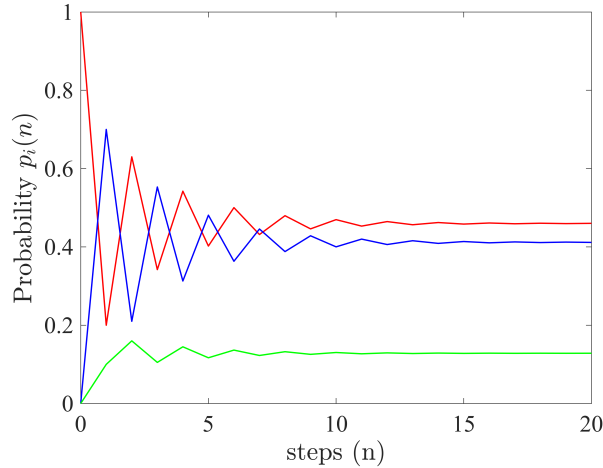
Figure 6.8: The probability of finding being in a state $p_i(n)$ as a function of time steps n. Here, the probability of being in the first state is $p_1(n)$ (red), the probability of being in the second state is $p_2(n)$ (blue), and the probability of being in the third state is $p_3(n)$ (green)

6.3.2 Simulating HMMs with more than two internal states

Before going into the details of the comparison between the three models mentioned previously, we discuss the effect of increasing the number of states in HMM on the complexity of the dynamics of the model, while keeping the number of outcomes the same as previously discussed: A and B only. Note here that we can not study the effect of increasing the number of states in the MM since that is technically impossible as the number of states is directly proportional to the number of outputs. To study the effect of increasing the number of internal states in HMMs, we produce a scatter plot of the probability of observing a sequence of outcomes, more specifically $P(BAAAB)$ as a function of $P(B)$ for two internal states machine $S = 2$, three internal states machine $S = 3$ and four internal states machines $S = 4$. Here, each plot was generated using 10^5 random machines that satisfy the parametrisations and conditions imposed on HMMs. As shown in Fig. 6.9, the differences between the three plots are almost negligible, which may be attributed to the fact that we only restricted the machines to have only two
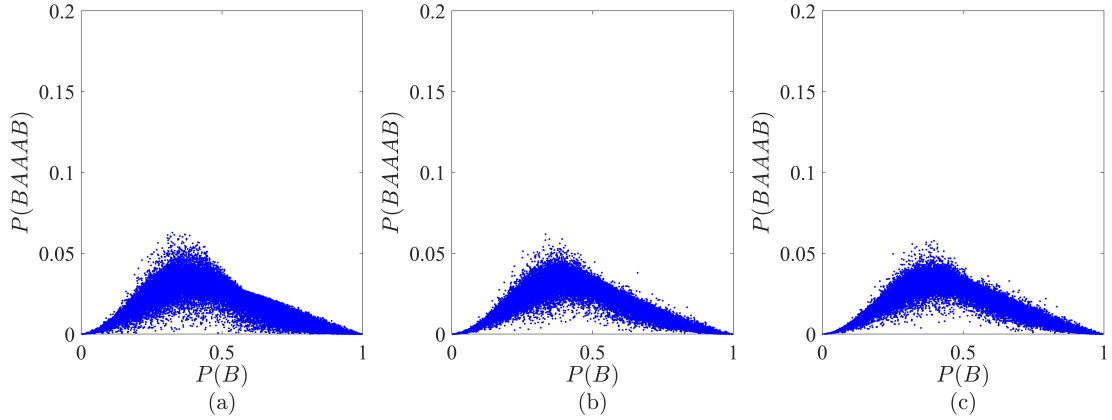
Figure 6.9: The probability $P(BAAAB)$ as function of $P(B)$ for a Hidden Markov model with two internal states $S = 2$ (a), three internal states $S = 3$ (b) and four internal states $S = 4$ (c). The three sub figures were generated by evaluating the probability of observing the sequence $P(BAAAB)$ for 10^5 random machines for each plot.

outcomes, therefore, we may argue that in this case (i.e. two output with two internal states model) the model with two internal states already represents the optimum number of states to simulate such a model. Expanding the HMM to include more than two internal states does not yield significant improvements to the complexity of the dynamics of the model, as the space occupied by the random machines for each model generated in Fig. 6.9 (a) is almost the same for Fig. 6.9 (b) and Fig. 6.9 (c). Furthermore, as the number of internal states increases, the complexity of the simulations also increases. Therefore, it is crucial to carefully select the number of states, taking into consideration the potential benefits gained by increasing the number of states and the rise in simulation complexity as a result of increasing the number of states. Therefore, within the framework proposed here it is concluded that there is no significant benefit in increasing the number of internal states of HMMs beyond two states. For details about the calculation of the stationary states of the HMM with three and four internal states refer to appendix C.

6.3.3 An example of a HQMM

As we have seen in Section 6.2, a complete parametrisation of 1-qubit HQMMs requires 12 real parameters. However, to show that HQMMs are more complex than HMMs, we only need to present one example of a machine that cannot be modelled classically by linear HMMs and MMs. Keeping this in mind, we only consider the following HQMMs with Kraus operators K_A and K_B which can be written as

$$K_A = \begin{pmatrix} \cos\varphi & -a\sin\varphi \\ \sin\varphi & a\cos\varphi \end{pmatrix}, \quad K_B = \begin{pmatrix} 0 & \sqrt{1-a^2}\,\sin\vartheta \\ 0 & \sqrt{1-a^2}\,\cos\vartheta \end{pmatrix}.$$

$$(6.42)$$

Here a, φ and ϑ are three real parameters with

$$a \in (0,1), \quad \varphi \in (0,2\pi), \quad \vartheta \in (0,2\pi). \tag{6.43}$$

It is relatively straightforward to check that the above operators are indeed valid Kraus operators.

The stationary state of the 1-qubit HQMM is calculated for the Kraus operators of Eq. (6.42) using Eq. (6.31) and Eq. (6.32). The expression of the stationary density matrix ρ_{ss} is been calculated numerically using `solve` function in MATLAB. Due to the complexity of the expression, refer to the appendix D for details about the calculation of the stationary density matrix ρ_{ss}.

6.3.4 A comparison of the performance of the machines

This section outlines a comparative analysis of three models, namely the MM, the HMM and the HQMM. The assessment of correlations in sequential measurements within each model involves the computation of the probability of observing particular sequences using various random machines of each model. The probability of obtaining a certain sequence, for each of the three models, was calculated for a large number of randomly generated machines that satisfy the parametrisation conditions of each model.

6.3 A comparison of the complexity of MMs, HMMs and HQMMs

In order to compare between the MM, HMM and HQMM, we consider the probability of observing the sequence $BAAAB$. To calculate the probability of observing the sequence $P(BAAAB)$, we start by defining the transition matrices and the stationary states of each of the three models. In the MM and HMM, we consider 1-bit machines with two states and two possible outcomes A and B. For the HQMM, we consider a 1-quibt machine with two possible outcomes A and B.

We start the simulation by defining the transition matrix T for the MM, the transition matrix T and the sub-transition matrices T_A and T_B for HMM and the sub-transition matrices K_A and K_B for the HQMM. All of these transition matrices are defined so that they fulfil the constraints imposed on each model. After that, we determine the stationary state of each model and subsequently evaluate the probability of observing the sequence $P(BAAAB)$. Then, the probability of observing $P(BAAAB)$ is recalculated for a total of 10^5 randomly generated machines, where at each iteration we generate new transition matrices for each model as previously stated. Finally, we create a scatter plot of the probability of observing the sequence $P(BAAAB)$ for each model as a function of $P(B)$.

In Fig. 6.10 the selected sequence for simulation is $BAAAB$, where $P(BAAAB)$ representing the probability of observing the outcome B subsequent to three consecutive occurrences of AAA, given that the initial outcome is B. As Fig. 6.10 illustrates, the HQMM (Fig. 6.10-[c-red]) exhibits better performance due to its ability to occupy a larger state space compared to its classical counterparts, namely the MM (Fig. 6.10-[a-green]) and the HMM (Fig. 6.10-[b-blue]). Furthermore, it can be observed that the HMM exhibits greater correlations in comparison to the basic MM. In other words, this sequence provides an insight into the correlation between two B outcomes that are spaced apart by multiple observations of A. Therefore, we may argue that the probability of getting this particular sequence is higher in the case of the HQMM than its classical counterparts, namely MM and HMM.

To assess the ability of each model to produce correlated sequences with high probability, we analyse the probability of observing a sequence denoted as
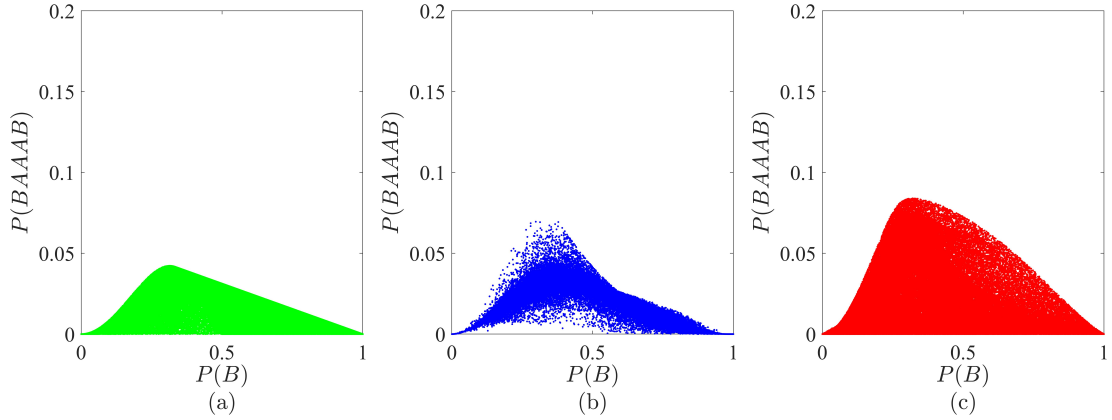
Figure 6.10: The probability of observing a sequence $P(BAAAB)$ as a function of $P(B)$ for MM (a-green), HMM (b-blue) and HQMM (c-red). A comparison between the three models shows higher probability to observe this sequence using the HQMM over its classical counterparts, HMM and MM. For each model, the simulation was iterated for 10^5 randomly generated machines.

$P(ABA, T^n, ABA)$ as a function of $P(B)$. This probability is defined as the probability of observing the sequence ABA followed by another sequence ABA while ignoring some outcomes, for n steps, in between the observation of the two sequences. To examine this probability, we graph $P(ABA, T^n, ABA)$ as a function of $P(B)$. Here, Fig. 6.11 illustrates the capability of three models, namely the MM, the HMM, and the HQMM, to display correlation in observing the sequence $P(ABA, T^n, ABA)$. The probability of obtaining the sequence using the MM is presented in Fig. 6.11 (a)–(c) (green). It shows a slight decline in the probability of observing the correlated sequences as we increase the number of ignored steps n. Furthermore, it should be noted that the dimensional space spanned by the MM is considerably smaller in comparison to that of the HMM and the HQMM. Additionally, the HMM, shown in Fig. 6.11(a)–(c) (blue), shows a higher probability of observing the correlated sequences than the MM when the number of ignored steps increases. Nonetheless, the HQMM, shown in Fig. 6.11 (a)–(c) (red), demonstrates better performance in comparison to the HMM and MM. In

brief, one might argue that the considered example of 1-quibt HQMM, which is a subset of HQMMs, has the potential to demonstrate correlated sequences with higher probability than the classical counterparts.

Another example that illustrates the correlations among measurements is shown in Fig. 6.12. Here, we plot the probability of observing the sequences $P(ABAB, T^n, ABAB)$ as a function of $P(B)$ while ignoring certain number outcomes in between the observation. Similar to Fig. 6.11, Fig. 6.12 shows the same behaviour where in the HQMM the probability of observing this sequence is slightly higher even when the measurements are ignored in between observations. Additionally, it should be noted that the alteration of the chosen sequence results in a variation of the space covered by each model, as well as the decline in the probability of observing a certain sequence.

To visually represent the long-term correlations among the three models, we examine the probability of observing the two outcomes of value B separated by some ignored measurements in between. In other words, we evaluate the probability $P(B, T^n, B)$ for the three models. To investigate the effect of the ignored measurements, we calculate the Euclidean distance between the probability $P(B, T^n, B)$ and the curve of $(P(B))^2$ for each time step n. Based on the fact that after many time steps, the probability of the sequence $P(B * * B)$ scales with $(P(B))^2$ in the absence of correlations between intermediate measurements. Thus, the Euclidean distance is evaluated between the probability $P(B, T^n, B)$ and the curve $(P(B))^2$ at each time step n can be thought to be a measure of the spread around the curve $(P(B))^2$. Notably, as shown in Fig. 6.13, the MM demonstrates a decline in the Euclidean distance faster than the HMM and the HQMM. Furthermore, the correlations present in the HMM demonstrate a relatively gradual decay, whereas the HQMM exhibits a slower decay than the HMM and the MM. Thus, we may infer that in HQMM, it is likely to observe correlated outcomes even when some measurements are being ignored between observations of the two outcomes.

The quantum advantage, in terms of the existence of temporal correlations and the high probability of observing correlated sequences, demonstrated by the

simulations of the HQMMs over the HMMs and MMs, can be related to the measurement enhancement shown earlier in the open quantum system of the two-cavity network. As it was mentioned earlier, the operator sum representation formalism, in the form of Kraus operators, can be viewed as a method for simulating the evolution of the density matrix as a function of time by employing quantum information principles. This formalism demonstrated that the use of Kraus operators can represent a general formalism for evolving the system under the conditions of the Markov approximation and coarse-grained time evolution. These Kraus operators evolve the system over an infinitesimal time interval Δt. Since the chosen evolution time step is larger than the environment's evolution time, the environment can be assumed to be in its preferred state after every time step. This 'stroboscopic' evolution of the system is similar to the type of evolution observed in the HQMM consisting of a principal system and an ancillary system. At each time step, the system evolves according to the Kraus operators based on the evolution path chosen under the Markovian evolution assumption and coarse-grained time evolution. After each evolution, the ancillary system, which represents the environment, is reset to its preferred state. Hence, we may anticipate that an open quantum system that evolves according to the Kraus operators is an example of a HQMM. Consequently, we can also anticipate that the two-cavity network within an instantaneous feedback loop may be considered an example of an HQMM.
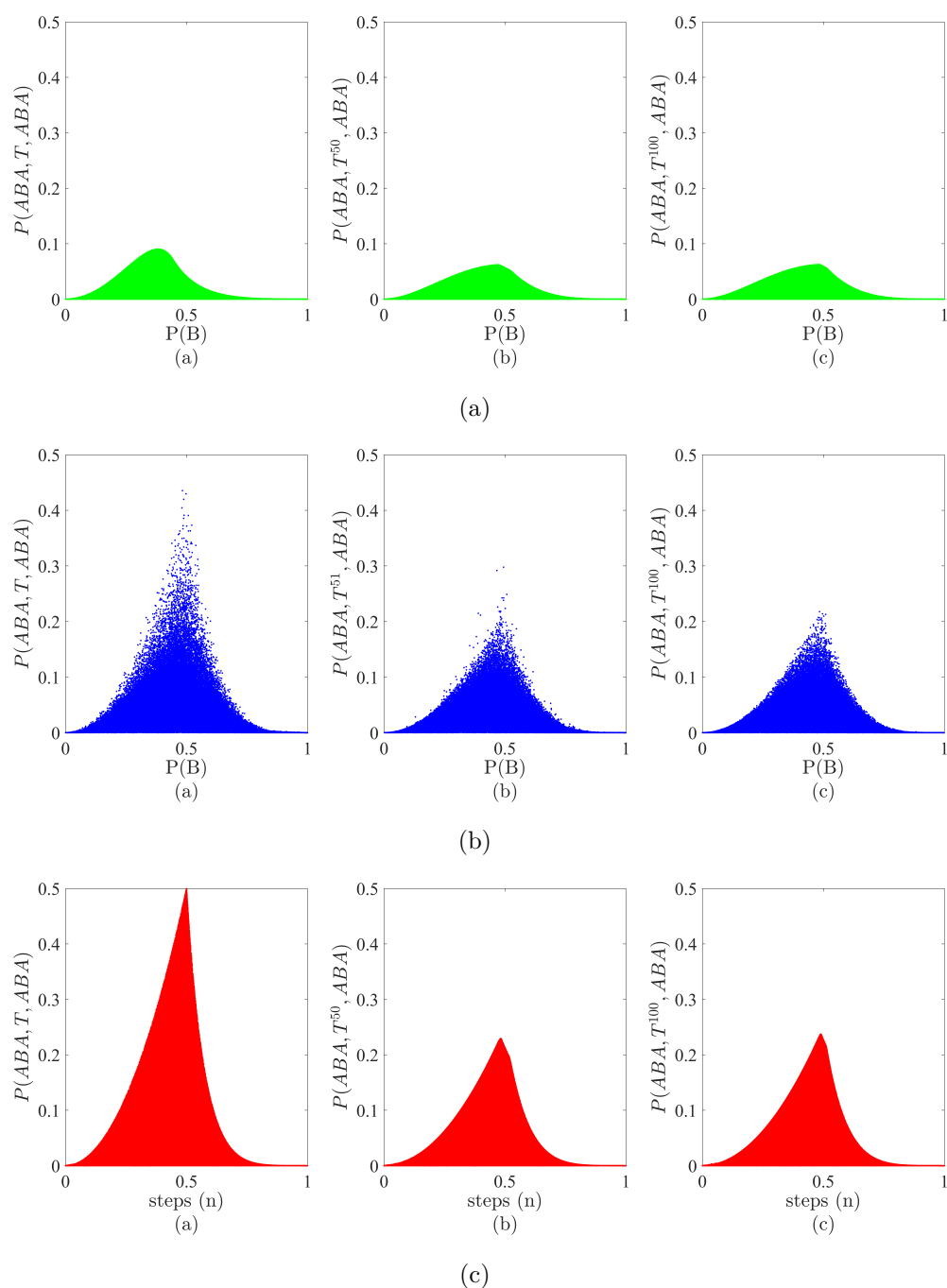
Figure 6.11: The probability of observing $P(ABA, T^n, ABA)$ as function of $P(B)$ for the MM (green), the HMM (blue), and HQMM (red) while ignoring some outcomes between observations of the two sequences of ABA. Here, n is the number of ignored steps; (a) is for $n = 1$, (b) is for $n = 50$, and (c) is for $n = 100$ for the HMM and HQMM. For the MM the number of ignored steps (a) is for $n = 2$, (b) is for $n = 51$, and (c) is for $n = 101$. For each model, the simulation was iterated for 10^6 randomly generated machines.
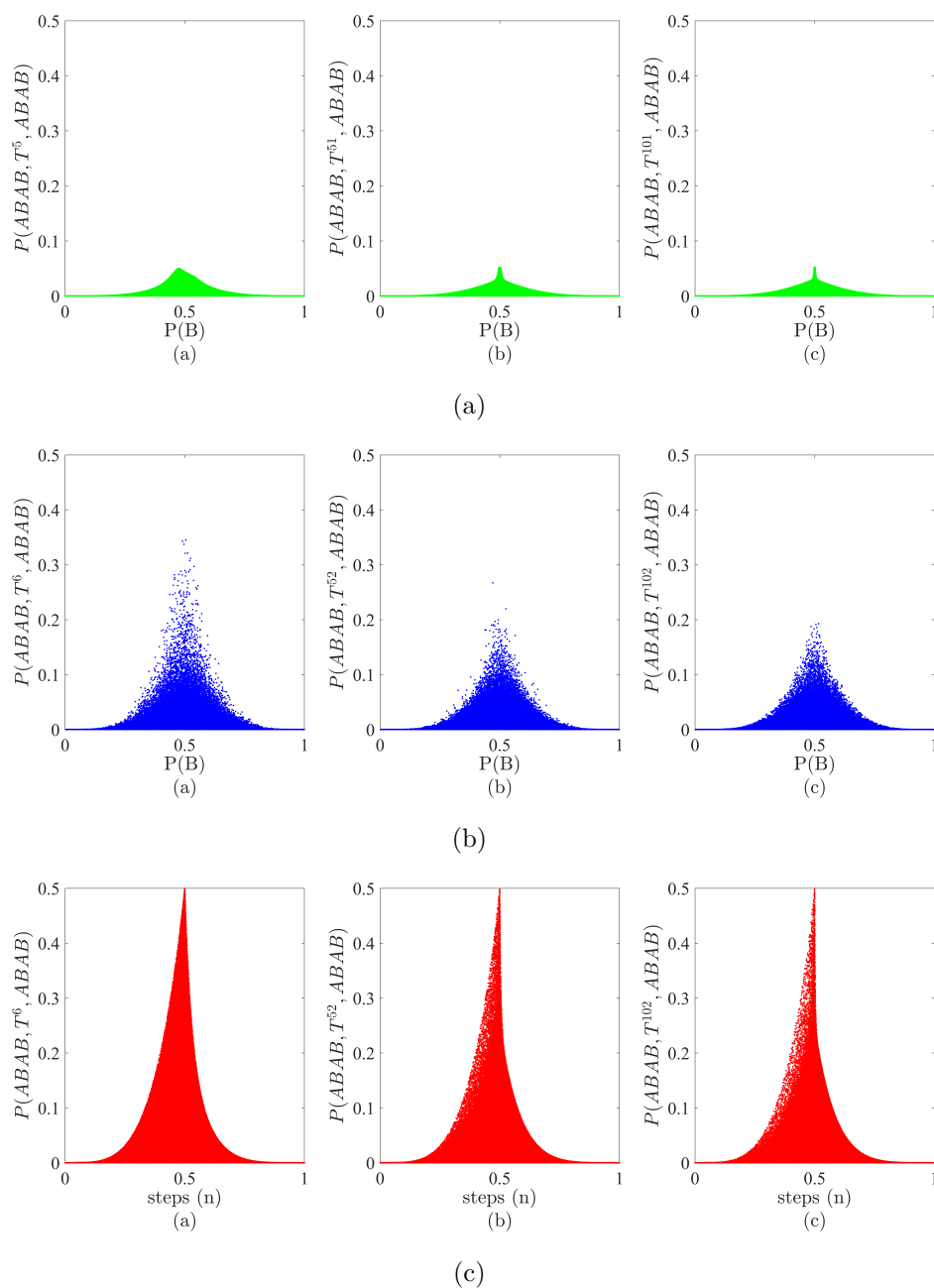
Figure 6.12: The probability of observing $P(ABAB, T^n, ABAB)$ as a function of $P(B)$ for the MM (green), HMM (blue) and HQMM (red) while ignoring some outcomes between the observations of the two sequences of $ABAB$. Here, n is the number of ignored steps the ignored steps are (a) $n = 6$, (b) $n = 52$ and (c) $n = 102$. The simulations where iterated for 10^6 for each model.
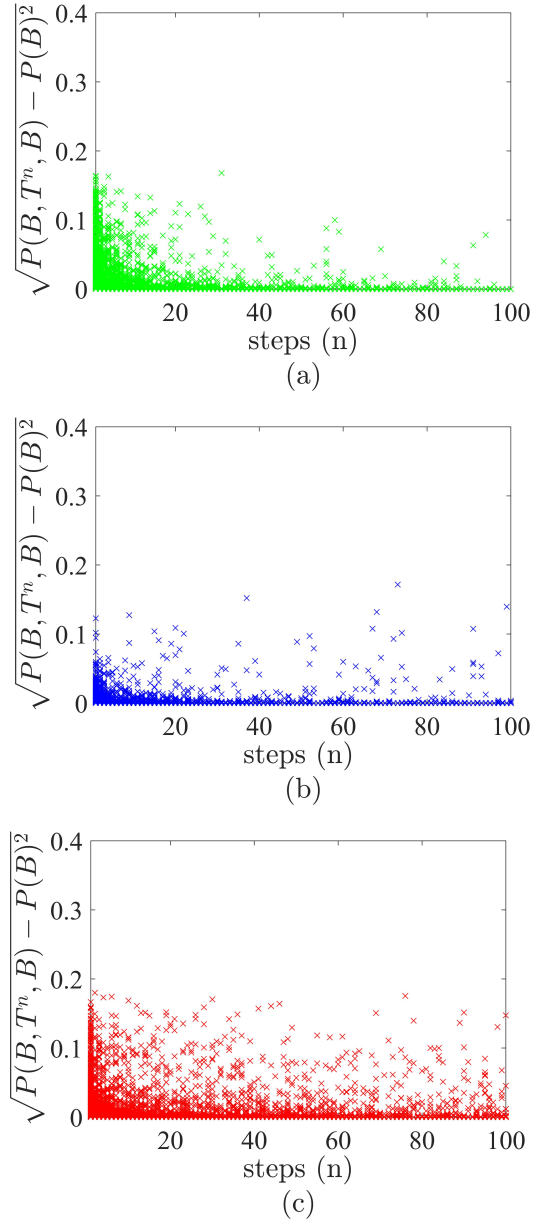
Figure 6.13: The Euclidean distance $\sqrt{P(B,T^n,B) - (P(B))^2}$ as function of ignored steps n calculated for (a) the Markov model (green), (b) the hidden Markov model (blue), and (c) the hidden quantum Markov model(red). For each model, the simulation was iterated for 4×10^4 randomly generated machines.

6.4 Summary

In the this chapter, a theoretical overview of MMs, HMMs, and HQMMs was discussed thoroughly. Our study involved the analysis of the constraints imposed on the transition matrix for each model and an exploration of the sub-transition matrices that arise in the HMMs and HQMMs. Furthermore, a comprehensive discussion was conducted on the parametrisation of each model, and the stationary distribution was determined for the evaluation of the particular probability sequences to be used later on for a performance comparison between the three models. Subsequently, we engaged in a discussion regarding the ability of each model to display temporal correlations between consecutive measurements. It has been observed that the correlations between measurements within MMs exhibit a rapid decay as the number of the time steps between measurements increases. The phenomenon of decay was also observed in the plot of the autocorrelation function of the MM, where the autocorrelation function as a function of time lag exhibited an exponential decay. The present study investigated the impact of increasing the internal states while maintaining a constant number of output outcomes. Our findings suggest that there is no significant advantage associated with increasing the internal states for the chosen sequence. Additionally, the probability of observing the sequence $P(BAAAB)$ was evaluated for the three models. The HMM demonstrated a slightly higher probability of observing the tested sequences compared to the MM, however, the one-qubit HQMM demonstrated a higher probability of observing the sequence than both the HMM and the MM. Furthermore, the ability to observe sequences, namely $P(ABA, T^n, ABA)$, $P(ABAB, T^n, ABAB)$, and $P(B, T^n, B)$, while ignoring measurements in between observations was tested for all three models. The HQMM showed a higher probability of getting the sequences and a higher probability of observing correlations between the sequences.

Chapter 7

Conclusion

Quantum jump metrology implemented in a scheme within a quantum feedback loop has demonstrated the potential to achieve measurement accuracy limits exceeding the SQL without requiring complex linear optics or entangled photons. We started by introducing a comprehensive analysis of the traditional method for quantifying the phase shift difference in an interferometer for benchmarking purposes. In addition, to gain a deeper understanding of the theoretical framework of our proposed scheme, a comprehensive overview of the behaviour of the one cavity network in a quantum feedback loop was presented. Afterwards, we proposed an expanded scheme for two-cavity network and two phase shifters within a feedback pulse loop that is more practical and efficient than the one-cavity network. Using pair coherent state and transformation matrices, the system dynamics of a two-cavity network were described, and measurements were analysed using the developed Kraus operators.

The optical network of two cavities scheme employing quantum jump metrology demonstrated the potential to achieve measurement accuracy with a scaling that exceeds the SQL, given the optimal input parameters, without the need for complex quantum properties such as entanglement. As in previous research, the presence of quantum jumps as photon emissions is continuously monitored. The subsequent driving of the cavities induces nonlinearities in the system dynamics, thereby causing correlations in the photon statistics observed by the detectors.

In the experimental configuration we examined, the cavities are always in a coherent state. Although photon emission does not alter the state of the cavities, it provides information regarding the state of the resonators. Similarly, the absence of photon observation reveals information. The dependence of the quantum feedback induced dynamics on the parameter that we wish to measure leads to effective ergodicity breaking in the dynamics of the system, resulting in two distinct classes of trajectory [64]. The scaling could be achieved by preparing the cavities in an initial state that is more complex than a coherent state. However, the use of coherent states simplifies experimentation, allowing the proposed scheme to be operated more easily and for extended durations.

A limitation of this scheme is that the outcomes can solely be obtained through numerical means, and the computation of Fisher information is only calculated for short durations. As a result of the close correspondence between the projected boundary and the anticipated uncertainty derived from our measurement signal, we believe that our fitting of the Fisher information is reasonable. An alternative measurement protocol for obtaining information about the phase would consist of utilising all data gathered during the continuous monitoring of the cavity network and employing a Bayesian inference procedure. In an open system where photon statistics are observed, this is likely the most intuitive method for measuring an unknown parameter. This could be supplemented further by a strong quantum measurement of the cavity state at the end of the observation, which would supplement the information obtained from monitoring photon statistics. However, for the purposes of this study we only regard the Fisher information as a proof of concept for the existence of a quantum enhancement. Due to this property, cavity networks are likely to receive increased interest for quantum sensing applications and may play a crucial role in the development of quantum machine learning devices. A long-term aim of the work that we present here is to design novel schemes for quantum computational networks based on optical interferometers.

Furthermore, the optical cavity network has been shown to represent an example of HQMMs. We introduced a mathematical framework for the HQMMs and discussed the classical Markov chain-based models, namely the MMs and

HMMs. The purpose of introducing the HQMMs was to better understand the source of quantum advantage gained in the quantum jump metrology scheme. Thus, we started by providing a systematic review of the definitions of the three models, focusing on the parametrisation of the models and the conditions imposed on the transition matrices and the stationary states. For simplicity, we considered modelling a system with two possible outputs A and B. The analysis of the correlations between sequential measurements of the MM showed a lack of long-term correlations. This result was more clearly identified in the evaluation of the autocorrelation function, where the correlation decayed exponentially after some time steps. Furthermore, we examined the effect of increasing the internal states while keeping the same number of two outputs in the case of HMMs. We observed that increasing the number of internal states, in this particular case, does not enhance the complexity of the dynamics of the HMMs. The same test cannot be performed for the MM since increasing the states without increasing the number of outputs is impossible. Therefore, we can predict that going to infinitely many internal states, while keeping two outcomes, in the case of the HMM may not be advantageous in this particular case. Moreover, it is known that increasing the number of internal states in the HMM may lead to the problem of overfitting; therefore, a sufficient number of internal states must be chosen carefully. Furthermore, as a measure of the complexity of the dynamics of the three models, we examined the probability of observing specific sequences for a large number of randomly generated machines for each of the three models. Using the established mathematical framework, we evaluated these probabilities accordingly. The results of the simulations revealed that the three models vary in their capability to generate a certain sequence. Clearly, the HQMM showed a higher probability of generating the chosen sequences than the HMM and the MM, which demonstrates the complex dynamics of the model. Moreover, the HMM gave slightly better results than the MM. A further investigation revealed that the HQMM is also performing well in producing highly correlated sequences observed at sequential time steps, even as the time steps between observations increase. In general, the performance of the models is affected by the choice of

the sequence to be observed, since some sequences can be engineered in classical models to give higher probabilities.

A further extension of this research would be assessing the effect of increasing the number of qubits in the HQMM on the temporal correlations. This is a cumbersome task since the complexity of the system increases rapidly, and a thorough analysis must be done to parametrises such a model. Furthermore, since the quantum jump metrology scheme of the two-cavity network inside a quantum feedback loop, which is considered an open quantum system, represents an example of HQMMs, a natural extension of this project is to study the temporal correlations and the quantum advantage that can be gained by investigating the HQMM with a coherent state.

Appendix A

Expectation values of the number operators $\langle N \rangle$ and $\langle N^2 \rangle$

Using the annihilation operators of the output ports a_4 and a_5 shown in Eq. (2.3) The expectation value of the photon number in Mach-Zehnder interferometer is defined as follows, the expectation value of $\langle N \rangle$ [11]

$$\langle N \rangle = \sin^2(\frac{\Delta\varphi}{2}) \left\langle a_0^\dagger a_0 \right\rangle + \cos^2(\frac{\Delta\varphi}{2}) \left\langle a_1^\dagger a_1 \right\rangle - \frac{\sin(\Delta\varphi)}{2} \left\langle a_0^\dagger a_1 \right\rangle$$
$$- \frac{\sin(\Delta\varphi)}{2} \left\langle a_1^\dagger a_0 \right\rangle . \tag{A.1}$$

Moreover, the expectation value of the square of the photon number is $\langle N^2 \rangle$ [11]

$$\left\langle N^2 \right\rangle = \sin^4(\frac{\Delta\varphi}{2})^2 \left\langle a_0^\dagger a_0^\dagger a_0 a_0 \right\rangle + \cos^4(\frac{\Delta\varphi}{2})^2 \left\langle a_1^\dagger a_1^\dagger a_1 a_1 \right\rangle$$
$$+ \sin^2(\Delta\varphi) \left\langle a_0^\dagger a_0 a_1^\dagger a_1 \right\rangle + \sin^2(\frac{\Delta\varphi}{2}) \left\langle a_0^\dagger a_0 \right\rangle$$
$$+ \cos^2(\frac{\Delta\varphi}{2}) \left\langle a_1^\dagger a_1 \right\rangle + \frac{\sin^2 \Delta\varphi}{4} \left\langle a_0^2 (a_1^\dagger)^2 \right\rangle$$
$$+ \frac{\sin^2 \Delta\varphi}{4} \left\langle (a_0^\dagger)^2 a_1^2 \right\rangle - \sin^2(\frac{\Delta\varphi}{2}) \sin \Delta\varphi \left\langle a_0^\dagger a_0^2 a_1^\dagger \right\rangle$$
$$- \sin^2(\frac{\Delta\varphi}{2}) \sin \Delta\varphi \left\langle (a_0^\dagger)^2 a_0 a_1^\dagger \right\rangle - \cos^2(\frac{\Delta\varphi}{2}) \sin \Delta\varphi \left\langle a_0 (a_1^\dagger)^2 a_1 \right\rangle$$
$$- \cos^2(\frac{\Delta\varphi}{2}) \sin \Delta\varphi \left\langle a_0^\dagger a_1^\dagger a_1^2 \right\rangle - \frac{\sin \Delta\varphi}{2} \left\langle a_0 a_1^\dagger \right\rangle - \frac{\sin \Delta\varphi}{2} \left\langle a_0^\dagger a_1 \right\rangle . \tag{A.2}$$

Appendix B

Transformation between the system environment representation to operator-sum representation

A formal description of Stinespring dilation theorem states that any contraction operator which is completely positive trace preserving map can be thought of as the result of a unitary evolution on a larger dilated system.

Stinestring Dilation: For any completely positive trace preserving map among states in a finite Hilbert space $\mathcal{H}_A$. Let us define the mapping $\mathcal{E}{:}S(\mathcal{H}) \to S(\mathcal{H})$, where $S(\mathcal{H})$ is a bounded operator in the Hilbert space. Then there exist a unitary operator U and a Hilbert space of the ancilla B on the space $\mathcal{H} \otimes \mathcal{B}$ such that,

$$\mathcal{E}(\rho) = \mathrm{Tr}_E U(\rho \otimes |0\rangle \langle 0|)U^\dagger. \tag{B.1}$$

Here $\rho \in S(\mathcal{H})$ and the ancillary system has a dimension $d(B) \leq d^2(\mathcal{H})$.

As a result of the Stinespring theorem, that any non-unitary operator-sum representation, such as Kraus operator, of quantum channel can be written as a unitary operator by extending the system to incorporate the effect of the environment on the system. In other words, we introduce an extra ancillary system

with some basis $|i\rangle_E$ interacting with the principle system ρ_S and taking a partial trace on the ancillary system, there for the mapping of the principal system reads as follows

$$\mathcal{E}(\rho_S) = \sum_i K_i \rho_{SE} K_i^\dagger.$$ (B.2)

The Kraus operators is defined as $K_i = \langle i|_E U |0\rangle_E$. Here U is a unitary operator that can be constructed such that the first block column of U is the Kraus operators defined as

$$U = \begin{bmatrix} K_1 & ... & ... \\ K_2 & ... & ... \\ K_3 & ... & ... \\ ... & ... & ... \\ ... & ... & ... \\ K_n & ... & ... \end{bmatrix}.$$ (B.3)

The rest of the unitary operator U must be constructed such that the it preserves the unitary relation $UU^\dagger = U^\dagger U = I$.

Appendix C

Three and four states of hidden Markov model

For the purpose of examining the effect of increasing the number of internal state in hidden Markov model while keeping the the same number of outcomes, i.e. two outcomes A and B. In this section we present the parametrisation of hidden Markov model with three internal states and four internal states.

C.1 Three-states HMM

For a hidden Markov model with three internal states with two outcomes A and B the transition matrix is given by,

$$T = \begin{pmatrix} t_1 & t_2 & t_3 \\ t_4 & t_5 & t_6 \\ t_7 & t_8 & t_9 \end{pmatrix} . \tag{C.1}$$

where the elements of the transition matrix T must satisfy $t_1 + t_4 + t_7 = 1$, $t_2 + t_5 + t_8 = 1$ and $t_3 + t_6 + t_9 = 1$. The sub-transition matrices T_A and T_B that gives the transition of states while emitting a specific outcome A and B are given

by,

$$T_A = \begin{pmatrix} t_{00} & t_{01} & t_{02} \\ t_{03} & t_{04} & t_{05} \\ t_{06} & t_{07} & t_{08} \end{pmatrix} . \tag{C.2}$$

$$T_B = \begin{pmatrix} t_{10} & t_{11} & t_{12} \\ t_{13} & t_{14} & t_{15} \\ t_{16} & t_{17} & t_{18} \end{pmatrix} . \tag{C.3}$$

where the elements of T_B must satisfy the conditions

$$0 \le t_{10} \le t_1$$
$$0 \le t_{11} \le t_2$$
$$0 \le t_{12} \le t_3$$
$$0 \le t_{13} \le t_4$$
$$0 \le t_{14} \le t_5$$
$$0 \le t_{15} \le t_6$$
$$0 \le t_{16} \le t_7$$
$$0 \le t_{17} \le t_8$$
$$0 \le t_{18} \le t_9 \tag{C.4}$$

Here, $T_A = T - T_B$.

The stationary state $\boldsymbol{p}_{\text{ss}} = (p_1, p_2, p_3)$ of the HMM with three internal states is given by

$$p_3 = \frac{-\big((t_1 - 1)x_2 - (t_4 x_1)\big)}{(y_1 x_2 - y_2 x_1)} . \tag{C.5}$$

$$p_2 = \frac{-\big((t_1 - 1) + p_3 y_1\big)}{x_1} . \tag{C.6}$$

$$p_1 = 1 - p_2 - p_3 . \tag{C.7}$$

Here x_1, x_2, y_1, y_2 defined as

$$x_1 = t_2 - t_1 - 1. \tag{C.8}$$

$$x_2 = t_5 - t_4 - 1. \tag{C.9}$$

$$y_1 = t_3 - t_1 - 1. \tag{C.10}$$

$$y_2 = t_6 - t_4. \tag{C.11}$$

C.2 Four-states HMM

For a hidden Markov model with four internal state and two outcomes A and B, the transition matrix is given by,

$$T = \begin{pmatrix} t_1 & t_2 & t_3 & t_4 \\ t_5 & t_6 & t_7 & t_8 \\ t_9 & t_{10} & t_{11} & t_{12} \\ t_{13} & t_{14} & t_{15} & t_{16} \end{pmatrix}. \tag{C.12}$$

where the elemnts of the transition matrix T must satisfy $t_1 + t_5 + t_9 + t_{13} = 1$, $t_2 + t_6 + t_{10} + t_{14} = 1$, $t_3 + t_7 + t_{11} + t_{15} = 1$ and $t_4 + t_8 + t_{12} + t_{16} = 1$. The sub-transition matrices T_A and T_B are given by,

$$T_A = \begin{pmatrix} t_{00} & t_{01} & t_{02} & t_{03} \\ t_{04} & t_{05} & t_{06} & t_{07} \\ t_{08} & t_{09} & t_{010} & t_{011} \\ t_{012} & t_{013} & t_{014} & t_{015} \end{pmatrix}. \tag{C.13}$$

$$T_B = \begin{pmatrix} t_{10} & t_{11} & t_{12} & t_{13} \\ t_{14} & t_{15} & t_{16} & t_{17} \\ t_{18} & t_{19} & t_{110} & t_{111} \\ t_{112} & t_{113} & t_{114} & t_{115} \end{pmatrix}. \tag{C.14}$$

where the elements of T_B must satisfy the conditions

$$0 \leq t_{10} \leq t_1$$
$$0 \leq t_{11} \leq t_2$$
$$0 \leq t_{12} \leq t_3$$
$$0 \leq t_{13} \leq t_4$$
$$0 \leq t_{14} \leq t_5$$
$$0 \leq t_{15} \leq t_6$$
$$0 \leq t_{16} \leq t_7$$
$$0 \leq t_{17} \leq t_8$$
$$0 \leq t_{18} \leq t_9$$
$$0 \leq t_{19} \leq t_{10}$$
$$0 \leq t_{110} \leq t_{11}$$
$$0 \leq t_{111} \leq t_{12}$$
$$0 \leq t_{112} \leq t_{13}$$
$$0 \leq t_{113} \leq t_{14}$$
$$0 \leq t_{114} \leq t_{15}$$
$$0 \leq t_{115} \leq t_{16} \tag{C.15}$$

Here, $T_A = T - T_B$.

The stationary state for four states HMM is given by $\boldsymbol{p}_{\text{ss}} = (p_1, p_2, p_3, p_4)$

$$p_4 = \frac{-\Big((x_1 y_2) - (x_2 y_1)\Big)}{\Big((y_2 z_1) - (y_1 z - 2)\Big)},$$
$$p_3 = \frac{-(x_1 + p_4 z_1)}{y_1},$$
$$p_2 = \frac{-\Big(t_1 - 1 + p_3(t_3 - t_1 - 1)\Big) + \Big(p_4(t_4 - t_1 - 1)\Big)}{t_2 - t_1 - 1},$$
$$p_1 = 1 - p_2 - p_3 - p_4. \tag{C.16}$$

where x_1, x_2, y_1, y_2, z_1 and z_2 are defined as

$$x1 = (t_1 - 1)(t_6 - 1 - t_5) - (t_5)(t_2 - t_1 - 1) \,. \tag{C.17}$$

$$x2 = t_5(t_{10} - t_9) - t_9(t_6 - t_5 - 1) \,. \tag{C.18}$$

$$y1 = (t_3 - t_1 - 1)(t_6 - t_5 - 1) - (t_7 - t_5)(t_2 - t_1 - 1) \,. \tag{C.19}$$

$$y2 = (t_7 - t_5)(t_{10} - t_9) - (t_{11} - t_9 - 1)(t_6 - t_5 - 1) \,. \tag{C.20}$$

$$z1 = (t_4 - t_1 - 1)(t_6 - t_5 - 1) - (t_2 - t_1 - 1)(t_8 - t_5) \,. \tag{C.21}$$

$$z2 = (t_8 - t_5)(t_{10} - t_9) - (t_6 - t_5 - 1)(t_{12} - t_9) \,. \tag{C.22}$$

Appendix D

Stationary states of hidden quantum Markov model

The stationary state density matrix ρ_{ss} of the HQMM for Kraus operators in Eq. (6.42) was evaluated numerically using `solve` function in MATLAB. The stationary density matrix reads

$$\rho_{\text{ss}} = \begin{pmatrix} \rho_{00} & \rho_{01} \\ \rho_{10} & \rho_{11} \end{pmatrix} . \tag{D.1}$$

where ρ_{00}, ρ_{01},ρ_{10} and ρ_{11} are given by

$$
\begin{aligned}
\rho_{00} &= (a + \cos(2\vartheta) - a\cos(2\varphi + 2\vartheta) + a^2\cos(2\varphi + 2\vartheta) - a^2)/C \\
&\quad + (a\cos(2\varphi) - a\cos(2\vartheta) - 1)/C\,, \\
\rho_{01} &= ((a-1)(\sin(2\varphi) + \sin(2\vartheta) - \sin(2\varphi + 2\vartheta)))/C\,, \\
\rho_{10} &= ((a-1)(\sin(2\varphi) + \sin(2\vartheta) - \sin(2\varphi + 2\vartheta)))/C\,, \\
\rho_{11} &= (\cos(2\varphi) - 1)/C\,. \tag{D.2}
\end{aligned}
$$

where C is defined as

$$
\begin{aligned}
C &= (a + \cos(2\varphi) + \cos(2\vartheta) - a\cos(2\varphi + 2\vartheta) + a^2\cos(2\varphi + 2\vartheta) \\
&\quad - a^2 + a\cos(2\varphi) - a\cos(2\vartheta) - 2)\,. \tag{D.3}
\end{aligned}
$$

135

References

[1] A. Aspect, J. Dalibard, and G. Roger, "Experimental test of bell's inequalities using time-varying analyzers," *Physical review letters*, vol. 49, no. 25, p. 1804, 1982.

[2] E. Polino, M. Valeri, N. Spagnolo, and F. Sciarrino, "Photonic quantum metrology," *AVS Quantum Science*, vol. 2, no. 2, 2020.

[3] M. G. Paris, "Quantum estimation for quantum technology," *International Journal of Quantum Information*, vol. 7, no. supp01, pp. 125–137, 2009.

[4] S. Aaronson and A. Arkhipov, "The computational complexity of linear optics," in *Proceedings of the forty-third annual ACM symposium on Theory of computing*, pp. 333–342, 2011.

[5] F. Wolfgramm, C. Vitelli, F. A. Beduini, N. Godbout, and M. W. Mitchell, "Entanglement-enhanced probing of a delicate material system," *Nature Photonics*, vol. 7, no. 1, pp. 28–32, 2013.

[6] M. A. Taylor, J. Janousek, V. Daria, J. Knittel, B. Hage, H.-A. Bachor, and W. P. Bowen, "Biological measurement beyond the quantum limit," *Nature Photonics*, vol. 7, no. 3, pp. 229–233, 2013.

[7] B. P. Abbott, R. Abbott, T. Abbott, M. Abernathy, F. Acernese, K. Ackley, C. Adams, T. Adams, P. Addesso, R. Adhikari, *et al.*, "Observation of gravitational waves from a binary black hole merger," *Physical review letters*, vol. 116, no. 6, p. 061102, 2016.

[8] R. Demkowicz-Dobrzański, M. Jarzyna, and J. Kołodyński, "Quantum limits in optical interferometry," *Progress in Optics*, vol. 60, pp. 345–435, 2015.

[9] S. Yang and G. Zhang, "A review of interferometry for geometric measurement," *Measurement Science and Technology*, vol. 29, no. 10, p. 102001, 2018.

[10] R. Loughridge and D. Y. Abramovitch, "A tutorial on laser interferometry for precision measurements," in *2013 American control conference*, pp. 3686–3703, IEEE, 2013.

[11] S. Ataman, A. Preda, and R. Ionicioiu, "Phase sensitivity of a mach-zehnder interferometer with single-intensity and difference-intensity detection," *Physical Review A*, vol. 98, no. 4, p. 043856, 2018.

[12] Z. Blanco-Garcia, "Quantum control of the states of light in a mach-zehnder interferometer," in *Journal of Physics: Conference Series*, vol. 839, p. 012021, IOP Publishing, 2017.

[13] L. A. Clark, A. Stokes, and A. Beige, "Quantum jump metrology," *Physical Review A*, vol. 99, no. 2, p. 022102, 2019.

[14] L. A. Clark, A. Stokes, and A. Beige, "Quantum-enhanced metrology with the single-mode coherent states of an optical cavity inside a quantum feedback loop," *Physical Review A*, vol. 94, no. 2, p. 023840, 2016.

[15] J. F. Haase, A. Smirne, S. Huelga, J. Kołodynski, and R. Demkowicz-Dobrzanski, "Precision limits in quantum metrology with open quantum systems," *Quantum Measurements and Quantum Metrology*, vol. 5, no. 1, pp. 13–39, 2016.

[16] R. Demkowicz-Dobrzański, J. Kołodyński, and M. Guţă, "The elusive heisenberg limit in quantum-enhanced metrology," *Nature communications*, vol. 3, no. 1, p. 1063, 2012.

[17] B. Escher, R. de Matos Filho, and L. Davidovich, "General framework for estimating the ultimate precision limit in noisy quantum-enhanced metrology," *Nature Physics*, vol. 7, no. 5, pp. 406–411 2011.

[18] H.-P. Breuer, F. Petruccione, *et al.*, *The theory of open quantum systems.* Oxford University Press, 2002.

[19] A. Monras, A. Beige, and K. Wiesner, "Hidden quantum markov models and non-adaptive read-out of many-body states,"*App. Math. and Comp. Sciences* 3,93 (2010).

[20] K. Wiesner and J. P. Crutchfield, "Computation in finitary stochastic and quantum processes," *Physica D: Nonlinear Phenomena*, vol. 237, no. 9, pp. 1173–1195, 2010.

[21] M. Cholewa, P. Gawron, P. GÅ,omb, and D. Kurzyk, "Quantum hidden markov models based on transition operation matrices," *Quantum Information Processing*, vol. 16, no. 4, p. 101, 2017.

[22] S. Srinivasan, G. Gordon, and B. Boots, "Learning hidden quantum markov models," in *International Conference on Artificial Intelligence and Statistics*, pp. 1979–1987, PMLR, 2018.

[23] V. Markov, V. Rastunkov, A. Deshmukh, D. Fry, and C. Stefanski, "Implementation and learning of quantum hidden markov models," *arXiv preprint arXiv:2212.03796*, 2022.

[24] L. A. Clark, W. Huang, T. M. Barlow, and A. Beige, "Hidden quantum markov models and open quantum systems with instantaneous feedback," in *ISCS 2014: Interdisciplinary Symposium on Complex Systems*, pp. 143–151, Springer, 2015.

[25] V. Giovannetti, S. Lloyd, and L. Maccone, "Advances in quantum metrology," *Nature photonics*, vol. 5, no. 4, pp. 222–229, 2011.

[26] G. Tóth and I. Apellaniz, "Quantum metrology from a quantum information science perspective," *Journal of Physics A: Mathematical and Theoretical*, vol. 47, no. 42, p. 424006, 2014.

[27] L. Pezzè, A. Smerzi, M. K. Oberthaler, R. Schmied, and P. Treutlein, "Quantum metrology with nonclassical states of atomic ensembles," *Reviews of Modern Physics*, vol. 90, no. 3, p. 035005, 2018.

[28] C. Gerry, P. Knight, and P. L. Knight, *Introductory quantum optics*. Cambridge university press, 2005.

[29] J. P. Dowling and K. P. Seshadreesan, "Quantum optical technologies for metrology, sensing, and imaging," *Journal of Lightwave Technology*, vol. 33, no. 12, pp. 2359–2370, 2014.

[30] V. Giovannetti, S. Lloyd, and L. Maccone, "Quantum-enhanced measurements: beating the standard quantum limit," *Science*, vol. 306, no. 5700, pp. 1330–1336, 2004.

[31] V. Giovannetti, S. Lloyd, and L. Maccone, "Quantum metrology," *Physical review letters*, vol. 96, no. 1, p. 010401, 2006.

[32] L. Pezze, A. Smerzi, G. Khoury, J. F. Hodelin, and D. Bouwmeester, "Phase detection at the quantum limit with multi-photon mach-zehnder interferometry," *Physical Review Letters*, vol. 99, no. 22, p. 223602, 2007.

[33] M. Zwierz and H. M. Wiseman, "Precision bounds for noisy nonlinear quantum metrology," *Physical Review A*, vol. 89, no. 2, p. 022107, 2014.

[34] B. C. Sanders and G. J. Milburn, "Optimal quantum measurements for phase estimation," *Physical Review Letters*, vol. 75, no. 16, pp. 2944–2947, 1995.

[35] S. Boixo, A. Datta, S. T. Flammia, A. Shaji, E. Bagan, and C. M. Caves, "Quantum-limited metrology with product states," *Physical Review A*, vol. 77, no. 1, p. 012317, 2008.

[36] M. Holland and K. Burnett, "Interferometric detection of optical phase shifts at the heisenberg limit," *Physical review letters*, vol. 71, no. 9, p. 1355, 1993.

[37] C. M. Caves, "Quantum-mechanical noise in an interferometer," *Physical Review D*, vol. 23, no. 8, p. 1693, 1981.

[38] R. S. Bondurant and J. H. Shapiro, "Squeezed states in phase-sensing interferometers," *Physical Review D*, vol. 30, no. 12, p. 2548, 1984.

[39] J. P. Dowling, "Quantum optical metrology–the lowdown on high-n00n states," *Contemporary physics*, vol. 49, no. 2, pp. 125–143, 2008.

[40] D. W. Berry and H. M. Wiseman, "Optimal states and almost optimal adaptive measurements for quantum interferometry," *Physical review letters*, vol. 85, no. 24, p. 5098, 2000.

[41] M. D. Vidrighin, G. Donati, M. G. Genoni, X.-M. Jin, W. S. Kolthammer, M. Kim, A. Datta, M. Barbieri, and I. A. Walmsley, "Joint estimation of phase and phase diffusion for quantum metrology," *Nature communications*, vol. 5, no. 1, pp. 1–7, 2014.

[42] G.-Y. Xiang, B. L. Higgins, D. Berry, H. M. Wiseman, and G. Pryde, "Entanglement-enhanced measurement of a completely unknown optical phase," *Nature Photonics*, vol. 5, no. 1, pp. 43–47, 2011.

[43] I. Afek, O. Ambar, and Y. Silberberg, "High-noon states by mixing quantum and classical light," *Science*, vol. 328, no. 5980, pp. 879–881, 2010.

[44] T. Nagata, R. Okamoto, J. L. O'brien, K. Sasaki, and S. Takeuchi, "Beating the standard quantum limit with four-entangled photons," *Science*, vol. 316, no. 5825, pp. 726–729, 2007.

[45] H. Lee, P. Kok, and J. P. Dowling, "A quantum rosetta stone for interferometry," *Journal of Modern Optics*, vol. 49, no. 14-15, pp. 2325–2338, 2002.

[46] M. W. Mitchell, J. S. Lundeen, and A. M. Steinberg, "Super-resolving phase measurements with a multiphoton entangled state," *Nature*, vol. 429, no. 6988, pp. 161–164, 2004.

[47] G. J. Pryde and A. G. White, "Creation of maximally entangled photon-number states using optical fiber multiports," *Physical Review A*, vol. 68, no. 5, p. 052315, 2003.

[48] Y. Israel, I. Afek, S. Rosen, O. Ambar, and Y. Silberberg, "Experimental tomography of noon states with large photon numbers," *Physical Review A*, vol. 85, no. 2, p. 022115, 2012.

[49] G. Gilbert, M. Hamrick, and Y. S. Weinstein, "Practical quantum interferometry using photonic noon states," in *Quantum Information and Computation V*, vol. 6573, pp. 173–181, SPIE, 2007.

[50] N. Thomas-Peter, B. J. Smith, A. Datta, L. Zhang, U. Dorner, and I. A. Walmsley, "Real-world quantum sensors: evaluating resources for precision measurement," *Physical review letters*, vol. 107, no. 11, p. 113603, 2011.

[51] S. Boixo, A. Datta, M. J. Davis, S. T. Flammia, A. Shaji, and C. M. Caves, "Quantum metrology: dynamics versus entanglement," *Physical review letters*, vol. 101, no. 4, p. 040403, 2008.

[52] M. Napolitano, M. Koschorreck, B. Dubost, N. Behbood, R. Sewell, and M. W. Mitchell, "Interaction-based quantum metrology showing scaling beyond the heisenberg limit," *Nature*, vol. 471, no. 7339, pp. 486–489, 2011.

[53] A. Datta and A. Shaji, "Quantum metrology without quantum entanglement," *Modern Physics Letters B*, vol. 26, no. 18, p. 1230010, 2012.

[54] B. L. Higgins, D. W. Berry, S. D. Bartlett, H. M. Wiseman, and G. J. Pryde, "Entanglement-free heisenberg-limited phase estimation," *Nature*, vol. 450, no. 7168, pp. 393–396, 2007.

[55] D. Braun, G. Adesso, F. Benatti, R. Floreanini, U. Marzolino, M. W. Mitchell, and S. Pirandola, "Quantum-enhanced measurements without entanglement," *Reviews of Modern Physics*, vol. 90, no. 3, p. 035006, 2018.

[56] M. Zwierz, C. A. Pérez-Delgado, and P. Kok, "Ultimate limits to quantum metrology and the meaning of the heisenberg limit," *Physical Review A*, vol. 85, no. 4, p. 042112, 2012.

[57] D. W. Berry and H. M. Wiseman, "Optimal states and almost optimal adaptive measurements for quantum interferometry," *Physical review letters*, vol. 85, no. 24, p. 5098, 2000.

[58] A. Shabani, J. Roden, and K. Whaley, "Continuous measurement of a non-markovian open quantum system," *Physical review letters*, vol. 112, no. 11, p. 113601, 2014.

[59] M. Beau and A. del Campo, "Nonlinear quantum metrology of many-body open systems," *Physical review letters*, vol. 119, no. 1, p. 010403, 2017.

[60] F. Albarelli, M. A. Rossi, D. Tamascelli, and M. G. Genoni, "Restoring heisenberg scaling in noisy quantum metrology by monitoring the environment," *Quantum*, vol. 2, p. 110, 2018.

[61] C. Ahn, A. C. Doherty, and A. J. Landahl, "Continuous quantum error correction via quantum feedback control," *Physical Review A*, vol. 65, no. 4, p. 042301, 2002.

[62] J. Wang and H. M. Wiseman, "Feedback-stabilization of an arbitrary pure state of a two-level atom," *Physical Review A*, vol. 64, no. 6, p. 063810, 2001.

[63] J. Wang, H. M. Wiseman, and G. J. Milburn, "Dynamical creation of entanglement by homodyne-mediated feedback," *Physical Review A*, vol. 71, no. 4, p. 042309, 2005.

[64] L. A. Clark, F. Torzewska, B. Maybee, and A. Beige, "Non-ergodicity in open quantum systems through quantum feedback," *Europhysics Letters*, vol. 130, no. 5, p. 54002, 2020.

[65] H. Cramér, *Mathematical methods of statistics*, vol. 43. Princeton university press, 1999.

[66] S. L. Braunstein and C. M. Caves, "Statistical distance and the geometry of quantum states," *Physical Review Letters*, vol. 72, no. 22, p. 3439, 1994.

[67] C. Brukner, S. Taylor, S. Cheung, and V. Vedral, "Quantum entanglement in time," *arXiv preprint quant-ph/0402127*, 2004.

[68] C. Simon and J.-P. Poizat, "Creating single time-bin-entangled photon pairs," *Physical review letters*, vol. 94, no. 3, p. 030502, 2005.

[69] H. Jayakumar, A. Predojević, T. Kauten, T. Huber, G. S. Solomon, and G. Weihs, "Time-bin entangled photons from a quantum dot," *Nature communications*, vol. 5, no. 1, p. 4251, 2014.

[70] A. Einstein, B. Podolsky, and N. Rosen, "Can quantum-mechanical description of physical reality be considered complete?," *Physical Review*, vol. 47, no. 10, pp. 777–780, 1935.

[71] J. S. Bell, "On the einstein podolsky rosen paradox," *Physics Physique Fizika*, vol. 1, no. 3, p. 195, 1964.

[72] M. A. Rowe, D. Kielpinski, V. Meyer, C. A. Sackett, W. M. Itano, C. Monroe, and D. J. Wineland, "Experimental violation of a bell's inequality with efficient detection," *Nature*, vol. 409, no. 6822, pp. 791–794, 2001.

[73] V. Vedral, M. B. Plenio, M. A. Rippin, and P. L. Knight, "Quantifying entanglement," *Physical Review Letters*, vol. 78, no. 12, pp. 2275–2279, 1997.

[74] C. Eltschka and J. Siewert, "Quantifying entanglement resources," *Journal of Physics A: Mathematical and Theoretical*, vol. 47, no. 42, p. 424005, 2014.

[75] R. Horodecki, P. Horodecki, M. Horodecki, and K. Horodecki, "Quantum entanglement," *Reviews of modern physics*, vol. 81, no. 2, p. 865, 2009.

[76] H. Ollivier and W. H. Zurek, "Quantum discord: a measure of the quantumness of correlations," *Physical review letters*, vol. 88, no. 1, p. 017901, 2001.

[77] D. Braun and J. Martin, "Heisenberg-limited sensitivity with decoherence-enhanced measurements," *Nature communications*, vol. 2, no. 1, p. 223, 2011.

[78] K. Macieszczak, M. Guţă, I. Lesanovsky, and J. P. Garrahan, "Dynamical phase transitions as a resource for quantum enhanced metrology," *Physical Review A*, vol. 93, no. 2, p. 022103, 2016.

[79] D. Braun, G. Adesso, F. Benatti, R. Floreanini, U. Marzolino, M. W. Mitchell, and S. Pirandola, "Quantum-enhanced measurements without entanglement," *Reviews of Modern Physics*, vol. 90, no. 3, p. 035006, 2018.

[80] J. R. Norris, *Markov chains.* No. 2, Cambridge university press, 1998.

[81] C. Andrieu, N. De Freitas, A. Doucet, and M. I. Jordan, "An introduction to mcmc for machine learning," *Machine learning*, vol. 50, pp. 5–43, 2003.

[82] D. Van Ravenzwaaij, P. Cassey, and S. D. Brown, "A simple introduction to markov chain monte–carlo sampling," *Psychonomic bulletin & review*, vol. 25, no. 1, pp. 143–154, 2018.

[83] A. J. Pinho, P. J. Ferreira, A. J. Neves, and C. A. Bastos, "On the representability of complete genomes by multiple competing finite-context (markov) models," *PloS one*, vol. 6, no. 6, p. e21588, 2011.

[84] S. R. Eddy, "Hidden markov models," *Current opinion in structural biology*, vol. 6, no. 3, pp. 361–365, 1996.

[85] L. Rabiner, "A tutorial on hidden markov models and selected applications in speech recognition," *PROCEEDINGS OF THE IEEE*, vol. 77, no. 2, 1989.

[86] B. H. Juang and L. R. Rabiner, "Hidden markov models for speech recognition," *Technometrics*, vol. 33, no. 3, pp. 251–272, 1991.

[87] L. Rabiner and B. Juang, "An introduction to hidden markov models," *ieee assp magazine*, vol. 3, no. 1, pp. 4–16, 1986.

[88] J. P. Coelho, T. M. Pinho, and J. Boaventura-Cunha, *Hidden Markov Models: Theory and Implementation using MATLAB®*. CRC Press, 2019.

[89] A. Viterbi, "Error bounds for convolutional codes and an asymptotically optimum decoding algorithm," *IEEE transactions on Information Theory*, vol. 13, no. 2, pp. 260–269, 1967.

[90] L. E. Baum, T. Petrie, G. Soules, and N. Weiss, "A maximization technique occurring in the statistical analysis of probabilistic functions of markov chains," *The annals of mathematical statistics*, vol. 41, no. 1, pp. 164–171, 1970.

[91] M. Gales and S. Young, "The application of hidden markov models in speech recognition," *Foundations and Trends in Signal Processing*, vol. 1, no. 3, pp. 195–304, 2007.

[92] T. Rydén, T. Teräsvirta, and S. Åsbrink, "Stylized facts of daily return series and the hidden markov model," *Journal of applied econometrics*, vol. 13, no. 3, pp. 217–244, 1998.

[93] G. A. Churchill, "Accurate restoration of dna sequences," in *Case Studies in Bayesian Statistics, Volume II*, pp. 90–148, Springer, 1995.

[94] J. Bechhoefer, "Hidden markov models for stochastic thermodynamics," *New Journal of Physics*, vol. 17, no. 7, p. 075003, 2015.

[95] S. Suvorova, L. Sun, A. Melatos, W. Moran, and R. J. Evans, "Hidden markov model tracking of continuous gravitational waves from a neutron star with wandering spin," *Physical Review D*, vol. 93, no. 12, p. 123009, 2016.

[96] M. G. House, H. W. Jiang, and X. C. Zhang, "Analysis of electron tunneling events with the hidden markov model," *Physical Review B*, vol. 80, no. 11, p. 113308, 2009.

[97] S. Gammelmark, K. Mølmer, W. Alt, T. Kampschulte, and D. Meschede, "Hidden markov model of atomic quantum jump dynamics in an optically probed cavity," *Physical Review A*, vol. 89, no. 4, p. 043839, 2014.

[98] M. A. Nielsen and I. Chuang, *Quantum computation and quantum information.* Cambridge University Press, 2002.

[99] J.-M. Raimond and S. Haroche, *Exploring the quantum.* Oxford University Press, vol. 82, p. 86, 2006.

[100] M. Le Bellac, *Quantum physics.* Cambridge University Press, 2011.

[101] D. Manzano, "A short introduction to the lindblad master equation," *Aip Advances*, vol. 10, no. 2, p. 025106, 2020.

[102] C. A. Brasil, F. F. Fanchini, and R. d. J. Napolitano, "A simple derivation of the lindblad equation," *Revista Brasileira de Ensino de Física*, vol. 35, pp. 01–09, 2013.

[103] P. Rice, *An Introduction to Quantum Optics.* IOP Publishing Limited, 2020.

[104] S. Barnett, *Quantum information*, vol. 16. Oxford University Press, 2009.

[105] J. Dalibard, Y. Castin, and K. Mølmer, "Wave-function approach to dissipative processes in quantum optics," *Physical review letters*, vol. 68, no. 5, p. 580, 1992.

[106] M. B. Plenio and P. L. Knight, "The quantum-jump approach to dissipative dynamics in quantum optics," *Reviews of Modern Physics*, vol. 70, no. 1, p. 101, 1998.

[107] K. Mølmer, Y. Castin, and J. Dalibard, "Monte carlo wave-function method in quantum optics," *JOSA B*, vol. 10, no. 3, pp. 524–538, 1993.

[108] P. Warszawski and H. M. Wiseman, "Quantum trajectories for realistic photodetection II: Application and analysis," *Journal of Optics B: Quantum and Semiclassical Optics*, vol. 5, no. 1, pp. 15–28, 2003.

[109] P. Warszawski and H. M. Wiseman, "Quantum trajectories for realistic photodetection i: General formalism," *Journal of Optics B: Quantum and Semiclassical Optics*, vol. 5, no. 1, pp. 1–14, 2003.

[110] T. A. Brun, "A simple model of quantum trajectories," *American Journal of Physics*, vol. 70, no. 7, pp. 719–737, 2002.

[111] M. Khudaverdyan, W. Alt, T. Kampschulte, S. Reick, A. Thobe, A. Widera, and D. Meschede, "Quantum jumps and spin dynamics of interacting atoms in a strongly coupled atom-cavity system," *Physical Review Letters*, vol. 103, no. 12, p. 123006, 2009.

[112] S. Reick, K. Mølmer, W. Alt, M. Eckstein, T. Kampschulte, L. Kong, R. Reimann, A. Thobe, A. Widera, and D. Meschede, "Analyzing quantum jumps of one and two atoms strongly coupled to an optical cavity," *Journal of the Optical Society of America B*, vol. 27, no. 6, p. A152, 2010.

[113] S. Gleyzes, S. Kuhr, C. Guerlin, J. Bernu, S. Deleglise, U. Busk Hoff, M. Brune, J.-M. Raimond, and S. Haroche, "Quantum jumps of light recording the birth and death of a photon in a cavity," *Nature*, vol. 446, pp. 297–300, Mar. 2007.

[114] Y. Castin, J. Dalibard, and K. Mølmer, "A wave function approach to dissipative processes," in *AIP Conference Proceedings*, vol. 275, pp. 143–156, American Institute of Physics, 1993.

[115] C. A. McDermott, "The quantum jump method: photon statistics and macroscopic quantum jumps of two interacting atoms," *arXiv preprint arXiv:2201.11193*, 2022.

[116] G. C. Hegerfeldt, "Ensemble versus individual system in quantum optics," *Fortschritte der Physik*, vol. 46, no. 6, pp. 595–604, 1998.

[117] W. Nagourney, J. Sandberg, and H. Dehmelt, "Shelved optical electron amplifier: Observation of quantum jumps," *Physical Review Letters*, vol. 56, no. 26, p. 2797, 1986.

[118] S. Gleyzes, S. Kuhr, C. Guerlin, J. Bernu, S. Deleglise, U. Busk Hoff, M. Brune, J.-M. Raimond, and S. Haroche, "Quantum jumps of light recording the birth and death of a photon in a cavity," *Nature*, vol. 446, no. 7133, pp. 297–300, 2007.

[119] P. Courteille, "Atom-light interaction and basic applications:lecture notes." https://www.ictp-saifr.org/wp-content/uploads/2019/09/LightAtomsLecture.pdf, September 2019. [Online; accessed 14-January-2022].

[120] M. Orszag, *Quantum optics: including noise reduction, trapped ions, quantum trajectories, and decoherence.* Springer, 2016.

[121] L. A. Clark, *Quantum feedback for quantum technology.* PhD thesis, University of Leeds, 2017.

[122] B. Li, J. Bartos, Y. Xie, and S.-W. Huang, "Time-magnified photon counting with 550-fs resolution," *Optica*, vol. 8, no. 8, pp. 1109–1112, 2021.

[123] I. Straka, J. Grygar, J. Hloušek, and M. Ježek, "Counting statistics of actively quenched spads under continuous illumination," *Journal of Lightwave Technology*, vol. 38, no. 17, pp. 4765–4771, 2020.

[124] G. C. Hegerfeldt, "How to reset an atom after a photon detection: Applications to photon-counting processes," *Physical Review A*, vol. 47, no. 1, p. 449, 1993.

[125] J. Dalibard, Y. Castin, and K. Mølmer, "Wave-function approach to dissipative processes in quantum optics," *Physical review letters*, vol. 68, no. 5, p. 580, 1992.

[126] H. Carmichael, *An open systems approach to quantum optics: lectures presented at the Université Libre de Bruxelles, October 28 to November 4, 1991*, vol. 18. Springer Science & Business Media, 2009.

[127] S. Gammelmark and K. Mølmer, "Fisher information and the quantum cramér-rao sensitivity limit of continuous measurements," *Physical review letters*, vol. 112, no. 17, p. 170401, 2014.

[128] R. Sweke, I. Sinayskiy, D. Bernard, and F. Petruccione, "Universal simulation of markovian open quantum systems," *Physical Review A*, vol. 91, no. 6, p. 062308, 2015.

[129] C. Budroni, T. Moroder, M. Kleinmann, and O. Guhne, "Bounding temporal quantum correlations," *Physical Review Letters*, vol. 111, no. 2, p. 020403, 2013.

[130] C. Brukner, S. Taylor, S. Cheung, and V. Vedral, "Quantum entanglement in time," 2004.

[131] S. Milz, C. Spee, Z.-P. Xu, F. Pollock, K. Modi, and O. Gühne, "Genuine multipartite entanglement in time," *SciPost Physics*, vol. 10, no. 6, p. 141, 2021.

[132] J. D. Franson, "Bell inequality for position and time," *Physical review letters*, vol. 62, no. 19, p. 2205, 1989.

[133] J. Brendel, N. Gisin, W. Tittel, and H. Zbinden, "Pulsed energy-time entangled twin-photon source for quantum communication," *Physical Review Letters*, vol. 82, no. 12, p. 2594, 1999.

[134] L. B. Vieira and C. Budroni, "Temporal correlations in the simplest measurement sequences," *Quantum*, vol. 6, p. 623, 2022.

[135] M. Gu, K. Wiesner, E. Rieper, and V. Vedral, "Quantum mechanics can reduce the complexity of classical models," *Nature Communications*, vol. 3, no. 1, p. 762, 2012.

[136] K. Korzekwa and M. Lostaglio, "Quantum advantage in simulating stochastic processes," *Physical Review X*, vol. 11, no. 2, p. 021019, 2021.

[137] T. J. Elliott, M. Gu, A. J. Garner, and J. Thompson, "Quantum adaptive agents with efficient long-term memories," *Physical Review X*, vol. 12, no. 1, p. 011007, 2022.

[138] T. J. Elliott and M. Gu, "Superior memory efficiency of quantum devices for the simulation of continuous-time stochastic processes," *npj Quantum Information*, vol. 4, no. 1, p. 18, 2018.

[139] T. J. Elliott, C. Yang, F. C. Binder, A. J. Garner, J. Thompson, and M. Gu, "Extreme dimensionality reduction with quantum modeling," *Physical Review Letters*, vol. 125, no. 26, p. 260501, 2020.

[140] C. Blank, D. K. Park, and F. Petruccione, "Quantum-enhanced analysis of discrete stochastic processes," *npj Quantum Information*, vol. 7, no. 1, p. 126, 2021.

[141] H. Jaeger, "Observable operator models for discrete stochastic time series," *Neural computation*, vol. 12, no. 6, pp. 1371–1398, 2000.

[142] J. K. Grewal, M. Krzywinski, and N. Altman, "Markov models-hidden markov models," *Nature methods*, vol. 16, no. 9, pp. 795–796, 2019.

[143] B. Vanluyten, J. C. Willems, and B. De Moor, "Equivalence of state representations for hidden markov models," *Systems & Control Letters*, vol. 57, no. 5, pp. 410–419, 2008.

[144] G. Benenti, G. Casati, and G. Strini, *Principles of Quantum Computation and Information-Volume II: Basic Tools and Special Topics.* World Scientific Publishing Company, 2007.

[145] F. Buscemi, G. M. D'Ariano, and M. F. Sacchi, "Physical realizations of quantum operations," *Physical Review A*, vol. 68, no. 4, p. 042113, 2003.

[146] Z. Hu, R. Xia, and S. Kais, "A quantum algorithm for evolving open quantum dynamics on quantum computing devices," *Scientific reports*, vol. 10, no. 1, p. 3301, 2020.

[147] P. Del Moral and S. Penev, *Stochastic Processes: From Applications to Theory.* CRC Press, 2017.